Tuning the electron localization in transition-metal oxide compounds: Fe_3O_4 and TiOCl under extreme conditions

Dissertation zur Erlangung des Doktorgrades der
Mathematisch-Naturwissenschaftlichen Fakultät der
Universität Augsburg

vorgelegt von

Jihaan Fath-Allah Abo-Elyazeed Ebad-Allah

July 2013

Erstgutachter:	Prof. Dr. C.A. Kuntscher
Zweitgutachter:	Prof. Dr. Armin Reller

Tag der mündlichen Prüfung: 30 July 2013

To my family, especially my parents, my husband, and my kids Noran, Nadin, and Mazen for giving me their endless love and support during my life.

Contents

Chapter 1

Introduction

The discovery of a metal-insulator transition in transition metal oxides has stimulated extensive theoretical and experimental studies, due to their interesting physical phenomena, such as Mott-insulator, charge ordering, high-T_c superconductivity, Peierls transition, etc. Due to the dimensionality and the narrow d-bands in transition metal oxides, both of electron-electron and electron-phonon interactions generally play an important role in their physical properties. In some systems clear signatures of both of these interactions are present, leading to a competition or interplay between them which can give rise to different physics, e.g., metal-insulator transition, depending on the value of relevant control parameters and the chemical and electronic properties of the materials. In the case of electron-electron interactions, a charge ordering or a spin density wave can occur. For electron-phonon interactions, several fingerprints can be observed, specifically, polaronic features in the optical conductivity.

The effects which occur in the material due to the electron-electron interactions and electron-phonon interactions, are sensitive to external influences such as temperature and pressure. The compression of the crystal lattice by applying an external pressure usually changes the atomic separation and the electronic bandwidth. Therefore, the application of external pressure allows one to study the physical properties of the system as a function of bandwidth control, which affects the electronic and the structural properties of the material and a metal-insulator transition could be achieved. Furthermore, cooling down changes the thermal contraction of the crystal lattice which could also affect the electronic and the structural properties of the material.

In spite of intensive research over the last decade, the nature of the metallic state in strongly correlated materials is still poorly understood. This is particularly true for a wide range of materials, including transition metal oxides, that have high pressure and/or low temperature properties (e.g., the appearance of the coherent excitation) consistent with a Fermi liquid but at low pressure and/or higher temperature are inconsistent with a Fermi liquid. The dynamic mean-field theory and its development during the last decade became a powerful tool for understanding the metal-insulator transitions in the strongly correlated systems via investigating various lattice models such as the Hubbard model. Optical spectroscopy is a powerful tool to investigate the electronic and vibrational properties of transition metal oxides.

In this thesis, two classes of transition metal oxides have been studied, namely: Fe_3O_4 and TiOCl. The main experimental techniques used are infrared spectroscopy and x-ray powder diffraction (XRD). For Fe_3O_4, the infrared spectroscopy measurements were carried out, first under high pressure at room temperature, then under high pressure and low temperature. For TiOCl, both experimental techniques were used to investigate the electronic and structural properties of this compound.

Magnetite belongs to the strongly electronically correlated systems. It shows many interesting physical properties, including a Verwey transition at T_V=122 K, which has attracted much interest since it was discovered in 1939. Within the present work, the pressure effects on the optical properties of magnetite were studied: first at room temperature then at low temperature. In the first part of the study, the polaronic nature of the observed band in the mid-infrared frequency range was investigated via several theoretical models. In the second part of the study, the pressure-dependance of the Verwey transition temperature in the far-infrared range was investigated.

TiOCl is a low-dimensional Mott-Hubbard insulator. Recently, the application of pressure on this compound revealed strong changes in its electronic and structural properties. Based on these results, the possibility of a pressure induced insulator-to-metal transition was suggested. In this project, the pressure-dependent structural properties of TiOCl at room temperature are investigated by x-ray powder diffraction measurements. Moreover, the pressure-dependant transmittance measurements at low temperature on single crystal of TiOCl in the mid-infrared frequency range are presented.

This thesis is organized as the following: A brief introduction into metal-to-insulator transitions will be presented in Chapter 2, the experimental techniques which are used to carry out the measurements and the analysis methods which are required for extracting the physical information are briefly reviewed in Chapter 3. In Chapter 4, the basic properties of magnetite and the observed changes of its optical properties under high pressure and low temperature are presented. Finally, in Chapter 5 the pressure-dependant XRD measurements of TiOCl are explained. Furthermore, the high pressure and low temperature infrared spectroscopy investigations on TiOCl are discussed.

Chapter 2

Theoretical Basics

2.1 Electron-electron interaction

Transition-metal oxides are generally characterized by their strong electronic correlations within the partly filled $3d$ orbitals. Therefore, various interesting physical phenomena were observed in transition-metal oxides like their metallization under extreme conditions [1]. A simple band theory[1] is the first theory which managed to distinct between the two major classes of materials (metals and insulators) and the transitions among them in a satisfactory way which depends mostly on the filling of the electronic bands at zero temperature. The electronic bands can be separated completely from each other due to the influence of the periodic potential, i.e., there can be an energy gap between bands where the Fermi level lies. As shown in Figure 2.1, when the Fermi level lies in a gap between a completely empty conduction band and a completely filled valence band, we will have an insulator since completely filled bands cannot contribute to transport. Furthermore, we will have a metal when the Fermi level crosses the conduction band. A third class of materials are semiconductors, where the band gap between the valence band and the conduction band is smaller than the energy gap of an insulator (i.e., band gap is small enough to allow for thermal excitations between the valence and the conduction band). Unfortunately, for the more complicated

---

[1] It is also called Bloch-Wilson theory and it is based on the electron interaction with the periodic ion potential. This interaction gives rise to the energy gap between the lowest conduction band and the highest valence band.

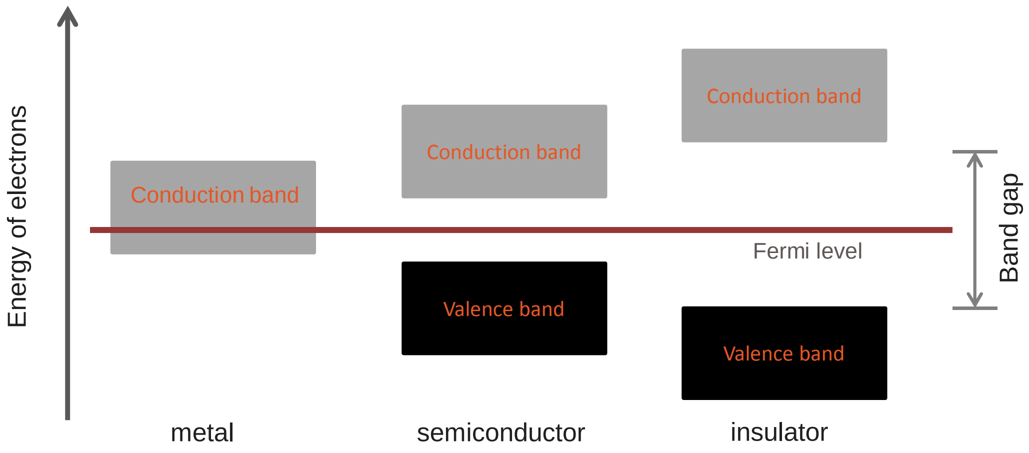

Figure 2.1: Schematic representation of the three types of electronic properties commonly exhibited in solids.

systems the band theory fails to describe a wide range of their physical properties because the electron-electron interaction is neglected, beside the absence of both the static deformation of the lattice[1] and the disorder[2]. For example, in some metal oxide compounds (e.g., NiO, CuO, ...etc), the band theory predicted that they will be metals, while experimentally they are insulators[3].

Later, Mott and Peierls clarified the importance of the electron-electron interaction for the determination of the electrodynamic properties of those systems, where the effect of the electronic interactions are known to be strong in the narrow-band systems. As a result, they become Mott-insulators when they are predicted to be metals according to the band theory [5, 6]. The resulting gap in

---

[1] The electron-ion interaction leads to a static distortion of the whole lattice structure, where the symmetry of the origin lattice is broken. The interaction between the electron and the static lattice is called Peierls insulator. This interaction results in the formation of a static periodic lattice deformation and a commensurate charge density wave of the electrons [2].

[2] Electron interaction with impurities and other lattice imperfection (disorder) may cause localization of electrons which is called Anderson insulator. In Anderson insulators the disorder induced localization of electrons leads to the occurrence of mobility edges that separate localized and delocalized states in a band. If the Fermi level lies between a band edge and its corresponding mobility edge, the single-electron states around the Fermi level are insulator states [2].

[3] De Boer, Verwey, Peierls, and Mott [3, 4] reported that NiO is experimentally an insulator although its eight d-electrons should only partly fill the 3d subshells.

the excitations spectra may arise either from the long-rang antiferromagnetic order of the pre-formed moments (Mott-Heisenberg insulator) or a quantum phase transition induced by charge and/or spin correlations (Mott-Hubbard insulator), which will be discussed in the following paragraphs.

2.1.1 Hubbard Model

The $3d$ transition-metal oxide systems, in which the electronic correlations have a strong effect, are generally associated with small values of bandwidth (narrow bands). The Mott-Hubbard model is an important theory which describes the electronic properties of these systems and their metal-insulator transition (MIT), i.e, the transition between paramagnetic metal and paramagnetic insulator [7, 8]. The idea of the Hubbard model is based on introducing the Coulomb interaction effect, i.e., the on-site Coulomb repulsion between electrons U, where the electrons will become localized and a Mott-insulator is formed [7, 9].

2.1.1.1 The classical approximations of the Hubbard Model

In order to understand the first explanation of the so-called Hubbard approximation, let us discuss the more extreme cases of the correlated system via the band description [10]: Starting from the insulating phase where U is very large and the density of states (DOS) contains the upper Hubbard band (UHB) located at energy ($\omega{=}{+}U/2$) and the lower Hubbard band (LHB) located at ($\omega{=}{-}U/2$) with a separation gap of about U-$2D$ where D is the half-width of the band (see Figure 2.2). Upon reducing U, there is a critical value U_c where the UHB and the LHB merge together and a metal results. Unfortunately, this model fails to provide a description of the metal consistent with the Fermi-liquid properties (quasiparticle features) [11].

Later this model was improved by Brinkman and Rice [12]. For the metallic phase, it was described as a strongly renormalized Fermi liquid with a reduced low-energy scale of the order ZD, where Z is the quasiparticle residue ($1/Z{=}m^*/m$, where m is the free electron and m^* is the quasiparticle effective mass). With increasing the interaction strength, this energy scale disappears at a critical value U_{BR}, with $Z{\propto}(U_{BR}$-$U)$ and the insulating state is achieved. Accord-

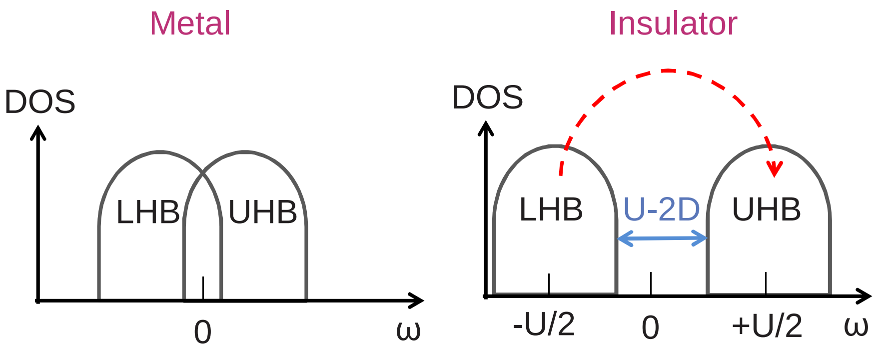

Figure 2.2: Schematic evolution of the density of states (DOS) with U within the Hubbard approximations for both metallic and insulator states [10].

ingly, the metal-to-insulator transition is thus described in terms of localization of the Fermi-liquid quasiparticles. This model gives a simple description of the insulator without taking into account the residual antiferromagnetic exchange and the infinite susceptibility at T=0 K. Furthermore, it describes the low-energy part of the strongly correlated metal in a convenient way, while it ignores the high-energy part which forms the Hubbard bands.

2.1.1.2 Single band Hubbard Model

The Hubbard model is mainly based on two factors: the hopping parameter t which reflects the kinetic energy of the electrons and the on-site Coulomb repulsion U whenever a site is doubly occupied, i.e., having two electrons at the same site. By using the second quantization notation, the Hamiltonian of the single band Hubbard model is defined as follows:

$$\mathbf{H}_{Hubbard} = \mathcal{T} + \mathcal{U} = -t \sum_{\langle ij \rangle \sigma} (c^{\dagger}_{i\sigma} c_{j\sigma} + c^{\dagger}_{j\sigma} c_{i\sigma}) + U \sum_{i} n_{i\uparrow} n_{i\downarrow}, \tag{2.1}$$

where $\mathcal{T}$ and $\mathcal{U}$ are the band term and the interaction term, respectively. i, j are lattice site indices, $\langle ij \rangle$ means a summation over nearest neighbours only. σ is the spin index which takes values of ↑ and ↓. n_i is the band filling and the creation (annihilation) of the single-band electron at site i with the spin state σ which is denoted by $c_{i\sigma}^{\dagger}(c_{i\sigma})$.

The hopping integral within a tight-binding model (t) is supposed to be isotropic and non-vanishing only for nearest-neighbour hopping:

$$t_{ij} = \int \varphi_{i\sigma}^{*}(r)\frac{\hbar^2}{2m}\nabla^2\varphi_{j\sigma}(r)dr, \tag{2.2}$$

where $\varphi_{i\sigma}$ is the Wannier orbital, m is the electron mass, and h is the Planck constant.

The on-site Coulomb repulsion U of two electrons at the same atomic site is presented by:

$$U = \int \varphi_{i\sigma}^{\star}(r)\varphi_{i\sigma}(r)\frac{e^2}{\mid r - r' \mid}\varphi_{i-\sigma}^{\star}(r')\varphi_{i-\sigma}(r')drdr' \tag{2.3}$$

In order to understand the physical meaning of the Hubbard model let us discuss the extreme cases: When the Coulomb interaction between electrons on a given site is vanished (U=0), a half-filled band which is "metallic" will exist and the electrons are delocalized due to the resulting small kinetic energy. Therefore, the site will have a high probability to be doubly occupied. This case is called tight-binding Hamiltonian. The other extreme case is achieved when $U \gg t$, where a single electron will be localized with up or down-spin on each lattice site in order to prevent double occupancy and the system becomes a "Mott-insulator" where the bands split with a gap of nearly about U. Figure 2.3 shows an example of the 3d band splitting. Subsequently, one can note that the ratio U/t is playing an important role in controlling the metal-to-insulator transition. A simple sketch of the two possible ways of inducing a metal to insulator transition is shown in Figure 2.4. From Figure 2.4, it is clear that the MIT is controlled by the competition between the gain of the kinetic energy arising from t and the increase of the Coulomb interaction energy due to the double occupancy of two electrons on the same site (i.e., varying the interaction strength (U/t)). The MIT obtained by the variation of (U/t), can be practically done by modifying the bandwidth (D) via using external parameters, e.g. applying chemical or external pressure. This transition will be defined as a bandwidth-controlled metal-to-insulator transition (BC-MIT). Additionally, the MIT can also be achieved by changing the filling level of the band n_i. This transition can practically be obtained by chemical substitution or intercalation of acceptors or donators. This transition will be defined as filling-controlled metal-to-insulator transition (FC-MIT). It is important to mention here that MIT can also be achieved by varying the temperature which will be explained in detail later within this chapter.

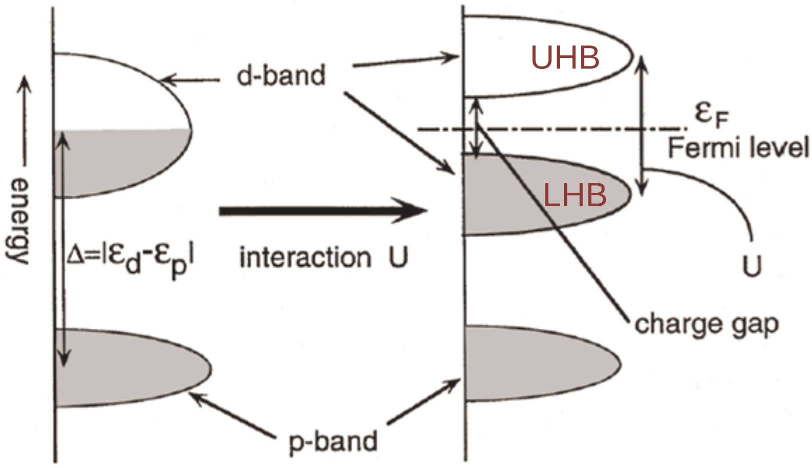

Figure 2.3: The lower Hubbard band (LHB) and upper Hubbard band (UHB), separated by the on-site Coulomb interaction U, resulting from the splitting of the 3d band [1].

The previous estimation of the Hubbard model addresses the case which corresponds to a single band at or close to the half filling where the chemical potential μ will be equal to $U/2$. If we take into account the huge range of the energy scales involved in a system with electronic correlations, in such a case, in order to explain the MIT via the bandwidth-control or the filling-control, there is a need to know the behaviour of the spectral function $A(E)^1$ with increasing the interaction strength (U/t). By applying the Dynamical Mean Field Theory (DMFT) within the Hubbard model, the complexity of a many-particle problem is extremely reduced.

---

[1] $A(E)$ measures the probability of removing /adding an electron from the many-particle system at the energy E below/above the Fermi level

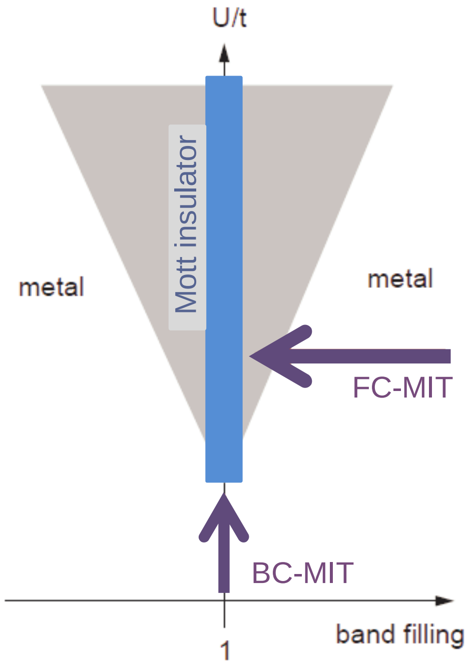

Figure 2.4: Schematic for the Metal-insulator phase diagram based on the Hubbard model in the plane of (U/t) and filling n. Two ways for the MIT are illustrated: bandwidth-controlled and filling-controlled metal-insulator transitions (BC-MIT and FC-MIT). The Mott insulator is found at half-filling ($n = 1$; thick line), the shaded area marks the variation regime [1].

2.1.2 The solution of the Hubbard Model by using the Dynamical Mean Field Theory at T=0 K

For the infinite dimensions, the spectral density as a function of increasing (U/t) was obtained by Refs. [9, 10]. Figure 2.5 shows the spectral density at half filling and T=0 K for a series of values of U. By means of the DMFT, it is possible to fill the gap between the two extreme cases of the (U/t) ratio. Starting from the largest value of (U/t), it can be seen that the two Hubbard bands (LHB and UHB) are separated by an excitation gap U (which is corresponding to the high-energy incoherent excitations), indicating a Mott insulating transition. With decreasing U, the spectral function is characterized by a quasiparticle peak, where the LHB and UHB Hubbard bands are still separated from each other but a transfer of spectral weight from both bands will lead to the appearance of a sharp and narrow quasiparticle peak (which is corresponding to coherent low-energy excitations) around the Fermi energy (ω=0) and below a critical value (U=U_{c2}). Upon decreasing U the quasiparticle peak becomes broader, and below a critical value U=U_{c1}<U_{c2} the resulting overlap between LHB and UHB can lead to a MIT independent of the quasiparticle contribution. In between the two critical values (U_{c1}<U<U_{c2}), a crossover region (intermediate regime) is found. It can be concluded that the Dynamical Mean Field Theory is able to realistically describe the insulating state, the metallic state, and the crossover between them accurately. Additionally, the resulting three-peak structure can be considered as being typical for a correlated metal where a metal-to-insulator transition can also be obtained via a transfer of spectral weight between the low-frequency quasiparticle peak and the high-frequency Hubbard subbands.

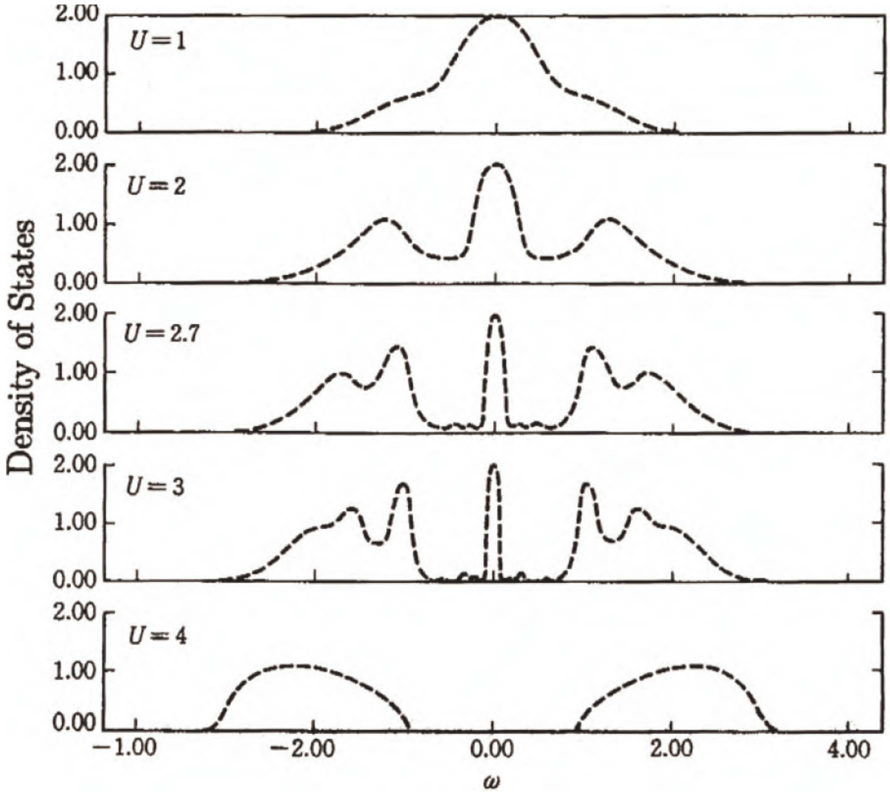

Figure 2.5: Growth of the spectral density of states obtained from the DMFT theory at half filling and T=0 K for a series of values of U, where U is given in units of the half band width ($D/2$). The first four curves (from top to bottom) correspond to an increasingly correlated metal, while the bottom one is an insulator [10].

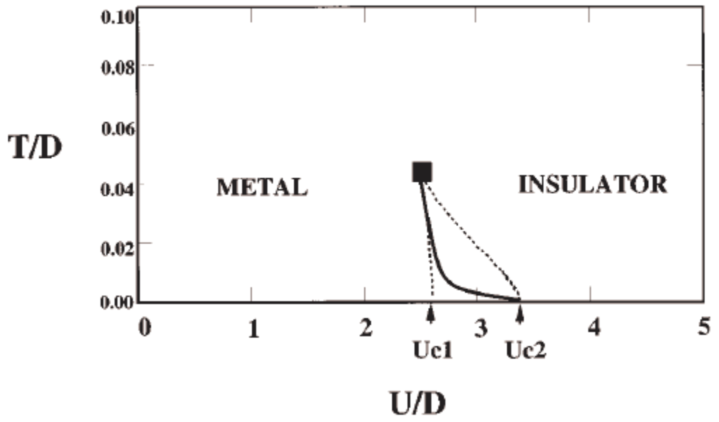

Figure 2.6: Phase diagram of the fully frustrated model at half filling. Within the region delimited with the dashed lines the metallic and insulating solutions coexist. The full line is the approximate location of the real first-order transition line. At high T it is possible to move continuously from one phase to the other since the transition becomes a crossover [10].

2.1.3 The solution of the Hubbard Model by using the Dynamical Mean Field Theory at T≠0 K

In order to have a complete description of the strongly correlated system phase diagram, not only the interaction strength ratio U/t has to be considered for driving the MIT but also both the temperature T and the degree of magnetic frustration (simulated by the ratio of the next-nearest-neighbour hopping amplitude to the nearest neighbor one t_1/t_2) have to be added [10]. Accordingly, four phases were expected, namely: a paramagnetic metallic phase (PM), a paramagnetic insulating (PI) state, an insulating phase with antiferromagnetic ordering (AFI), and an antiferromagnetic metallic state (AFM) with the existence of magnetic frustration.

Figure 2.6 shows the phase diagram of the fully frustrated system, i.e., magnetically ordered phases are not considered since they are suppressed by the magnetic frustration and only the paramagnetic insulator and the paramagnetic metal phases are competing each other. At T=0 K, there can be a clear distinction between the metal and the insulator phases as a function of U. At finite but low temperatures, two paramagnetic solutions were found between $U_{c1}(T) < U < U_{c2}(T)$ (see Figure 2.6). With increasing the temperature, both of U_{c1} and U_{c2} lines were expected to merge at $U_c(T)$. At finite temperature, the actual MIT transition was expected to take place at $U_c(T)$ and the transition is classified as a first order in agreement with the solution of the Hubbard model by using the DMFT.

The Hamiltonian of the Hubbard model for a frustrated square lattice at half-filling is given by:

$$\mathbf{H} = -t_1 \sum_{\langle ij\rangle\sigma} (c^\dagger_{i\sigma} c_{j\sigma} + c^\dagger_{j\sigma} c_{i\sigma}) - t_2 \sum_{\langle ij\rangle\sigma} (c^\dagger_{i\sigma} c_{j\sigma} + c^\dagger_{j\sigma} c_{i\sigma}) + U \sum_i n_{i\uparrow} n_{i\downarrow} - \mu \sum_{i\sigma} c^\dagger_{i\sigma} c_{i\sigma}, \quad (2.4)$$

where t_2 and t_1 are describing the hopping around and along one diagonal of the square plaquettes, respectively.

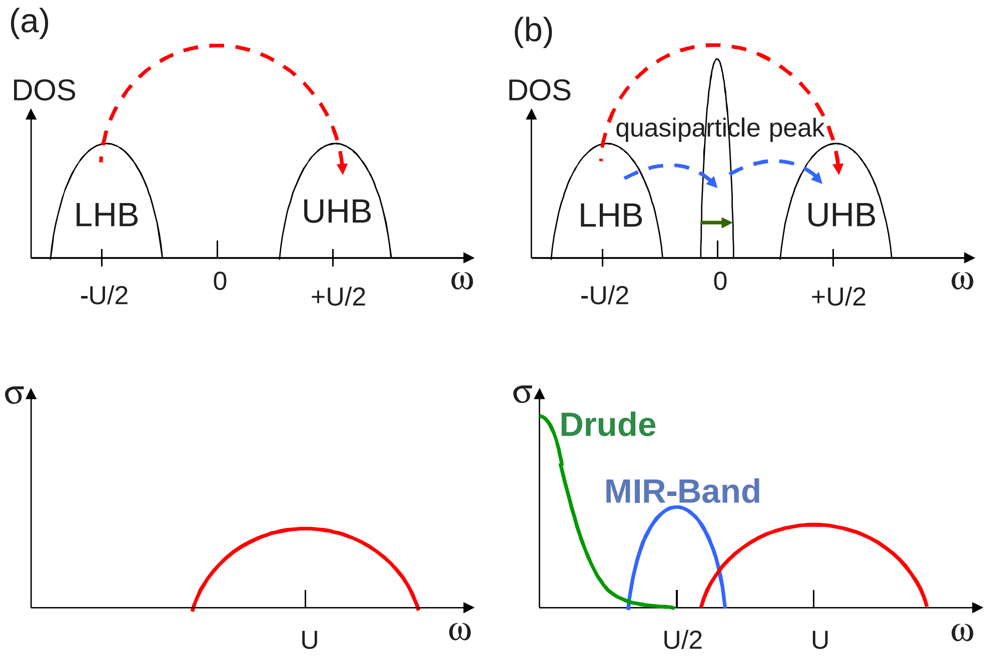

Figure 2.7: Schematic DOS (1/2 filling) and their corresponding optical spectra for (a) the insulator and (b) the metallic solutions [13].

The solution of the Hubbard model by using the DMFT [8, 13–16] predicts that at temperature higher than a critical temperature T_{coh}, where $T_{coh} \ll D$ and close to the first-order Mott transition temperature, a crossover from a metallic-like solution to an insulator-like solution exists, where this crossover region is very narrow (see Figure 2.9). This indicates the absence of a real transition within this region, where the quasiparticle peak is suppressed rapidly and in some reports there is no existence of the quasiparticle peak [8, 10]. Therefore, an incoherent excitation will appear in the optical conductivity spectra as shown in Figure 2.7(a). In contrast, at temperatures below T_{coh}, the quasiparticle peak will appear around the Fermi energy and the Fermi-liquid description will apply. As a result, an insulator-to-metal transition is expected where coherent excitations will appear in the optical conductivity spectra and a transfer of spectral weight to the low-frequency end of the optical conductivity spectrum is predicted. Therefore, it was concluded that the temperature T_{coh} defines an energy scale at which there is a crossover from the coherent excitations to the incoherent excitations where the quasiparticle peak is vanished gradually with increasing the temperature (see Figure 2.8) [14].

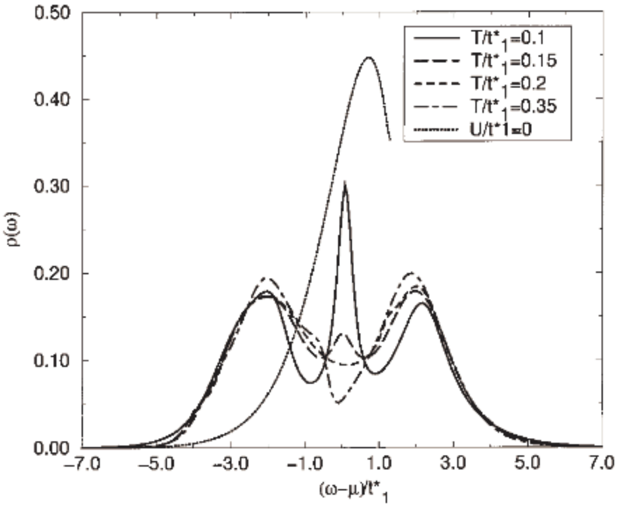

Figure 2.8: The temperature dependence of the spectral density of the strongly correlated metallic phase of a Hubbard model at half-filling and in large dimensions. The results shown are for U=4$t_1^\star$ and a degree of magnetic frustration of $t_2^\star$=0.3$t_1^\star$ [14].

Therefore, the phase diagram of the more realistic cases has to be modified as shown in Figure 2.9, where the system has a partial magnetic frustration and the crossover regime is present. Within the presence of partial magnetic frustration, a transition from an AFI phase to an AFM phase is possible in the case of small value U, where the Néel temperature (T_N) in the metallic phase is predicted to be smaller than in the insulating phase.

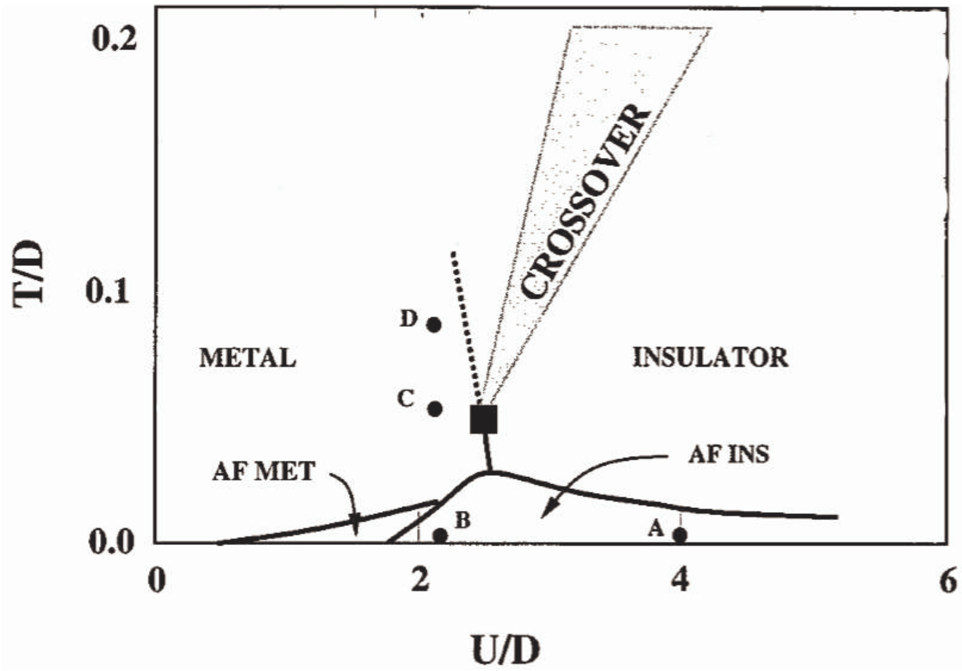

Figure 2.9: Approximate phase diagram predicted by the model with nearest-neighbour (t_1) and next-to-nearest-neighbour hopping (t_2) ($t_1/t_2 = \sqrt{1/3}$). The first order paramagnetic metal to insulator transition ends at the critical point T_{coh} (square) [10].

Accordingly, as shown in Figure 2.7(b) the DMFT predicts that at temperatures below T_{coh}, i.e., the temperature at which the quasiparticle resonance is formed, the optical conductivity spectrum will consist of the following contributions: A Drude term which will start to appear due to transitions within the quasiparticle resonance, a mid-infrared band due to the transition from the lower Hubbard band to the unoccupied part of the quasiparticle peak and from the occupied part of the quasiparticle peak to the upper Hubbard band, and a high frequency band due to the excitations from the lower Hubbard band to the upper Hubbard band [10, 13, 16].

These theoretical predictions of the MIT were verified by optical conductivity measurements on single crystals of the quasi-two-dimensional organic charge-transfer salt [κ^{-}(BEDT-TTF)$_2$Cu[N(CN)$_2$]Br$_x$Cl$_{1-x}$] [15, 17] via varying the Br content. From the optical conductivity spectra a development of the Drude-like contribution was observed indicating the metallic behaviour for Br contents of x= 0.73, 0.85, 0.9 during cooling down to T=20 K, which is below the first-order electronic phase transition. In contrast, for the Br content of x=0, 0.4 no Drude peak was observed during cooling down to 20 K which is consistent with a Mott insulator. Furthermore, the theoretical calculation by using the DMFT for this compound predicts that the optical conductivity spectrum will consist of: A Drude peak a ω=0, a broad absorption band due to the electronic transitions between Hubbard bands at around ω=2000 cm$^{-1}\approx$ U where U=10$|t_2|$=0.3 eV, and a band at ω=$U/2$ due to the transitions between the quasiparticle peak and Hubbard bands. Figure 2.10 shows a comparison between the optical conductivity spectra obtained from both the theoretical and experimental data where two discrepancies were observed: First, the Drude weight for the calculated data disappears at a temperature of about two times greater than the experimental one. Second, the band at ω=$U/2$ was not observed experimentally.

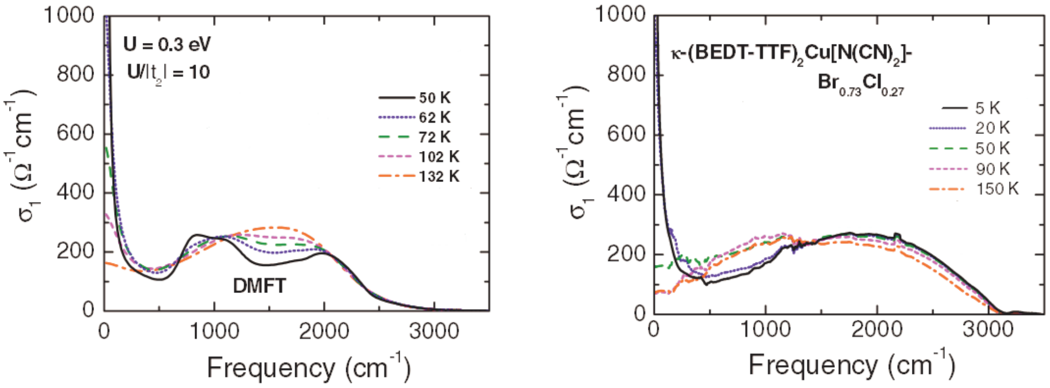

Figure 2.10: The frequency dependence of the optical conductivity at several temperatures of [κ^{-}(BEDT-TTF)$_2$Cu[N(CN)$_2$]Br$_x$Cl$_{1-x}$] (a) Calculations are based on the DMFT treatment of the Hubbard model on the anisotropic triangular lattice for U=0.3 eV [15]. (b) Experimental data for the c polarization axis [17].

Furthermore, the metal-to-insulator transition was observed experimentally in many transition-metal oxides. One of the most famous examples which exhibit such a transition is V_2O_3. At T_{MIT}=160 K, it undergoes a phase transition from a high-T metallic phase to a low-T insulator phase. This transition is associated with lattice distortion and antiferromagnetic ordering at low T [10].

Figure 2.11 shows the phase diagram of the studied chemical substitutions in $(V_{1-x}M_x)_2O_3$ with Cr and Ti ions. The solid line represents the phase boundary of the first order transition. The phase diagram shows three thermodynamic phases: paramagnetic metallic phase (PM), antiferromagnetic phase, and paramagnetic insulating phase (PI) [10, 18, 19].

- For Ti-doping: T_{MIT} decreases with increasing the Ti content where it approximately vanishes at x=0.05 and the metallic phase exists for the Ti content of x>0.05 for the whole temperature range.

- For Cr-doping: At x=0.01 three transitions are observed from the high-temperature side: PM phase to PI phase, PI phase to antiferromagnetic insulator phase, and PM phase to antiferromagnetic insulator phase. With increasing the Cr content to x=0.018, $(V_{1-x}Cr_x)_2O_3$ has two transition from paramagnetic metal to paramagnetic insulator phase and from PI phase to antiferromagnetic insulator phase.

- By applying pressure to Cr-substituted samples the paramagnetic metallic phase is recovered at room temperature. With an external pressure, as a first approximation, the ratio U/t is decreased due to the increase of the hopping integral. Therefore, the net effect of an external pressure is that to increase the kinetic energy of the carriers, thus reducing the effect of U on the system.

2.2 Electron-phonon interaction

Another fundamental interaction which could change the character of the electronic states and hence the optical properties of the transition metal oxides, is the electron-phonon interaction. The electron-phonon (el-ph) interaction describes the interaction between the electron and the lattice vibrations, which could lead

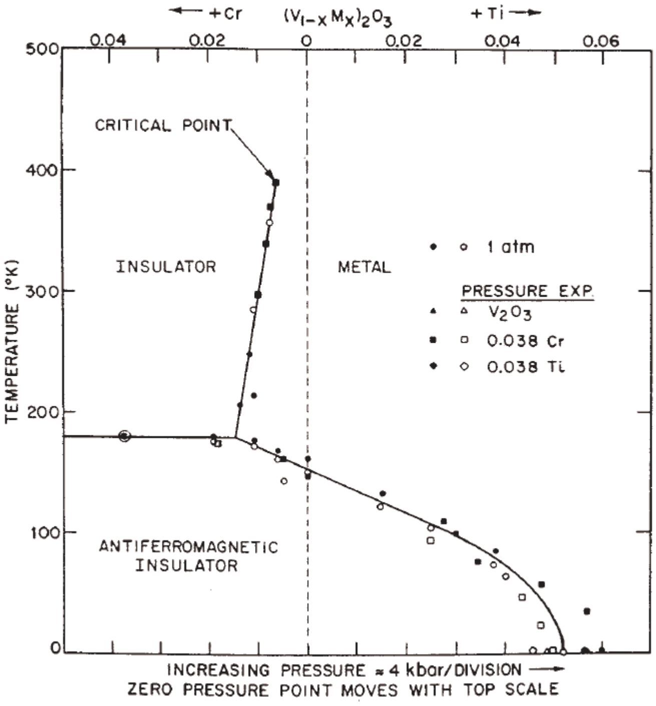

Figure 2.11: The phase diagram which shows the MIT in $(V_{1-x}M_x)_2O_3$ based on different experimental conditions (e.g., various Ti and Cr compositions, temperature, and pressure) [10, 18, 19].

to a MIT in the transition-metal oxide compounds, such as the Peierls transition and superconductivity. The electron-phonon interaction is expected to be large for soft lattices; while the strength of the random potential can be modified by alloying and/or by removing the underlying lattice periodicity by making an amorphous solid [20]. The Hamiltonian for the general case is written as:

$$\mathcal{H} = \mathcal{H}_{el} + \mathcal{H}_{ph} + \mathcal{H}_{el-ph} + \mathcal{H}_{el-el}, \tag{2.5}$$

where the kinetic energy of both the electron and the phonon (lattice vibrational) are represented by the first two terms, while the electron-phonon and the electron-electron interactions are represented by the last two terms, respectively.

The phonon effect on the movement of electrons is considered as a perturbation. Accordingly, there are various types of electron-phonon coupling interactions (due to the existence of several methods for perturbing the motion of electrons) such as:

- Fröhlich interaction, i.e., Coulomb interaction between electrons and the longitudinal electric field produced by the longitudinal optical (LO) phonons.
- Deformation-potential interaction (with both optical and acoustic phonons) and piezoelectric interaction (with acoustic phonons), i.e., the displacement of atoms from their equilibrium positions, which affects the electronic band structure, similar to the effect of applying pressure [21].

During our discussion about the electron-phonon interaction, some attention should be given to polarons. Hence, in several transition-metal oxide compounds, an evidence of the existence of a mid-infrared optical conductivity band which results from the electron-phonon interaction, associated with the polaronic nature of the charge carriers, was observed [22, 23, 23, 24].

2.2.1 Polaron

The concept of the polaron was introduced into physics by Landau in 1933 [25], where he proposed that the local deformation of ions due to the displacement from their equilibrium positions (caused by the electron itself) will create a potential well. As a result, the electrons will be trapped within the potential wells, even in a perfect crystal lattice, where the characteristic phonon frequencies are sufficiently low. This self-trapping phenomenon (an electron dressed by a phonon cloud) is called polaron. These dressed electrons could be excited out from the potential well via absorbing radiation. As the dressed electrons move through the ionic crystal the distortions which are induced by the electron-phonon coupling will be transferred. As a result, the polaron mass will change during this movement creating a quasiparticle, with strong effects by the strength and nature of the el-ph interaction. In several studies the polaron formation was discussed within the adiabatic concept, where the electronic carrier is supposed to adjust to the instantaneous positions of the atoms in the solid [26–28]. Quantitatively, there are several physical properties which characterize the polaron such as its effective mass, binding or(self-) energy, and its response to external electric and magnetic fields. According to these properties the polaron can be classified to different types (e.g, large polaron, small polaron) depending on whether long or short-range electron-lattice interaction prevails in a multidimensional system. The qualitative differences between the large and the small polaron were observed in their electronic transport properties and hence their optical properties. Clear signs of the polaron formation were observed in the optical properties of several materials (e.g.,ferrites, nickelates, titanates, manganites and cobaltites), especially the appearance of a broad absorption band in the mid-infrared frequency range which was attributed to the polaronic nature, which was called polaronic band [29].

2.2.1.1 Large Polaron

In many materials, when the polaron radius R^1 is very large compared to the lattice constant a (i.e., self-trapped carrier involves multiple sites), the quasiparticle will be called large polaron (or Fröhlich polaron). The large polaron (LP) is usually formed when the electron-phonon coupling is weak, i.e., the electron is lightly dressed by a wide band Bloch state which leads to an increasing polaron radius. The LP is characterized by the slight increase of its effective mass, the large mobility (μ >1 cm^2/Vs) which drops with increasing the temperature, and the prevailing long-range electron-lattice interaction which is called Fröhlich interaction [30]. The electron-phonon interaction for the large polaron (Fröhlich coupling constant α) is given by:

$$\lambda = \frac{e^2}{\hbar}\sqrt{\frac{m}{2\hbar\omega_0}}[\frac{1}{\epsilon_\infty} - \frac{1}{\epsilon_0}], \tag{2.6}$$

where ϵ_∞ and ϵ_0 are the high-frequency and the static dielectric constants, respectively. ω_0 is the frequency of the longitudinal optical phonon. For the weak coupling regime (i.e., at λ <1), the perturbation-theory provided by Fröhlich predicted that the large polaron formation lowers the electron energy by:

$$E_p = -\lambda\hbar\omega_0 \tag{2.7}$$

---

[1] R is the ratio of the electronic bandwidth of the free electronic carrier to the binding energy of a carrier with radius a [26].

Generally, the photoionization process is used for exciting self-trapped carriers from their ground state of the potential well via photon incidence. Figure 2.12(a) shows the photoionization diagram for an adiabatic LP. Hence, the excitation energy for the photoionization corresponds to the electronic binding energy of the self-trapped carriers. Accordingly, for the LP, the self-trapped carriers will be excited from their bound ground state to unbound (continuum) states with a threshold photon energy equal to $3E_p$, where E_p is the electronic binding energy of the self-trapped carriers. Furthermore, the photoionization spectrum for the LP shows a temperature-independent absorption band in the mid infrared frequency range (see Figure 2.12(b)). This absorption band is asymmetric where its peak has more intensity on the high-frequency side than on the low-frequency side and this peak position is approximately given by

$$\omega_p = 3E_p/\hbar \tag{2.8}$$

Therefore, by knowing the peak position of the polaronic band one can also determine the polaron binding energy. This polaronic absorption peak shifts to higher frequencies as the size of the LP decreases.

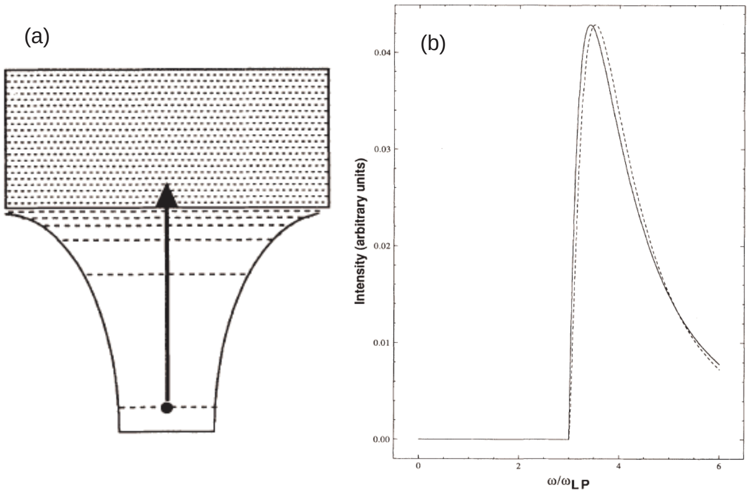

Figure 2.12: (a) The photoionization diagram for the optical transition of an adiabatic LP from its bound ground state to unbound state. (b) The photoionization absorption spectrum of the three-dimensional (solid curve) and the two-dimensional (dashed curve) LP as a function of frequency [26].

For a theoretical description of the optical properties of LP, a phenomenological approach is used [26], where the absorption coefficient per polaron density is described by:

$$\alpha/n_p = \frac{128e^2\pi}{3mc\omega}\frac{(\kappa(\omega)R)^3}{[1+(\kappa(\omega)R)^2]^4}, \tag{2.9}$$

where R is the radius of the hydrogenic ground state of the polaron and n_P is the density of the polaron. m is the mass of the photoionized carrier and the effective mass is given by Richard Feynman [31]:

$$m^\star = m(1+\alpha/6) \tag{2.10}$$

The wave vector $k(\omega)$ is defined as

$$k(\omega) = \sqrt{2m(\hbar\omega - 3E_P)}/\hbar = \frac{2\pi\sigma_1(\omega)\mu_1}{n\omega}, \tag{2.11}$$

where $\sigma_1(\omega)$ is the optical conductivity of LP, μ_1 is the magnetic permeability, and n is the refractive index. Hence for the weak coupling regime:

$$\alpha = \frac{2k\omega}{c} \tag{2.12}$$

By substituting from equations (2.11) and (2.12) into (2.9). In the case of μ_1=1 and n=2, the optical conductivity of the large polaron suggested by Emin due to the photoionization of the charge carriers from the self-trapped to the free carrier state is described by [26, 32]

$$\sigma_1(\omega) = n_P\frac{64}{3}\frac{e^2}{m}\frac{1}{\omega}\frac{(k(\omega)R)^3}{[1+(k(\omega)R)^2]^4} \tag{2.13}$$

Another contribution of the LP which appears in the optical conductivity spectra is a Drude-like contribution at low frequencies due to itinerant motion of the polaron, similar to that of free charge carriers. This contribution is created by the coherent motion of large polarons. Hence, the self-trapped carrier of a large polaron extends over multiple sites, the self-trapped carrier can continuously adjust to alterations of the atomic positions and thereby move between the sites.

Therefore, the large polarons can move coherently and the coherent motion is associated with classical motions of atoms [26].

2.2.1.2 Small Polaron

On the other hand, when the distorted lattice is localized within a few sites of the electron (i.e., it collapses to a single site), the quasiparticle will be called small polaron (SP). This concept was introduced by Holstein where his model consists of tight-binding conduction electrons interacting with local dispersionless phonon modes [27]. The small polaron is usually formed when the electron-phonon coupling is strong, i.e., the electron is strongly localized and is described by a sequence of narrow bands separated by the phonon excitation energy. Accordingly, the polaron radius R may become approximately equal to the interatomic lattice constant a. The SP is characterized by the large increase of its effective mass, the small mobility ($\mu \ll 1$) which decreases with increasing the temperature, and the prevailance of the short-range lattice order [27].

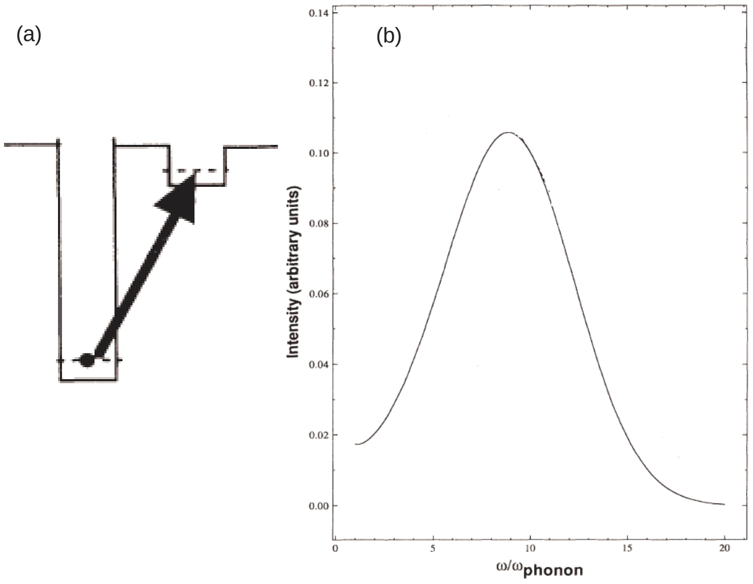

Figure 2.13: (a) The photoionization diagram for the optical transition of an adiabatic SP. (b) The photoionization absorption coefficient per SP at T=0 K as a function of ω/ω_p [26].

For the SP, the absorption spectrum of the photoionization process is due to the hopping of the self-trapped carrier from its localized state to a localized state at a site neighbouring to the small polaron site. Figure 2.12(a) shows the photoionization diagram for an adiabatic SP. For equivalent sites, the excitation energy for the transition between two sites is corresponding to the reduction of the electronic energy associated with the SP formation. It is approximately twice the bound state energy of the small polaron (i.e, $2E_p$). The photoionization spectrum will show generally a temperature-dependent absorption band in the mid infrared frequency range (see Figure 2.13(b)), where for the low temperatures the SP behaves like a free particle, while for high temperature it moves by thermally activated hopping with enhanced mass [33]. This absorption band has asymmetric shape where the intensity of the peak from the low frequency side is higher than the high frequency side, which is opposite to the one of the LP. The position of this peak is approximately at

$$\omega_p \approx 2E_p \tag{2.14}$$

Therefore, the polaron binding energy can be determined from the peak position of the polaronic band in the optical conductivity. Hence the broadening of the SP absorption band is produced by atomic vibration, therefore with decreasing temperature the broadening of the polaronic absorption peak (the mid infrared band) decreases.

Additionally, unlike the LP, the movement of the SP is associated with the quantum-mechanical tunneling of atoms which leads to the resonance energy associated with the coherent movement of SP being very small compared to the disorder energies. Accordingly, the coherent motion of the charge carriers of the SP is suppressed in real materials and the Drude contribution due to the SP will not be observed in the optical conductivity where the spectrum will consist only of the mid infrared band due to the photoionization of SP.

Within this piece of work, the optical conductivity of SP obtained from the Holstein model [27] which is reinvestigated by using the Fratini model [28], where the concept of the DMFT is applied to the Holstein model, will be discussed. In Fratini's model the polaron formation as mentioned above is depending on the adiabatic ratio

$$\gamma = \omega_0 / D, \tag{2.15}$$

where ω_0 and D are the avarage phonon frequency to which the electrons couple and the half of the free electron band width, respectively. Depending on the value of the adiabatic ratio, it is possible to differentiate between adiabatic and antiadiabatic regimes. Moreover, the analytical expressions for the small polaron contribution to the optical conductivity in the adiabatic regime based on DMFT have been interpreted by several authors [28, 34] depending on the ratio between the bandwidth D and the variance s of the phonon-induced broadening of the electronic levels:

$$s^2(T) = E_P \omega_0 \coth \omega_0/(2T) \tag{2.16}$$

By checking both of the boundaries ($s \gg D$, and $s \ll D$) it was found that:

- For $s \gg D$: The phonon induced broadening of the electronic levels will be very big compared to the electronic dispersion. The simplest formula of the absorption by small polaron at sufficiently high temperature $T \geqslant \omega_0/2k_B$ (k_B is Boltzmann constant) described by a Gaussian-shaped peak centered at $\omega_{max}= 2E_P$ is given by [35–37]

$$\sigma_1(\omega, \beta) = \sigma(0, \beta) \frac{\sinh(\frac{1}{2}\omega\beta)}{\frac{1}{2}\omega\beta} \exp[-\frac{\beta\omega^2}{16E_{\mathrm{A}}}], \tag{2.17}$$

  where $\beta = 1/(k_B T)$ and $E_{\mathrm{A}}=E_P/2$ is the thermal activation energy for hopping conduction of the carrier across the potential barrier.

- For the opposite limit ($s \ll D$): The transition will be from a polaronic state with energy $\approx$ -$2E_p$ to a continuum state and the electronic dispersion will control the line shape. The absorption by small polaron is described by [28]

$$\sigma_1(\omega) \propto \frac{1 - e^{\omega/T}}{\omega} \Phi(\omega - 2E_P) N(\omega - 2E_P), \tag{2.18}$$

  where the function $\Phi(\epsilon)$ is the corresponding current vertex which can be derived by

$$\Phi(\epsilon) = (D^2 - \epsilon^2)/3, \tag{2.19}$$

and the density of states $N(\epsilon)$ is assumed to be semielliptical of the half-band width D:

$$N(\epsilon) = \frac{2}{\pi D^2}\sqrt{D^2 - \epsilon^2} \tag{2.20}$$

Hence, the finite band width effects were taken into account in Eqn.(2.18). So the position of the mid infrared absorption band in this model will be lower than $2E_P$, where it will be located at

$$\omega_{max} = 2E_P - D^2/2E_P, \tag{2.21}$$

meaning that the mid-infrared absorption band will shift to lower frequencies relative to $2E_P$.

Furthermore, the conduction mechanism due to the hopping of the SP is an effective tool for the quasiparticles related to transport. If the conduction mechanism is due to the hopping of the small polaron in adiabatic regime, the thermally activated behavior of the dc conductivity will described by [33, 38]

$$T\sigma(T) \propto \exp[-E_H/(k_B T)], \tag{2.22}$$

where E_H is the hopping energy which given by

$$E_H = \frac{E_p}{2} - t = E_A - t, \tag{2.23}$$

where t is the electronic transfer integral.

Figure 2.14 shows an example of the fitting by using equation (2.22) for the data of as-deposited $La_{0.7}Ca_{0.3}MnO_3$ film on Si. The data are fitted well in a limited temperature range above the Curie temperature T_c, while at higher temperatures clear deviations were observed [38].

As mentioned before, the polaronic band was observed in the optical prop-

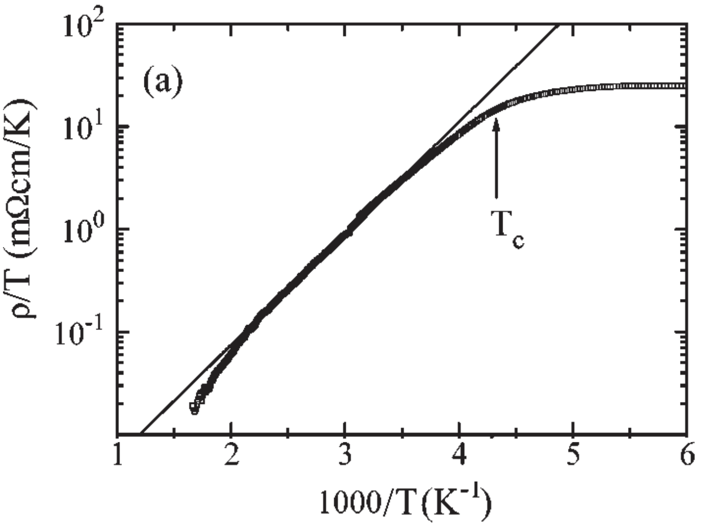

Figure 2.14: Fit of the ρ/T as a function of inverse temperature for the as-deposited $La_{0.7}Ca_{0.3}MnO_3$ with equation (2.22). The polaron model fits the data in the limited temperature range above T_c (solid line), but clear deviations are apparent at high temperatures [38].

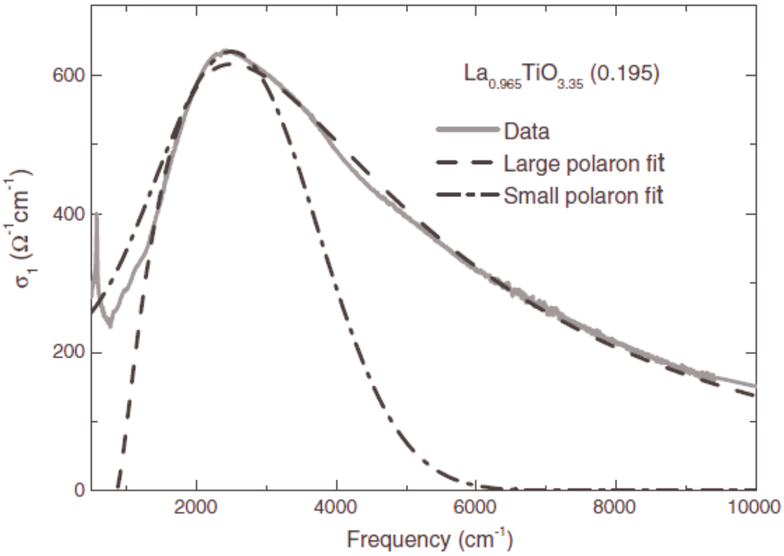

Figure 2.15: Fit of the mid infrared absorption band of $La_{0.965}TiO_{3.4}$ (0.195) with large and small polaron models according to equations (2.13) and (2.17), respectively [39].

erties of several materials. As an example, the optical conductivity spectra of $La_{1-y}Ca_yTiO_{3.4\pm\delta}$ along the conducting chain direction showed this absorption band around 2500 cm^{-1}. Figure 2.15 shows the fitting of this band by using Eq. (2.13) and Eq. (2.17) which are describing the large and the small polaron models, respectively. For the large polaron model, the best fitting was obtained with the parameters n_p=9.18×10^{20} cm^{-3}, E_p=284.5 cm^{-1}, and R=2.23 Å. For the small polaron model, the parameters $\sigma(0,\beta)$=226.5 Ω^{-1} cm^{-1}, and the polaron binding energy=1994 cm^{-1} were obtained. From the fitting it was concluded that the large polaron model described the shape of the mid infrared absorption band well [39].

2.2.1.3 Polaron crossover in the adiabatic regime

With increasing el-ph coupling, the transformation from the LP to the SP via an intermediate crossover regime was predicted analytically by the DMFT [28]. Figure 2.16 shows the phase diagram of the different regimes obtained from the Fratini model [28] depending on the optical conductivity equations for the weak and strong coupling regimes which were explained above. Hence, there is no analytical expression for this regime, therefore here we will focus on the optical properties in the adiabatic polaron crossover region (the gray shaded region in the phase diagram). This intermediate region (crossover region) is characterized by the coexistence of both the weak coupling and the strong coupling regimes. Therefore, at low temperature the DMFT predicts that the optical conductivity will show a transfer of spectral weight between these two regimes. Additionally, in the low frequency part of the optical conductivity (of the order of the phonon frequencies) several narrow absorption features are predicted to appear. These peaks are denoted as polaron interband transitions (PIT). They are purely electronic in nature and due to the transitions between different subbands in the polaron excitation spectrum. These peaks have monotonic temperature dependance (see Figure 2.17).

Experimentally, these PIT were observed in the optical spectra of several materials [41, 42]. Figure 2.18 shows the optical conductivity spectra of β-$Sr_{0.17}V_2O_5$ along the b direction at T=10 K with the fitting by using the small polaron models

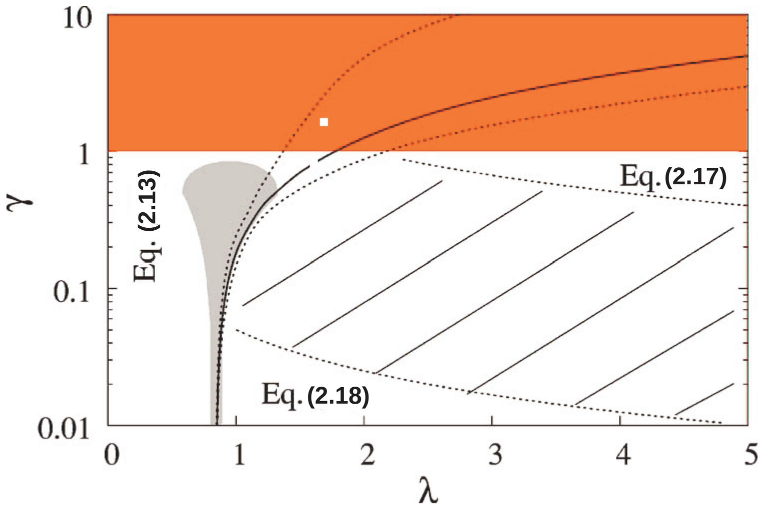

Figure 2.16: The phase diagram which illustrates the different regimes at T=0 K of different limiting formulas: Eq. 2.13 for weak coupling regime, Eq. 2.18 for strong coupling adiabatic regime regime $s \ll D$, and Eq. 2.17 for strong coupling adiabatic regime $s \gg D$. The bold and dotted lines indicate the location and spread of the polaron crossover obtained in Ref. [40]. In the hatched region at $\gamma < 1$, the optical conductivity is not accessible by the strong coupling adiabatic theory. This region is delimited by two lines: the bottom line represents the s/D=0.05 and the upper line represents the s/D=2. The gray shaded region indicates the adiabatic intermediate regime [28].

according to equation 2.18. The optical conductivity spectrum at low temperatures consists of a mid-infrared absorption band (which narrowed and shifted to lower frequency with decreasing temperature) and several relatively narrow peaks (which appeared in the far-infrared range at low temperature). By applying the concept of the DMFT of the small polaron it was found that this compound refers to an adiabatic small polaron in the intermediate e-ph coupling regime, where they estimated the adiabatic ratio $\gamma \approx 0.2$, polaron binding energy $E_p \approx 0.4$ eV, and coupling strength $\lambda \approx 0.8$. Therefore, the observed far-infrared peaks were attributed to be polaronic interband transitions.

One of our goals is to study the nature of the polaronic band in magnetite by using different theoretical polaron investigations which will be discussed in detail in chapter 4. Furthermore, in some systems it was found that one of the two interactions (electron-electron interaction and/or electron-phonon interaction) are dominant as a driving force of the metal-insulator transition. However,

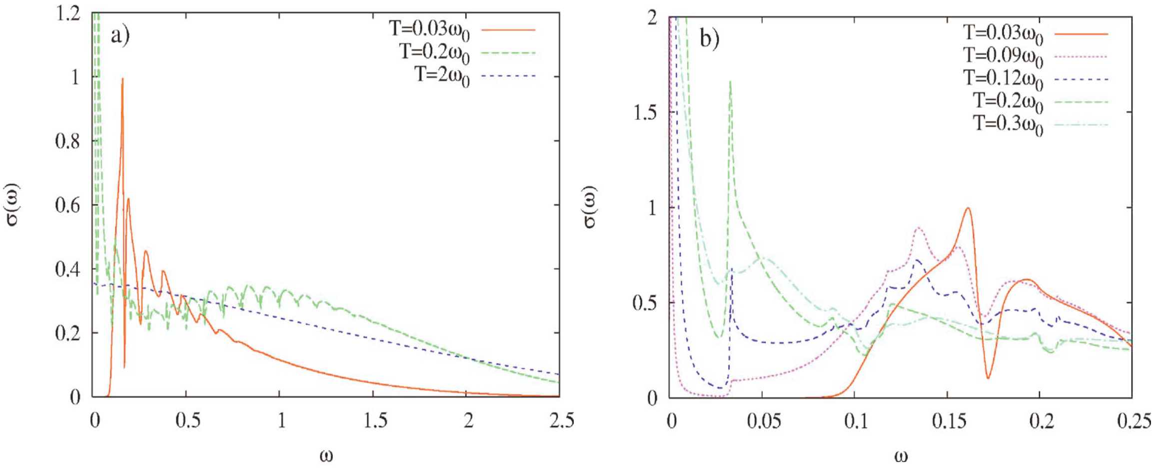

Figure 2.17: Optical conductivity in the adiabatic regime γ=0.1, at an intermediate value of the coupling strength =0.9. (a) The absorption changes from a weak-coupling-like at low temperature to a strong-coupling-like at high temperature, leading to a monoclinic evaluation of the spectral weight. (b) The temperature evaluation around one phonon threshold, where polaron interband transitions appear [28].

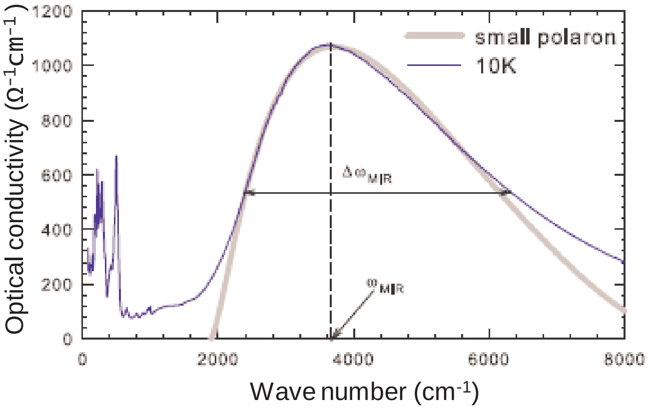

Figure 2.18: Optical conductivity spectrum of β-$Sr_{0.17}V_2O_5$, at T=10 K, with the fitting curve of the mid infrared absorption band by using the small polaron models according to equation 2.18. The vertical dashed line denotes the position of the maximum ω_{MIR} of the mid infrared peak. The horizontal arrow illustrates its half height width $\triangle\omega_{MIR}$ [41].

in other systems, these two interactions compete with each other. The aim of this study is to reveal how these interactions affect the electronic properties of Fe_3O_4 and TiOCl under high pressure and low temperature, which might lead to the strong modification of their physical properties and hence the occurrence of a metal-insulator transition.

Chapter 3

Experimental Procedure

3.1 Introduction

In this chapter, a brief overview will be given about the experimental techniques used in this thesis, in order to characterize the measurements of Fe_3O_4 and TiOCl samples. A general description of the Fourier transform infrared spectroscopy will be illustrated. The experimental devices used to carry out the reflectance and the transmittance measurements as a function of pressure at room temperature and at low temperature will be described. The explanation of the theoretical basis used for the analysis and interpretation of the results will be given.

3.2 Fourier transform infrared spectroscopy

Fourier transform infrared spectroscopy [FT-IR] is the most useful technique for obtaining a fast and a perfect spectral analysis of the electromagnetic radiation [43, 44]. It is an analytical technique used to identify materials that are either organic or inorganic. This technique allows us to detect the absorption and the reflection properties over an extremely broad spectral range starting from the far-infrared up to the ultraviolet.

3.2.1 Basic principle

The FT-IR is an adaption of the Michelson interferometer, that consists of a fixed mirror, a moving mirror, and a beamsplitter. As shown in figure 3.1 the radiation from a broad band IR-source is collimated and directed into the interferometer source where it is divided by the beamsplitter into two beams which are then sent to the two mirrors. The two mirrors reflect the beams back along the same paths, hence they recombine at the beamsplitter where they interfere in order to proceed to the sample area and fall on the detector.

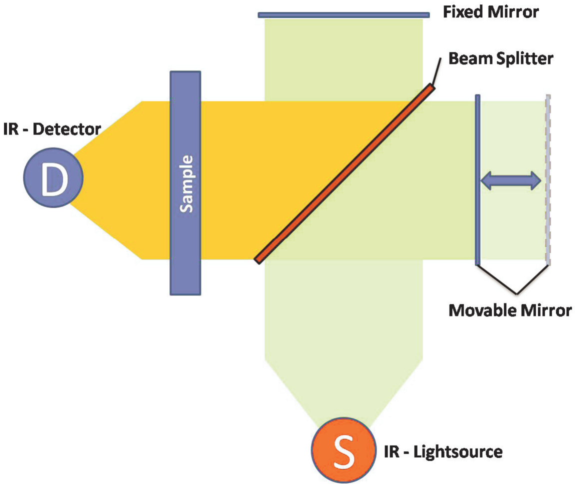

Figure 3.1: Schematic diagram of the beam path through the Michelson Interferometer.

If the two beams have a path difference (δ) between them, an interference pattern will be generated. The resulting intensity of the recombined beams $I(\delta)$ is measured as a function of the optical path difference between the two mirrors and is called the interferogram [45, 46]. The IR spectrum can be obtained by calculating the Fourier transform (FT) of the interferogram. For more explanation, let us take the case of the monochromatic source as an example: If the two splitted beams travel through exactly the same path length, then the two beams are completely in phase with each other; thus they interfere constructively leading to a maximum in the detector response. Otherwise, the interference is destructive when the two beams are 180° out of phase to each other. Therefore,

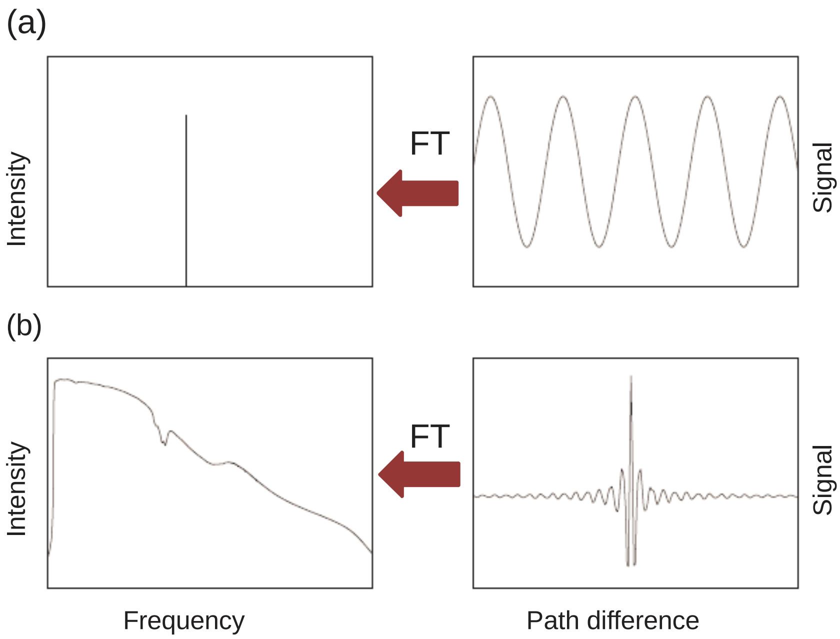

Figure 3.2: A typical interferogram and its corresponding spectrum (a) For a monochromatic source (b) For a typical infrared source.

the detector output will alternate in a cosinusoidal way between the maximum equal to the incoming intensity and zero. Figure 3.2(a) displays the interferogram for the monochromatic beam and its transformed spectrum using FT.

For a typical infrared source, the emitted spectrum will be continuous and the obtained interferogram will be described mathematically by [47]:

$$I(\delta) = \int_{-\infty}^{\infty} B(\nu) \cdot \cos(2\pi\delta\nu) d\nu, \tag{3.1}$$

where the Fourier transform $B(\nu)$ is the intensity or the brightness of the source as a function of frequency ν which is given by the following formula:

$$B(\nu) = \int_{-\infty}^{\infty} I(\delta) \cdot \cos(2\pi\delta\nu) d\nu, \tag{3.2}$$

Figure 3.2(b) shows an example of the power spectrum obtained through FT.

Here, it must be noticed that the main advantage of the Fourier transformation is that all the wavelengths reach to the detector simultaneously, therefore, multiple scans of the sample can be done in a very short time, also the signal-to-noise ratio is improved. All details about the principles and the characterization of the FT-IR spectroscopy is found in Ref. [44].

3.2.2 Spectrometer components and operating frequency range

The FT-IR spectrometer consists of three basic components: radiation source, beamsplitter, and detector. In the following each of this components will be illustrated in details [48]:

Radiation sources

There are common radiation sources for the IR spectrometer: All of them produce continuous radiation but with different energy profiles depending on the measurements range. However, the most common types of IR light sources are: Hg discharge lamp which is used for the far-IR region (10- 700 cm^{-1}), Silicon carbide (Globar) source used for the mid-IR region (555- 8000 cm^{-1}), and Tungsten halogen lamp used for the near-IR (3000- 12000 cm^{-1}) and visible (10000- 24000 cm^{-1}) regions.

Beamsplitter

The beamsplitter consists of a thin film deposited on a non-absorbing substrate. For the far-IR region, the beamsplitters are made of Mylar thin films, Ge coated KBr is used for the mid-IR, and Sn_2Sb_3 coated CaF_2 beamsplitters are used for the near-IR and visible regions, respectively.

Detectors

The most popular detectors for FT- IR spectrometer are: Bolometer (silicon-based helium cooled) which is used for the far-IR region, the mercury cadmium telluride MCT (liquid nitrogen cooled) for the mid-IR region, the InSb detector (liquid nitrogen cooled) for the near-IR region, and the Si diode for the visible region.

3.3 Experimental equipments for the high-pressure infrared measurements

In this section, a short description for the experimental devices used to carry out the reflectance and the transmittance measurements involving the high-pressure techniques at room temperature will be given.

3.3.1 Spectrometer

The FT-IR spectrometer Bruker IFS 66v/s was used to carry out the infrared spectroscopy measurements in the present work [48]. The IFS 66v/s Bruker can cover the spectral range from 10 cm^{-1} to 24000 cm^{-1}, i.e. from the far-infrared to the visible frequencies with a maximum resolution of 0.25 cm^{-1}. The detector compartment consists of the deuterated triglycine sulfate (DTGS) detector which works at room temperature, and the MCT detector. In order to avoid the H_2O and CO_2 absorption features, the spectrometer has to be kept under vacuum. The structure and radiation response of the Bruker IFS 66v/s spectrometer is illustrated in Figure 3.3. Here, it must be noticed that in the case of using the synchrotron radiation as a source instead of the spectrometer built-in conventional sources, the position of a plane mirror has to be changed remotely.

3.3.2 Infrared microscope

The incoming light beam from the interferometer can be reflected via a rotating mirror behind the interferometer either to the spectrometar sample chamber or to an infrared microscope connected to the spectrometer (see Figure 3.3). Hence, the sample size in high-pressure experiments is limited by a small size compared with the size of the incoming beam from the spectrometer. Accordingly, a commercial infrared microscope (type of IR-Scope II Bruker) is coupled to the spectrometer in order to focus the IR beam on a specific chosen area from a small sample [49]. Inside the microscope, there are two Schwarzschild objectives with 15x magnification factor, viewing with 4x magnification, and a working distance of 24 mm. One of these objectives is used for focusing the light on the sample,

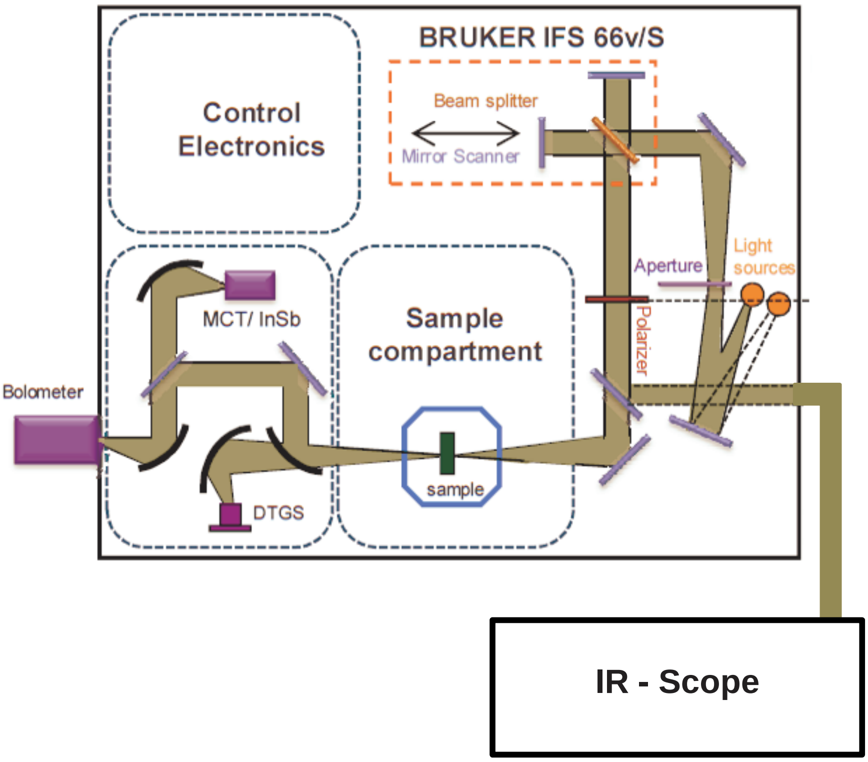

Figure 3.3: Optical layout of the Bruker IFS 66v/s spectrometer [48].

while the second serves as a condenser for the transmission measurements. The microscope is provided with a narrow-band MCT detector and it is possible to replace it with other detectors. The incoming IR beam from the spectrometer is adjusted via several mirrors to be focused to the Schwarzschild objectives and to be redirected further to the detector. Moreover, the mirrors which focus the IR beam to the Schwarzschild objectives are aligned by a particular way that the focus of the IR radiation is coupled to the focus of the visible light of the microscope, i.e. the focus on the sample by the eye is coinciding with the IR radiation. The microscope has apertures which can control the diameter of the IR beam to values between 300 to 3750 μm. The top of the microscope contains two ports, one of them is used as a Camera port in order to allow us to take photos of the samples. The other port is used for collecting the ruby luminescence signal

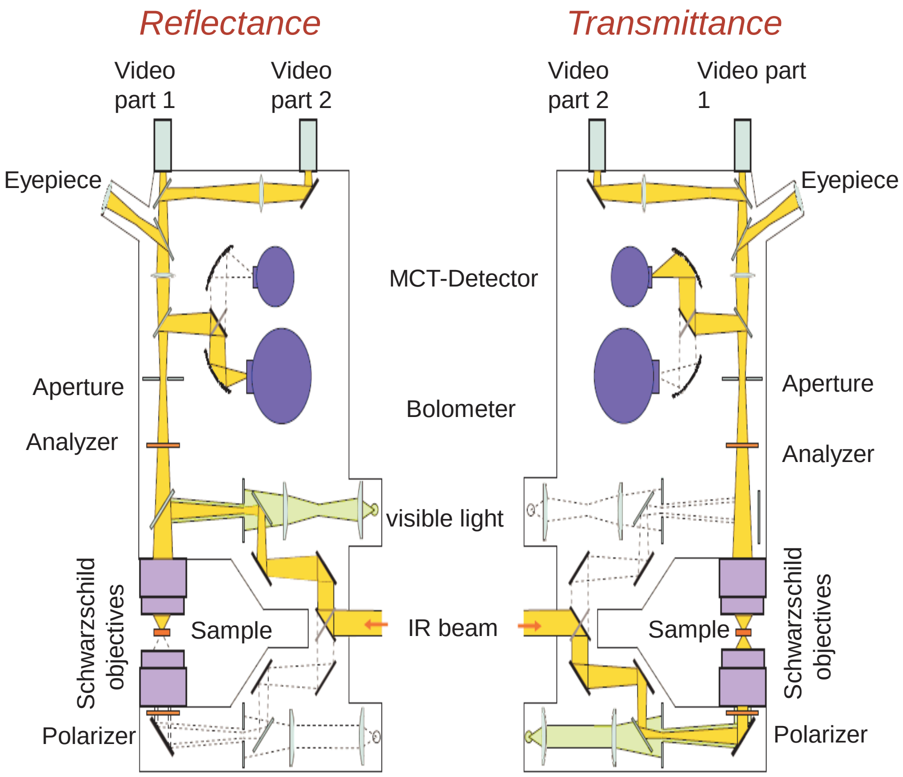

Figure 3.4: Optical layout of the IR Scope II which shows the beam path for both the transmittance and reflectance [49].

during pressure measurements. The microscope can work either for reflection or transmission measurements. The beam path inside the IR microscope for the reflectance and the transmittance modes is illustrated in Figure 3.4.

In the present work, the infrared spectroscopy measurement under high pressure is one of our goals. The measuring procedure of a small sample inside the diamond anvil cell (DAC) was carried out as follows: The DAC has to be mounted inside the microscopes movable sample stage using a home built holder. The aperture has to be kept fixed for all the experimental runs. Furthermore, after aligning the sample inside the DAC in the visible mode, the IR beam has to be maximized by using the mirrors which couple the microscope and the spectrometer.

3.3.3 High-pressure diamond anvil cells

In order to measure the optical properties of a sample placed inside the pressure cell, there must be some basic requirements for the pressure cell design which need to be taken into account:

- The inserted window has to be sufficiently larger than both the spot size of the incoming light and the maximal wavelength of the radiation.
- It must be almost perfect transparent in the whole measured spectrum ranges.
- It must have a high hardness in order to not be damaged by applying high pressures.

Accordingly, the natural diamond is found to be the best candidate for such an optical window. For the infrared spectroscopy measurements the pure diamond type IIA (nitrogen-free) is used. This diamond has the greatest spectroscopic range of transparency as it has only one main multi-phonon absorption in MIR between 1500- 2700 cm^{-1} and partially up to 4000 cm^{-1} as shown in Figure 3.5.

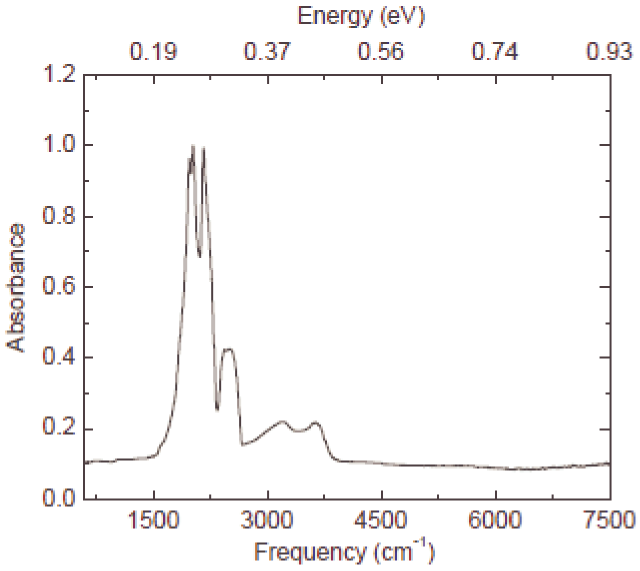

Figure 3.5: Multiphonon excitations of the diamond in the MIR range [50].

The diamond anvil cell (DAC) is the pressure device which allows us to attain static pressures up to several tens of GPa by compressing samples with small volumes. The DAC is very simple in principle, where it basically consists of two brilliant-cut diamond stones which are beveled at the tip (culet) with their large faces (table) resting on flat hard seats to serve as anvil faces [51]. Between the two anvil faces a metallic gasket with a small hole is placed. In this hole (which serves as a sample chamber), the sample is placed with the ruby ball (which is used for the pressure calibration). Then the hole is filled with a suitable pressure transmitting medium (PTM). By applying force (F) on the sample area (A) via the anvil faces, the pressure (P) will be generated according to the general formula ($P = F/A$). Figure 3.6 illustrates the main working principle of the DAC.

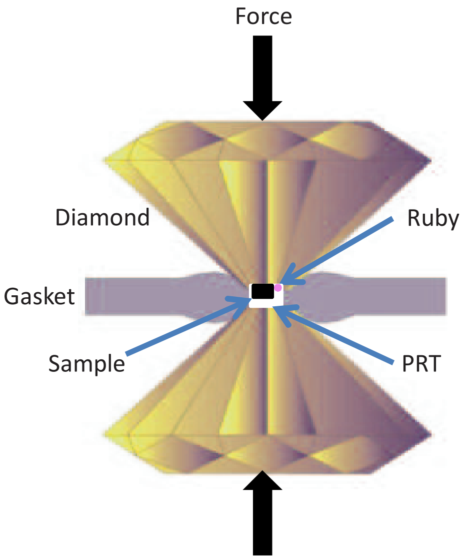

Figure 3.6: Sketch showing the main working principle of the DAC.

The maximum pressure that can be reached with a DAC is depending on several factors [52] such as:

- The area of the anvil faces: The smaller the area of the anvil faces, the higher the pressure P that can be reached by the DAC.
- The parallelism between the culets of the DAC.
- Centering the gasket hole with respect to the culet centers.
- The hardness of the gasket material (e.g. stainless steel, Inconel, and copper beryllium) which gives side support to the conical faces of the anvils.

In the following, a brief illustration about the several types of the DAC used in this work will be given.

CryoDAC Mega cell:

The Diacell CryoDAC-Mega [53] is one of the useful diamond anvil cells for optical and X-ray diffraction studies at cryogenic temperatures designed by easy lab. It is made from a CuBe alloy and it is well suited to be used with FTIR and other types of spectrometers due to its high numerical aperture. The diamond anvils are mounted within force-fitted CuBe rings, and are mechanically fixed to their tungsten carbide support plates, thereby avoiding use of epoxy resins or other adhesives which all tend to be unreliable at very low temperatures. The DAC is held within two CuBe blocks. One of these is fixed to the cryostat cold station and also accepts the cylindrical DAC. The second block fits over the DAC and is used to apply load to the cell by means of four bolts.

The diameter of the complete assembly is 38 mm. The culet diameter in this cell is 800 micron while the diamond thickness is about 1.5 mm. The opening angle of the apertures in this DAC is 50° at both the piston and cylinder assemblies. The maximum pressure that can be achieved in this DAC is about 12 GPa. A gasket made from a CuBe alloy with an initial thickness 0.4 mm is used with this DAC. For applying pressure up to 10 GPa, the gaskets are pressed to a thickness of about 70-80 μm and holes of diameter 300 μm are drilled in these gaskets.

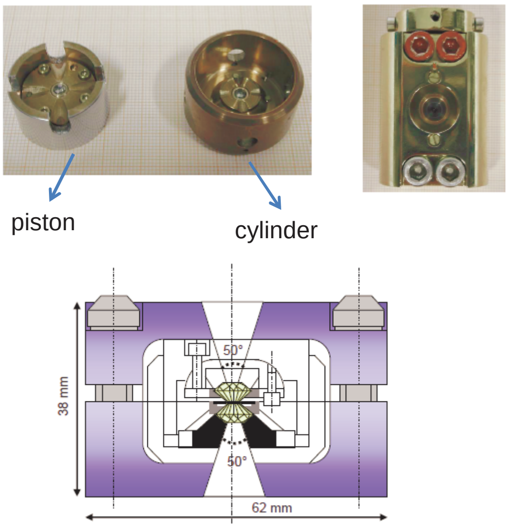

Figure 3.7: The CryoDAC-Mega cell and its cross-sectional view [53].

Figure 3.7 shows a picture for the Diacell CryoDAC-Mega and its cross-sectional view.

Syassen-Holzapfel-type DAC:

The Syassen-Holzapfel type diamond anvil cell [54] is a clamped piston-cylinder cell developed by Huber, Syassen and Holzapfel. Figure 3.8 shows a Syassen-Holzapfel DAC and its cross-sectional view. One of the diamond anvils is mounted in an (X-Y) translational stage incorporated in a fixed backing plate. The other diamond is mounted on a tilting stage in a moving piston. The force for compressing the anvils for pressure generation is produced by a thread-and-knee mechanism. A simple gear-set wrench synchronously turns two threaded rods which connect the front and back sides of the brackets and pulls the lower ends of the brackets together. Thereby, the distance between the upper ends of the brackets decreases compressing the moving piston to generate pressure. The special geometry of this construction results in large force multiplication. Due to the presence of a long piston and good fit combined with thrust acting strictly parallel to the axis of the device, this DAC has excellent alignment stability. The

Syassen-Holzapfel DAC used within this project has a height of 38.7 mm and a length of ≈ 60 mm. The diamond anvils are made of type-IIa diamonds with a height of 1.5 mm and a culet diameter of 400 μm. The maximum pressure that can be generated in this DAC is around 25 GPa. The opening angles of the apertures at the piston and the cylinder assemblies are 40° and 50°, respectively, to minimize signal loss. A gasket made of stainless steel with an initial thickness of 0.25 mm is used in this DAC. Holes with diameters of about 120-150 μm were drilled in the gaskets which were pressed to a thickness about 70-80 μm, for measuring at pressures up to 23 GPa. For measuring the reference in the reflectance measurements, Silver layers are evaporated on the residual pressed area of the gaskets after drilling the holes.

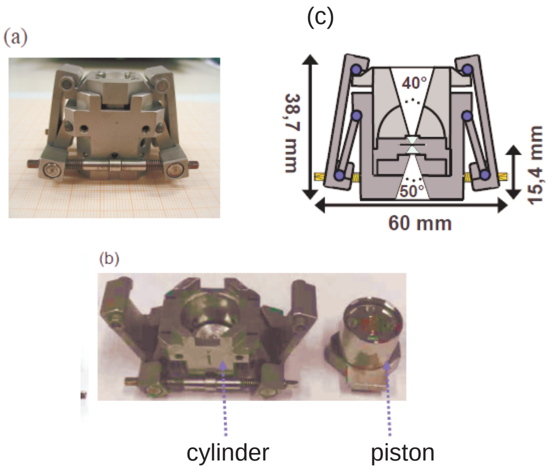

Figure 3.8: The Syassen-Holzapfel DAC and its cross-sectional view [54].

3.3.4 Method for measuring pressure

Several methods for measuring pressure have been developed. The easiest method used in the present work for measuring the pressure is the ruby luminescence technique [55–57], i.e. measuring the luminescence of small ruby balls (AL_2O_3 with Cr^{+3} impurities). In this method, very small ruby balls are placed inside the sample chamber beside the sample. When Cr^{+3} is exposed to a green or a violet laser, the electrons will excite to a higher level followed by rapid non-radiative decay to a metastable level, then it will be relaxed rapidly with a radiative decay to the lowest level (ground state). During the decaying process to the ground state, the R luminescence lines will be emitted. The main luminescence lines in ruby are R_1 and R_2 (transitions of the Cr^{+3} ion) which are characterized by their intensity, sharpness, and both lines are very sensitive to pressure and temperature. Upon increasing pressure, the energy gap between the metastable states and the ground state decreases due to compressing the lattice which leads to shifting of R_1 and R_2 lines appreciably toward the red end of the visible spectrum, i.e. to higher wavelengths (see Figure 3.9).

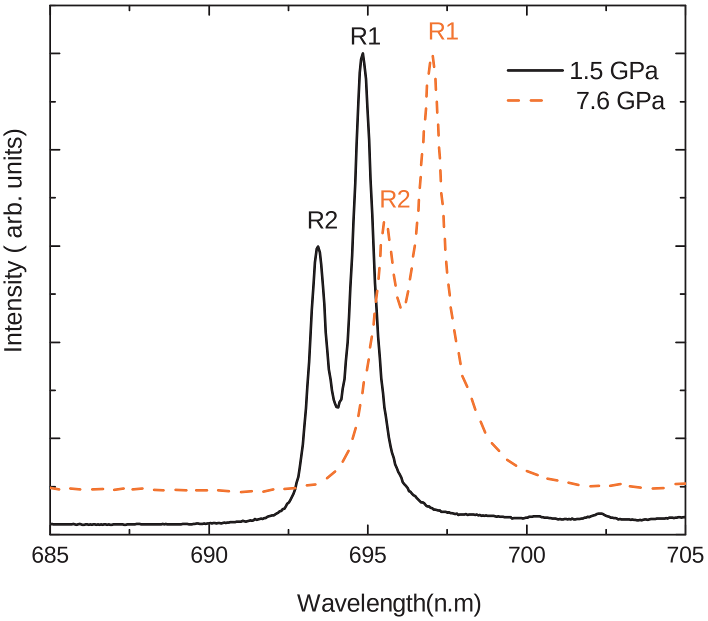

Figure 3.9: The pressure-dependance of R_1 and R_2 wavelengths at room temperature.

The shift in wavelength is followed as a function of pressure. According to Ref. [58] the relationship between the pressure P below 30 GPa and the wavelength shift of R_1 ruby line $\Delta\lambda$(in nm) can be described by

$$P(\Delta\lambda) = \frac{A}{B}[(1 + \frac{\Delta\lambda}{\lambda_0})^B - 1], \tag{3.3}$$

where λ_0 is the wavelength at ambient conditions (λ_0=694.25 nm), A=1904 GPa and B=7.665.

In order to determine the pressure inside the DAC during the measurements, a green laser with sufficient power is passed to the ruby balls inside the DAC, then a measurable luminescence signal from the ruby balls will be obtained. The signal will be collected and sent through an optical fiber to a suitable spectrograph (within this work a high resolution charge Ms260i^{TM} grating-type imaging spectrograph equipped with a CCD camera is used). This way allows us to measure the pressure inside the DAC in-situ without removing the DAC from the microscope stage. Figure 3.10 shows a sketch of the optical head.

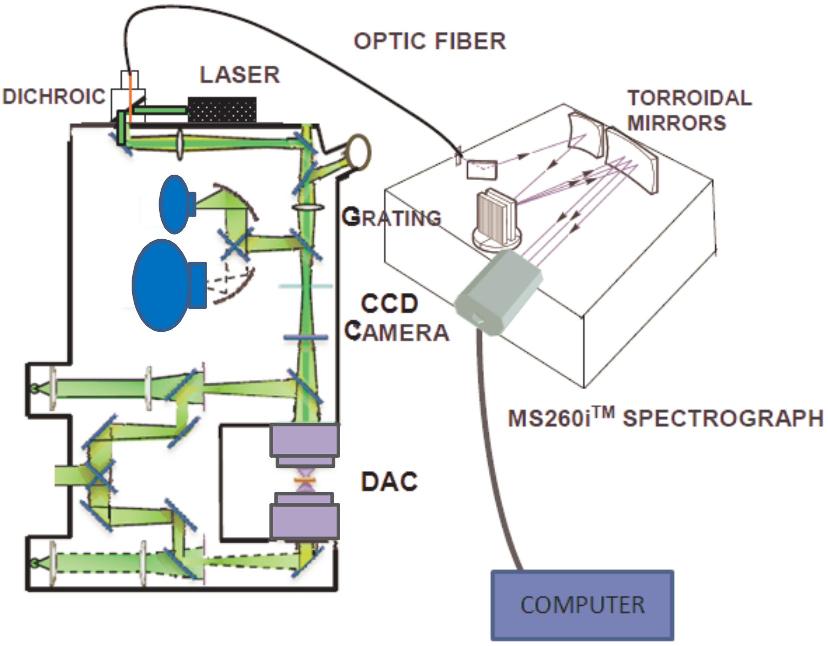

Figure 3.10: Sketch of the ruby luminescence setup coupled to the IR microscope used for pressure calibration [59].

3.4 Experimental equipment for the high-pressure and low-temperature infrared measurements

In this section, there is a short description for the experimental devices used to carry out the reflectance and the transmittance measurements involving the high pressure and low temperature techniques.

3.4.1 Low-temperature and high-pressure infrared setup

The setup used to carry out the temperature-dependent optical measurements under high pressure consists of:

- FTIR (Bruker IFS 66v/s and Vertex 80v) commercial spectrometers, where the basic principle of both spectrometers are the same.
- A home built infrared microscope with 55 mm working distance between the two schwarzschild objectives and magnification of 15x.
- Pressure cell.
- Cryostat.

The reflectance and transmittance measurements under high pressure and low temperature can be achieved by coupling the home built infrared microscope to the FTIR spectrometer. In order to avoid the H_2O and CO_2 absorption features both of them have to be kept under the same vacuum conditions. The diamond anvil cell (DAC) has to be mounted to a suitable home built holder for each DAC, then this DAC holder has to be mounted to the cold finger of an optical cryostat (Cryo Vac KONTI cryostat). The cryostat is used for both reflection and transmission measurements. The detailed description of the cryostat and its accessories is presented in the following.

3.4.2 Cryostat

The cryostat is designed in a way that there is an isolation vacuum which can be pumped. In order to cool the sample, the isolation vacuum must be pumped

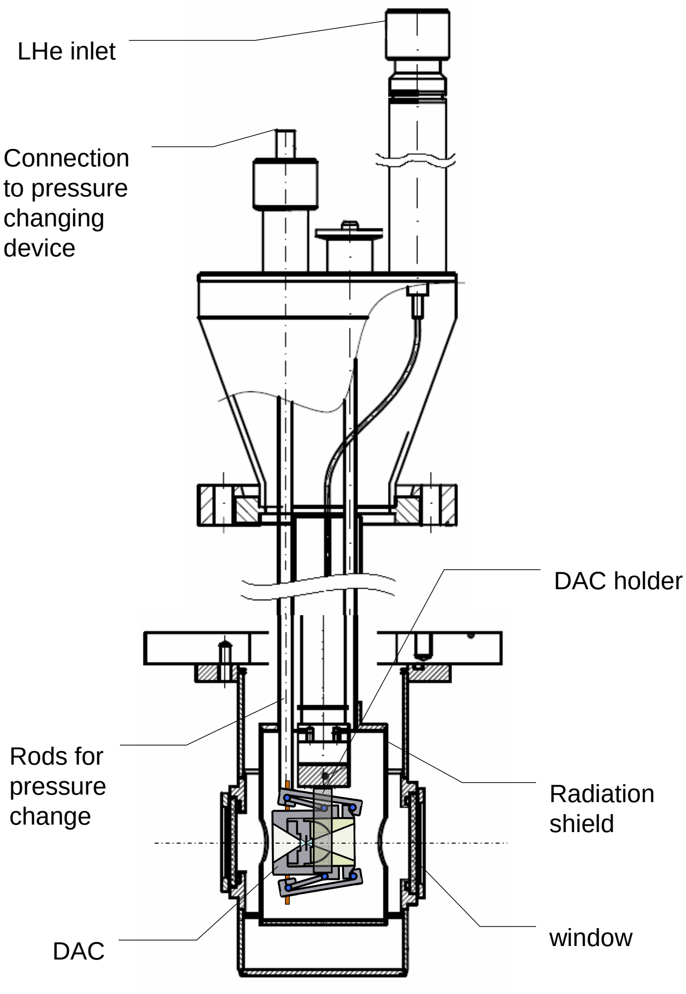

Figure 3.11: Layout of the Cryo Vac KONTI cryostat [60].

to at least $< 10^{-5}$ mbar. The cryostat is a flow-type cryostat with liquid helium supply from an external tank. It can provide a wide operating temperature range from (5- 500 K). The helium flow can be regulated and DAC can be heated through the use of a heat exchanger mounted on the bottom of the experimental chamber, therefore the desired temperature of the sample can be reached. For more details, the liquid helium is fed from the He-container to the heat exchanger through a small stainless steel tube with the help of a vacuum pump. The rate flow of the liquid helium is controlled by a valve. This valve is designed in such a way to allow a precise flow regulation. A heat exchanger is placed close to the sample holder which is controlled by a temperature controller. A suitable vacuum grease is used in order to obtain a good thermal contact (heat exchange) between the DAC and the DAC-holder to avoid the temperature gradient between them during the measurements becoming too large. The basic sketch of the cryostat operation arrangement is shown in Figure 3.11.

3.5 Optical analysis

To investigate the response of a solid to the electromagnetic radiation is one of the more interesting tasks in spectroscopy. When a material is exposed to electromagnetic radiation, its optical responses could be changed. This is measured by sending an electromagnetic wave to the sample surface and measuring the reflected (or transmitted) intensity. In the present work, the optical properties of Fe_3O_4 and TiOCl crystals are studied. Within this section the definitions of the transmission and the reflection will be reviewed and how to determine them inside the DAC is illustrated. Then the models which are used to obtain the corresponding optical conductivity will be presented.

3.5.1 Transmission measurements

3.5.1.1 Transmission measurements on free-standing samples

Practically, transmission (T) is defined as the ratio of the radiation power transmitted through the sample(I_s) to the radiation power of the incident beam through the reference (I_0),

$$T = \frac{I_s}{I_0}, \tag{3.4}$$

While the absorbance is a measure for the fraction of the light which gets absorbed by the sample. From the calculated transmission spectra, the absorbance (A) is obtained according to

$$A = \log(1/T) = -\log T = -\log \frac{I_s}{I_0}, \tag{3.5}$$

3.5.1.2 Transmission measurements in DAC

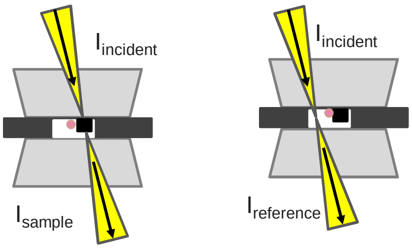

Figure 3.12: Sketch of the measurement arrangement in order to obtain the transmission of a sample in the DAC.

For the transmission measurements inside the DAC, the sample and the ruby ball have to be inserted in one side of the gasket hole in order to leave a free area for the reference measurements (see Figure 3.12). During the measurement, at each pressure, the intensity $I_s(\omega)$ of the radiation transmitted through the sample is measured then the incident radiation spot is focused on an empty space next to the sample to measure the intensity transmitted through the pressure transmitting medium $I_0(\omega)$ as a reference. The calculated transmission of the sample is,

$$T(\omega) = \frac{I_s(\omega)}{I_{reference}(\omega)}, \tag{3.6}$$

3.5.2 Reflectance measurements

3.5.2.1 Reflectance measurements on free-standing samples

In the present work, the IR-reflectance spectra are taken at the near-normal incidence for frequencies 200-20000 cm^{-1}. The calculated spectrum is defined as the ratio of the reflected electromagnetic intensity I_s from the sample surface to the electromagnetic intensity I_0 reflected from the material surface which has a nearly 100% reflecting surface, e.g., Al and Ag,

$$R(\omega) = \frac{I_s(\omega)}{I_0(\omega)}, \tag{3.7}$$

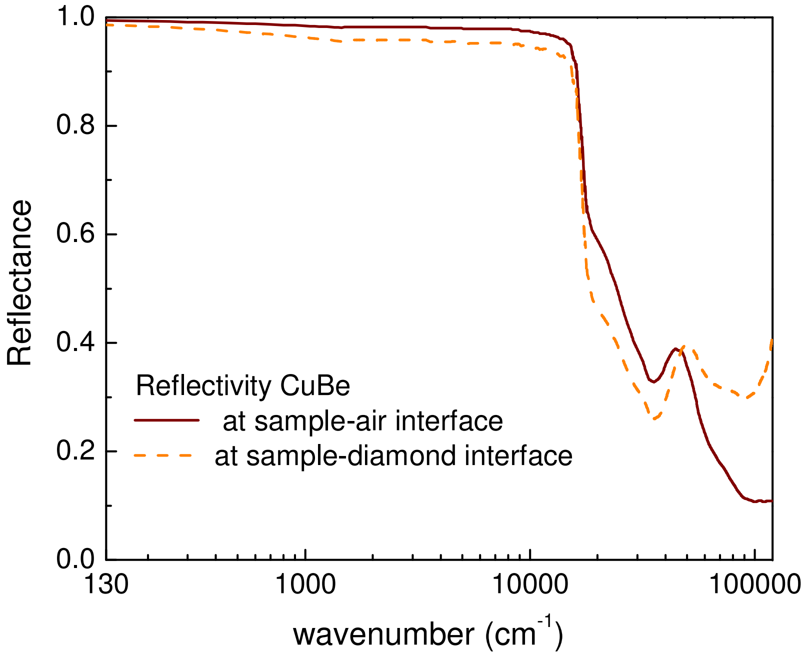

Figure 3.13: Comparison between the infrared reflectance of Cu in air and inside the DAC [61].

3.5.2.2 Reflectance measurements in DAC

In order to obtain the reflectance spectra in DAC, the sample has to lie on the inner face of the diamond. Accordingly, it is not straightforward to find a good reference. As the window size of the cell is too small, it is not possible not place a mirror next to the crystal. Instead, the light reflected back from a clean place from the remaining pre-pressed area of the gasket (hole sides) is used as a reference. A layer of silver is evaporated on it or a gasket from CuBr is used, where Cu has nearly 100% reflectivity in the whole infrared range (see Figure 3.13). The reflectance spectra of the sample with respect to diamond is denoted by (R_{s-d}). It is obtained by measuring the intensity $I_{s-dia}(\omega)$ reflected at the interface between the sample and the diamond anvil for each pressure. For measuring the reference, there are two ways: In the first way, the intensity $I_{gasket}(\omega)$ reflected from the remaining pre-pressed area of the gasket (hole sides) at the same diamond interface of the sample is measured. While in the second way, the intensity reflected from the top surface of the diamond I_1 is measured during the measurement and at the end of the measurement, the intensity reflected from the top surface of the diamond I_2 is measured and the intensity reflected from the top surface of the diamond I_b at the diamond-air interface is also measured as shown in Figure 3.14.

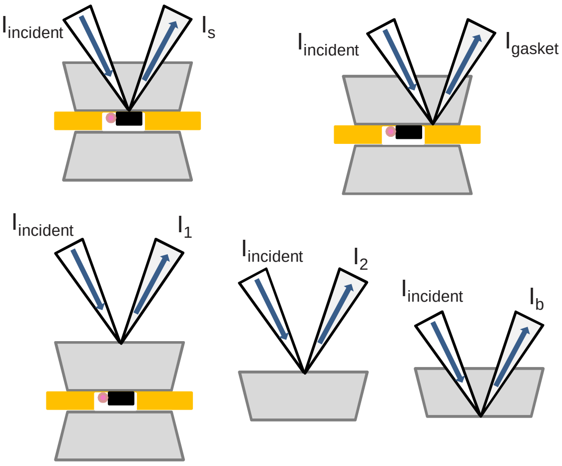

Figure 3.14: Schematic representation of the measurement configuration for obtaining the various quantities required for calculation of the reflectance of a sample at the sample-diamond interface in a DAC.

The absolute reflectance spectrum is calculated according to

$$R_{s-d}(\omega) = \frac{I_{s-dia}(\omega)}{I_{gasket-dia}(\omega)} = [\frac{I_{s-dia}(\omega)}{I_1} \times \frac{I_2}{I_b}]R_{dia}, \tag{3.8}$$

where $R_{dia} = [\frac{n_{dia}-1}{n_{dia}+1}]^2 \approx 0.1667$ for the refractive index $n_{dia} \approx 2.38$.

3.5.3 Optical response and the related Kramers-Kronig transformations

The optical response functions are related to the complex optical conductivity $\tilde{\sigma}(\omega\ )$ and the complex dielectric function $\tilde{\epsilon_r}(\omega)$ of the materials which can be obtained from the measured reflectance or absorbance spectra. Accordingly, to know the full optical response of the material from its reflectance or absorbance spectra, the optical functions n, κ must be known, i.e. the normal refractive index n and the extinction coefficient (κ) which describe the optical absorption. By considering a plane interface between two media with the refractive indices n_1 and n_2, the propagation of the electromagnetic wave can be described via Fresnel equation: Assuming that the interface is between air or vacuum (n_1=1) and a medium with (n_2=$\tilde{n}$), so the reflectance and the transmittance of the material will be described in the following.

- The near normal incident reflectance $R(\omega)$ is given by [62],

  $$R(\omega) = |\frac{n_2 - n_1}{n_2 + n_1}|^2 = |\frac{\tilde{n} - 1}{\tilde{n} + 1}|^2, \tag{3.9}$$

  where $\tilde{n}$ is the complex refractive index which is defined by,

  $$\tilde{n} = n + i\kappa, \tag{3.10}$$

  and the normal refractive index n is defined by

  $$n = \frac{c}{v}, \tag{3.11}$$

  where c and v are the velocity of the light in the free space and in the matter, respectively.

- The transmittance of the material will be described by [59],

  $$T = \frac{[(1-R)^2 + 4R\sin(\phi)^2]e^{-d\alpha}}{(1-Re^{-d\alpha})^2 + 4Re^{-d\alpha}\sin(\beta+\phi)^2}, \tag{3.12}$$

  where d is the thickness of the material, β and ϕ are the transmitted and reflected phase changes, and α is the absorption coefficient. These variables are defined as:

  $$\beta = \frac{2nd\pi}{\lambda_0}, \tag{3.13}$$

$$\phi = \arctan(\frac{-2\kappa}{1-n^2\kappa^2}), \tag{3.14}$$

$$\alpha = \frac{4\pi\kappa}{\lambda_0}, \tag{3.15}$$

where λ_0 is the wavelength in the vacuum.

Now let us return back to equation (3.9) and assume that the interface is between vacuum medium (n_1=1) and a medium with (n_2=$\sqrt{\tilde{\epsilon_r}}$), so the near normal incident reflectivity $R(\omega)$ will be described by:

$$R(\omega) = |\frac{\sqrt{\tilde{\epsilon_r}}-1}{\sqrt{\tilde{\epsilon_r}}+1}|^2, \tag{3.16}$$

where $\tilde{\epsilon_r}$ is the complex dielectric constant which is frequency dependent and is given by:

$$\tilde{\epsilon_r} = \epsilon_1 + i\epsilon_2, \tag{3.17}$$

From Maxwell's equations which describe the propagation of the electromagnetic waves through a matter, the relation between the electric displacement $D(\omega)$ in the matter and the electric field of the electromagnetic wave $E(\omega)$ is given by:

$$D(\omega) = \tilde{\epsilon_r}(\omega) \cdot E(\omega), \tag{3.18}$$

Hence, the complex refractive index of the medium is related to its relative complex dielectric function by

$$\tilde{n} = \sqrt{\tilde{\epsilon_r}}, \tag{3.19}$$

Accordingly, the relationships between the real and imaginary parts of $\tilde{\epsilon}$, $\tilde{n}$, and $\tilde{\epsilon_r}$ will be described by:

$$\epsilon_1 = n^2 - \kappa^2, \tag{3.20}$$

$$\epsilon_2 = 2n\kappa, \tag{3.21}$$

Equations (3.20) and (3.21) show that ϵ_1 and ϵ_2 are dependant on n and κ which are related to the Kramers-Kronig dispersion relations. Furthermore, from the relation between the complex dielectric function and the complex optical conductivity (see Equation (3.22)), the real part of the optical conductivity σ_1 can be calculated depending on the dielectric function

$$\tilde{\epsilon}_r = \epsilon_\infty + i\frac{4\pi\tilde{\sigma}}{\omega}, \tag{3.22}$$

where ϵ_∞ is the valence electrons contribution to the complex dielectric function and is known as high-frequency dielectric constant. $\tilde{\sigma}$ is the complex optical conductivity which is given by,

$$\tilde{\sigma} = \sigma_1 + i\sigma_2, \tag{3.23}$$

Accordingly, one can be deduced the real and the imaginary part of the complex optical conductivity as:

$$\sigma_1 = \frac{\omega}{4\pi}\epsilon_2, \tag{3.24}$$

$$\sigma_2 = \frac{\omega}{4\pi}[\epsilon_\infty - \epsilon_1], \tag{3.25}$$

where σ_1 represents the dissipation of the electromagnetic waves in the medium, and σ_2 performs the screening of the applied field. The relationships which are connecting the real and the imaginary parts of refractive index are known as the Kramers-Kronig relations [62, 63]. Furthermore, by combing the real and imaginary parts of both (the complex optical conductivity and the complex dielectric function) with the Kramers-Kronig relations, a set of the so-called sum rules for several optical parameters is obtained (for more details see Ref. [20, 63])

3.5.4 Drude-Lorentz model

To know more details about the optical properties of the studied materials and compare them with other methods of measurement, the interpretation of the measured reflectance or transmittance spectrum is needed.

Lorentz developed a model which included all direct interband transitions of the material, hence the insulator was treated as an atom with electrons which are bound to the nucleus, i.e., this model describes the localized carriers. The harmonic oscillator within the Lorentz model is given by [20, 63]

$$m\frac{d^2\mathbf{r}}{dt^2} + \frac{m}{\tau}\frac{d\mathbf{r}}{dt} + m\omega_0^2\mathbf{r} = -e\mathbf{E}, \tag{3.26}$$

where m and e are the mass and charge of the electron, respectively. τ is the relaxation time (damping effect), and $\mathbf{r}$ is the electron position vector given by

$$\mathbf{r}(\omega) = \frac{-e\mathbf{E}/m}{(\omega_0^2 - \omega^2) - i\omega/\tau}, \tag{3.27}$$

The relation between the atomic polarizability $\alpha(\omega)$ over all N atoms per unit volume, and the induced dipole moment $\tilde{\mathbf{P}}(\omega)$ is given by

$$\tilde{\mathbf{P}}(\omega) = \frac{Ne^2}{m}\mathbf{E}\frac{1}{(\omega_0^2 - \omega^2) - i\omega/\tau} = N\alpha(\omega)\mathbf{E} = \tilde{\chi}\mathbf{E}, \tag{3.28}$$

where $\tilde{\chi}$ is the dielectric susceptibility. Hence, the dielectric susceptibility is related to the complex dielectric function, accordingly the complex dielectric function depending on the Lorentz model will be given by

$$\tilde{\epsilon}(\omega) = 1 + 4\Pi\tilde{\chi}(\omega) = 1 + \frac{4Ne^2\pi}{m}\frac{1}{(\omega_0^2 - \omega^2) - i\omega/\tau}, \tag{3.29}$$

On the other hand, Drude developed a model which depends on the Lorentz model. He treated the metal as a free electron gas by putting the restoring force equal to zero (i.e., canceling the last term in Equation (3.26)). He assumed the existence of an average relaxation time τ which adjusts the relaxation of the system to equilibrium. From the equation of the electron motion in an electric field, the optical properties of the Drude model can be extracted. The equation of motion of an electron in the Drude model is given by [20, 63]:

$$m\frac{d\mathbf{v}}{dt} + \frac{m\mathbf{v}}{\tau} = -e\mathbf{E}, \tag{3.30}$$

where $\mathbf{v}$ is the electron drift velocity in the direction of the applied field that is corresponding to the average velocity of the electron. In the case of the optical spectroscopy, the drift velocity of the electrons will be expressed by:

$$\mathbf{v} = \frac{e\tau}{m}\frac{1}{1 - i\omega\tau}\mathbf{E}, \tag{3.31}$$

Furthermore, the relation between the current density and drift velocity is described by

$$\mathbf{j} = Ne\mathbf{v} = \frac{Ne^2\tau}{m}\frac{1}{1 - i\omega\tau}\mathbf{E}, \tag{3.32}$$

where N is the electron density, and the DC conductivity σ_0 is equal to

$$\sigma_0 = \frac{\mathbf{j}}{\mathbf{E}} = \frac{Ne^2\tau}{m}, \tag{3.33}$$

From Ohm's law, the conductivity for an isotropic materials is described by:

$$\tilde{\sigma}(\omega) = \frac{\sigma_0}{1 - i\omega\tau}, \tag{3.34}$$

where $\frac{1}{\tau}$ is the scattering rate. From equations (3.32, and 3.34), the real and imaginary parts of the complex conductivity can be written depending on the Drude model as,

$$\tilde{\sigma}(\omega) = \sigma_1(\omega) + i\sigma_2(\omega) = \frac{\tau\omega_p^2}{4\pi}[\frac{1}{1+\omega^2\tau^2} + i\frac{\omega\tau}{1+\omega^2\tau^2}], \tag{3.35}$$

where ω_p is the plasma frequency which is equal to:

$$\omega_p^2 = \frac{4N\pi e^2}{m}, \tag{3.36}$$

From equation (3.22), the frequency dependance of the complex dielectric function and hence its real and imaginary parts is obtained according to,

$$\tilde{\epsilon}(\omega) = \epsilon_1(\omega) + i\epsilon_2(\omega) = 1 - \frac{\omega_p^2}{\omega^2 + i\omega\tau} = (1 - \frac{\omega_p^2}{\omega^2 + \tau^2} + i\frac{\omega_p^2\tau}{\omega^3 + \omega\tau^2}), \quad (3.37)$$

By adding the Equations (3.29 and 3.37), the sum of the complex dielectric function of both the Lorenz and the Drude models can be obtained

$$\tilde{\epsilon}(\omega) = \epsilon_\infty - \frac{\omega_p^2}{\omega^2 + i\tau\omega} + \sum_i \frac{\omega_{p,i}^2}{(\omega_i^2 - \omega^2) - i\omega\tau_i}, \quad (3.38)$$

where the second and the third terms of Equation (3.38) represent the Drude (the intraband transitions) and the Lorentz contributions (the different interband transitions), respectively. $\omega_{p,i}^2$, ω_i and τ_i are the oscillator strength, center frequency, and width of the *ith* Lorentz oscillator, respectively.

Figure 3.15 shows an example of how the typical reflectance and its corresponding optical conductivity spectra for metal and insulator looks like. In the case of metal, the reflectance increases to 100% as the energy tends to zero, while the optical conductivity reaches its dc value. In the case of insulator, the reflectance at low energies reaches a constant value depending on the higher energy absorptions. Hence there are no free electrons presenting in the insulator so there is no Drude term and the optical conductivity tends to zero as energy also approaches zero.

Within this project, the Drude-Lorentz model is used to describe the linear response of the optical conductivity $\sigma_1(\omega)$ properties of Fe_3O_4 and TiOCl (e.g. coherent term, phonon, interband transition, etc.) as sum of several contributions.

3.6 Other experimental techniques

In this section, a brief description of the other experimental techniques used to obtain the results in this thesis will be given.

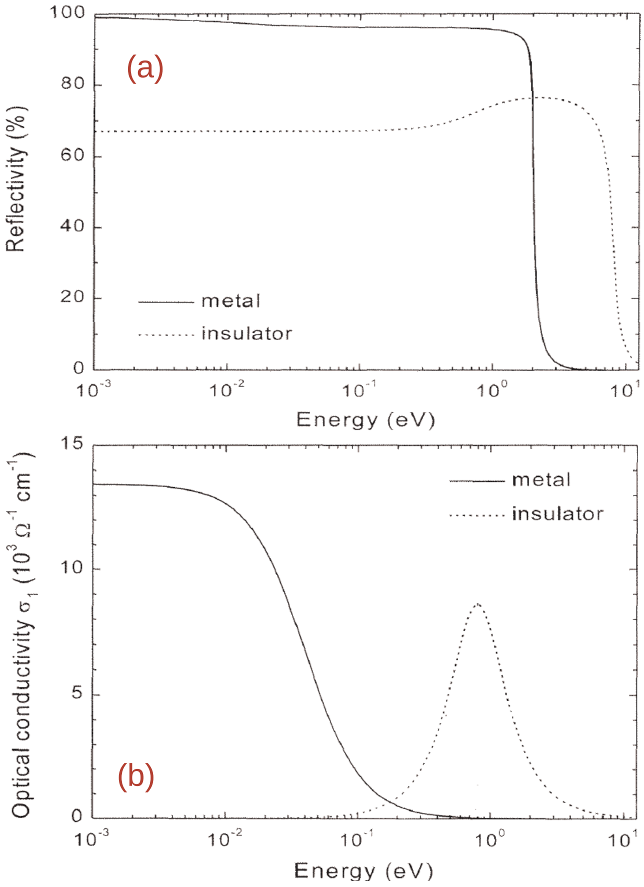

Figure 3.15: (a) The typical reflectivity curves obtained from Ref. [64]. Solid and dot curves represented the metal and the insulator, respectively. (b) The corresponding optical conductivity obtained by the Drude-Lorentz model.

3.6.1 Measurements at the synchrotron facility

Synchrotron radiation is an infrared source of radiation, occurring when electrons are accelerated to very high speeds [65]. This could happen either inside a curved path through a constant magnetic field (bending magnet radiation), or on their trajectories inside a variable magnetic field. The synchrotron radiation energy is proportional to the fourth power of the electrons speed while it is inversely proportional to the square of the radius of the path. For this reason, storage rings devoted to the production of synchrotron radiation, electrons or positrons are used. The basic features of the synchrotron radiation are:

- High intensity, which is 10 times larger than the other standard thermal sources.
- High degree of polarization.

- Pulsed on 100 picoseconds time scale.
- Large bandwidth (from far-IR, visible light, UV, to soft and hard X-ray).

Within this work, the far-IR reflectance measurements of Fe_3O_4 under pressure at room temperature, and under pressure at low temperature, were carried out at the synchrotron radiation facility, Angstroemquelle Karlsruhe beam-line (ANKA) at Karlsruhe, Germany. At the ANKA-IR beamline similar instruments as described above (i.e., an IR microscope coupled to Bruker IFS66v/S), are used to carry out the measurements. A detailed description of the beamline optical scheme and of the performances for infrared spectroscopy is found in Ref. [66, 67]. Here, it must be noticed that before calculating the reflectance spectra, the variation of the spectral intensity of synchrotron radiation induced from the decrease of the electron beam current with time, must be taken into account by applying additional normalization procedures.

Additionally, the high pressure X-ray powder diffraction measurements of TiOCl were performed at the beam-line ID09A in the European Synchrotron Radiation Facility (ESRF), at Grenoble, France, which will be discussed in the following.

3.6.2 X-ray diffraction measurements

X-ray diffraction (XRD) is a standard technique for phase identification of a crystalline material. It gives the diffraction from a collection of thousands of tiny single crystals having random orientation. It provides information on unit cell dimensions. Hence, each crystalline solid has a unique pattern identifying its crystal structure. The XRD technique is based on the incidence of a collimated beam of X-rays (with a wavelength λ, generated by a cathode ray tube) on the sample. When the sample and the detector rotate, the X-rays will be scattered at the crystallographic lattice planes of the sample. Hence, the diffraction peak occurs when the Bragg condition is satisfied [68]:

$$n\lambda = 2d\sin\theta, \tag{3.39}$$

where n is integer, λ is the wavelength of the X-rays, d is the interplanar spacing generating the diffraction (the lattice spacing), and θ is the diffraction angle. This law relates the wavelength of electromagnetic radiation to the diffraction angle and the lattice spacing in a crystalline sample (see Figure 3.16). In order to obtain the diffraction pattern (Debye-Scherrer rings) the diffracted X-rays have to be detected, processed and converted to a count rate which is then output to a device such as a computer monitor [69].

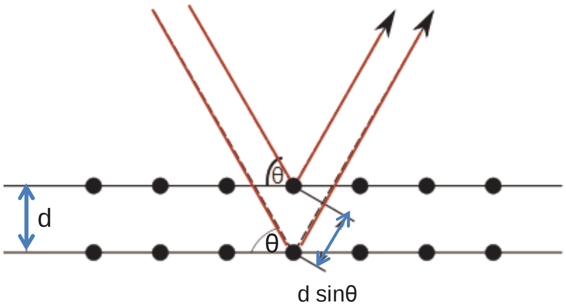

Figure 3.16: Schematic showing the Bragg diffraction.

Within this project, X-ray Powder Diffraction measurements of TiOCl under pressure at room temperature were carried out by C. A. Chuntscher et al. [70]. A monochromatic radiation source with λ=0.4128 $\mathring{A}$ was used. Normally, the powder consists of a large number of randomly oriented micro-crystallites. When it is exposed to monochromatic X-rays, all crystallites in a favorable orientation will diffract the radiation according to the Bragg equation (a detailed description about the measurements procedure is found in Ref. [69]). For TiOCl, the sample was scanned through a range of 2θ angles, and all possible diffraction directions of the lattice were attained due to the random orientation of the powdered material. The DAC was rotated by 3° during the exposure to improve the powder averaging. The diffraction patterns were recorded with an image plate detector. The recorded image plate data were converted to diagrams of intensity versus scattering 2θ by using the computer program FIT2D [71]. In this program the diffraction radiation can be seen as the intersection of Debye-Scherrer rings. Before integration, any artifacts due to the diffraction on the gasket, ruby ball, diamond anvils, etc. must be excluded from the 2D image by masking them.

Then for structural analysis, the crystallographic program JANA 2006 software was used to carry out the LeBail fits of the diffraction data (a detailed description about the use of JANA 2006 for obtaining the LeBail fit, is found in Ref. [72]).

Chapter 4

The physical properties of magnetite

4.1 Introduction

Magnetite (Fe_3O_4) is one of the most known minerals. It is characterized by its black color. It belongs to the strong correlated materials, meaning that electron-electron interactions are not negligible. Magnetite is still attractive to several areas of research due to its unique physical, chemical, and magnetic properties. In this chapter, the pressure-dependent investigations on Fe_3O_4 are presented. A survey on the basic physical properties of magnetite, which we need in order to understand the results in this part of the work, are clarified in the first sections. Then the infrared spectroscopic studies on magnetite under pressure at room temperature and low temperature are presented in the following sections.

4.2 Properties of Fe_3O_4

There are several transition metal oxides which have the general formula AB_2O_4 and crystalize in normal spinel or inverse spinel structure, whereas magnetite is one of the most known example among them. Before we start to speak about the crystal structure of magnetite, let us first understand what is the definition of spinels?

Spinels are any one of the mineral classes which crystallize in the cubic crystal structure and have the general ionic formula AB_2O_4. In general, spinels are divided into two main types: normal spinel and inverse spinel.

- **Normal spinels**: The divalent ions A^{2+} occupy the tetrahedral sites while the trivalent ions B^{3+} occupy the octahedral sites, as described by the ionic formula

$$[A^{2+}][B^{3+}]_2O_4. \tag{4.1}$$

- **Inverse spinels**: The divalent ions A^{2+} swap with half of the trivalent ions, B^{3+}, in the octahedral sites, while the other half of the trivalent ions B^{3+} occupies the tetrahedral sites, as described by the ionic formula

$$[B^{3+}]([A^{2+}][B^{3+}])O_4. \tag{4.2}$$

4.2.1 Crystal structure of Magnetite

Fe_3O_4 has an inverse cubic spinel structure at ambient condition with the following properties: space group O_h^7(Fd$\bar{3}$m), lattice constant a = 8.396 $\mathring{A}$, and Z = 8 [73–75]. The ionic formula for Fe_3O_4 can be written more precisely as

$$[Fe^{3+}]_A[Fe^{2+} + Fe^{3+}]_BO_4. \tag{4.3}$$

where A and B denote the tetrahedral and the octahedral sites, respectively as shown in Figure 4.1[75].

The Bravais lattice of magnetite consists of 14 atoms and is considered as face-centered cubic (fcc) with 8 formula units in the unit cell. Each unit cell of this lattice contains 32 closely packed O^{2-} ions embracing 64 tetrahedral (A-type) and 32 octahedral (B-type) interstices. Normal spinels will be formed in magnetite when 1/8 of the A-types are occupied by 8 divalent (Fe^{2+}) ions and 1/2

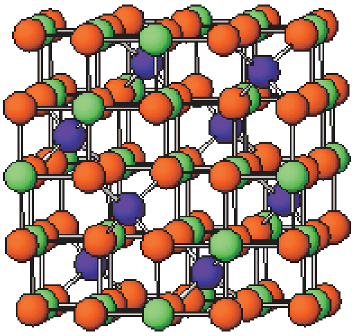

Figure 4.1: Magnetite unit cell: Red atoms are oxygen, blue and green colors represent the iron atoms in the tetrahedral and octahedral sites, respectively [75].

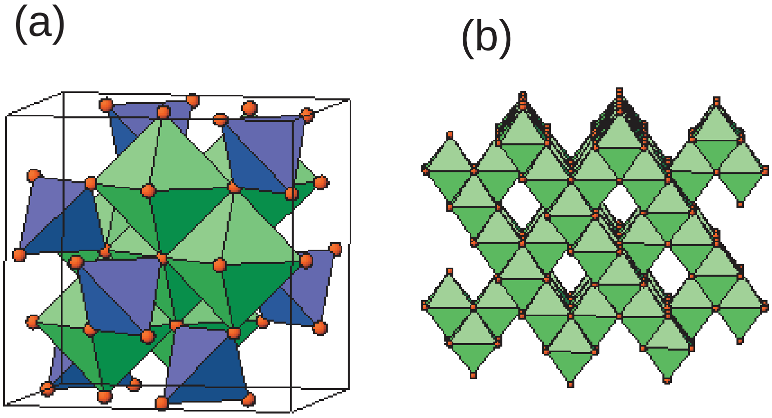

Figure 4.2: (a) Iron polyhedra (blue tetrahedra and green octahedra) in magnetite unit cell. (b) Edge sharing network of octahedra in magnetite [75].

of the B-types are occupied by 16 trivalent (Fe^{3+})ions. Hence, Fe_3O_4 at ambient conditions crystallizes in the inverse spinel structure [76, 77], accordingly 8 of the 16 trivalent ions in the unit cell will be placed in A-sites, while the other 8 of the trivalent ions together with the 8 divalent ions will occupy the B-sites, i.e., magnetite contains both divalent and trivalent iron ions in the octahedral sites at ambient conditions (see Figure 4.2).

Through cooling down from room temperature to low temperature, it was found that magnetite undergoes a first structural phase transition at $T_v \approx 120$ K called Verwey transition, which will be discussed in detail in 4.2.3. At T = T_v; Verwey supposed that the crystal structure of Fe_3O_4 will change from cubic to tetragonal crystal structure [76–78]. Later experiments suggested that the orthorhombic crystal structure is more precise for the low-temperature phase transition than the tetragonal one [79]. Recently, a monoclinic structure with space group (Cc) was proposed as the new crystal structure for magnetite below the Verwey transition [79–82].

On the other hand, an additional phase transition was observed at room temperature under high pressure, where the structure of the high-pressure phase was proposed to be monoclinic [83].

4.2.2 Magnetic order of magnetite

At ambient conditions, magnetite has ferrimagnetic order with a net magnetic moment 4 μ_B per unit formula [84]. For more explanation, let us suppose that we have two sublattices, so the iron ions in the tetrahedral (A-type) and octahedral (B-type) will align ferromagnetically within each sublattice and antiferromagnetically between the two sublattices. Additionally, magnetite undergoes a transition from ferrimagnetic state to paramagnetic state at very high Nèel temperature ($T_N \approx 850$ K) as shown in the inset of Figure 4.2(a).

4.2.3 Verwey transition

The Verwey transition is an electron-ordering transition occurring in a mixed-valent system that results in an ordering of the valence states in the low-temperature phase [76, 85]. In 1939, Verwey discovered during cooling down that the resistivity of magnetite goes weakly up and at a critical temperature $T_v \approx 120$ K a spontaneous jump by a factor of about 100 happened, as shown Figure 4.3(b). At this critical temperature, magnetite undergoes a first-order phase transition called Verwey transition (bad metal-to-insulator transition). Then below the Verwey transition, magnetite becomes much more insulating [76].

The mechanism and origin of this transition is still under discussion until now. In principle, Verwey suggested a purely electronic mechanism for this transition.

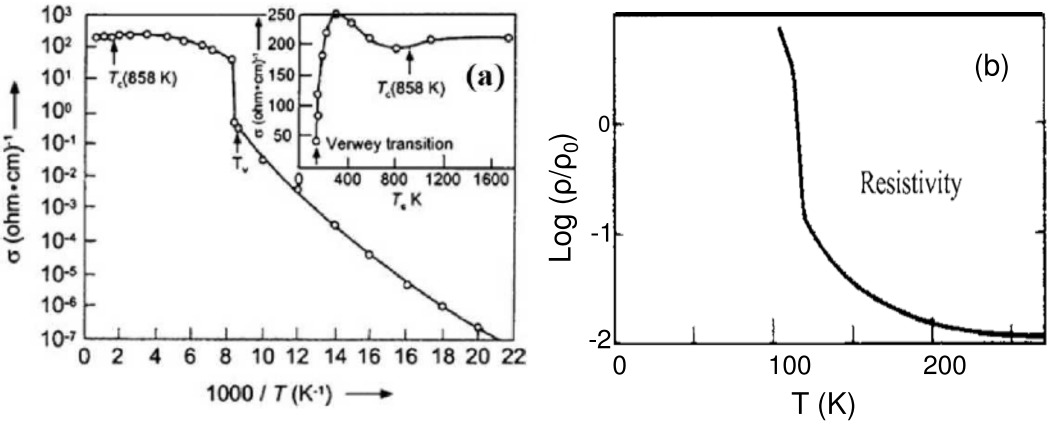

Figure 4.3: (a) The temperature dependance of the electrical conductivity in magnetite. (b) Spontaneous drop of specific resistivity at 120K for magnetite [85].

At ($T>T_v$) he proposed that Fe^{2+} and Fe^{3+} ions are randomly distributed over the B-sites, and there will be a continuous interchange of the electrons between the Fe^{2+} and Fe^{3+} ions in the octahedral sites by means of thermally activated fast electron hopping through the relatively simple valency exchange which is described by:

$$Fe^{2+} - e^{-} \Longleftrightarrow Fe^{3+}$$

Hence, this mechanism is responsible for the metallic state of magnetite. Upon cooling down below the critical temperature T_v, he proposed the occurrence of a charge ordering (CO) at the B-sites leading to a long range order combined with a structural distortion from its cubic symmetry and decreased the conductivity by about two orders of magnitude [80, 86].

Moreover, the x-ray resonant scattering experiments at the Fe K-edge in a single crystal of magnetite [87] found that the origin of the "bad metal-to-insulator" transition at T_v is not only due to the charge ordering on the B-sites but also due to the strong electron-phonon interaction. Furthermore, other experiments, namely: Mössbauer and powder x-ray diffraction, mentioned that magnetite undergoes a coordination crossover (CC) approximately around T_v during cooling down at ambient pressure, where the charge density was claimed to be transferred from the B-sites to the A-sites. As a result the spinel structure will change from inverse to normal according to:

$$[Fe^{3+}]_A[Fe^{2.5+} + Fe^{2.5+}]_B O_4 \rightarrow [Fe^{2+}]_A[Fe^{3+} + Fe^{3+}]_B O_4 \tag{4.4}$$

4.2.4 Vibrational and electronic properties of magnetite

As we mentioned before, magnetite belongs to the space group O_h^7(Fd$\bar{3}$m) at ambient conditions. The predicted number of vibration modes of this structure is 42. According to the group theory, the following modes are expected:

$$\mathrm{A}_{1g}+\mathrm{E}_g+\mathrm{T}_{1g}+3\mathrm{T}_{2g}+2\mathrm{A}_{2u}+2\mathrm{E}_u+4\mathrm{T}_{1u}+2\mathrm{T}_{2u}$$

where the T_{1g}, A_{2u}, E_u, and T_{2u} are silent modes [88, 89]. By applying the selection rules, one expects four infrared active modes ($4\mathrm{T}_{1u}$) and five Raman active modes ($\mathrm{A}_{1g}+\mathrm{E}_g+3\mathrm{T}_{2g}$). Up to now, only two infrared phonon modes at around 355 cm^{-1} and 565 cm^{-1} are observed experimentally [88–91]. In addition, Iizumi et al. [79] suggested that at the Verwey transition the lattice will be distorted. This could be ascribed to the simultaneous condensation of the phonons. This lattice distortion will lead to a decrease of the crystal symmetry, where one can expect a huge increase in the number of the phonon modes at low temperature.

Another important point which needs to be clarified is the electronic structure of magnetite, meaning the distribution of the electrons in the energy levels. The one-electron energy diagram for magnetite at room temperature which was predicted by Ref. [92] is shown in Figure 4.4(a). The main features of this diagram are estimated based on

- The crystal field splitting Δ_{cf}.
- The exchange energy splitting Δ_{ex} between the majority spin-up band and minority spin-down band.

As shown in Figure 4.4(a), the five degenerate d-electron levels of the Fe ions in the octahedral sites will split by the crystal field into three degenerate t$_{2g}$

levels (d_{xy}, d_{xz},d_{yz}) and two degenerate e_g levels (d_{z^2}, $d_{x^2-y^2}$), with a crystal field parameter Δ_{cf}. In solid, the t_{2g} and e_g levels will form the t_{2g} and e_g bands. The majority spin-up of the t_{2g} and e_g bands will be occupied with ten electrons form $Fe^{2+}(3d^6)$ and $Fe^{3+}(3d^5)$ ions, while the extra electron of the Fe^{2+} ion, i.e., the eleventh electron in the octahedral sites occupies the minority spin-down of the t_{2g} band. Therefore, they predicted that the band which appeared at the Fermi level E_f (see Figure 4.4(a)) is developed from the extra electron of the Fe^{2+} ion which occupies the minority spin-down of the t_{2g} band, where the electronic density of state at E_f will be spin-polarized and the conductivity at temperatures above T_v is ascribed to the hopping of this extra electron between the octahedral sites. On contrary, below the Verwey transition temperature, one expects a gap to be open at E_f due to the charge ordering in the magnetite band structure as shown in Figure 4.4(b).

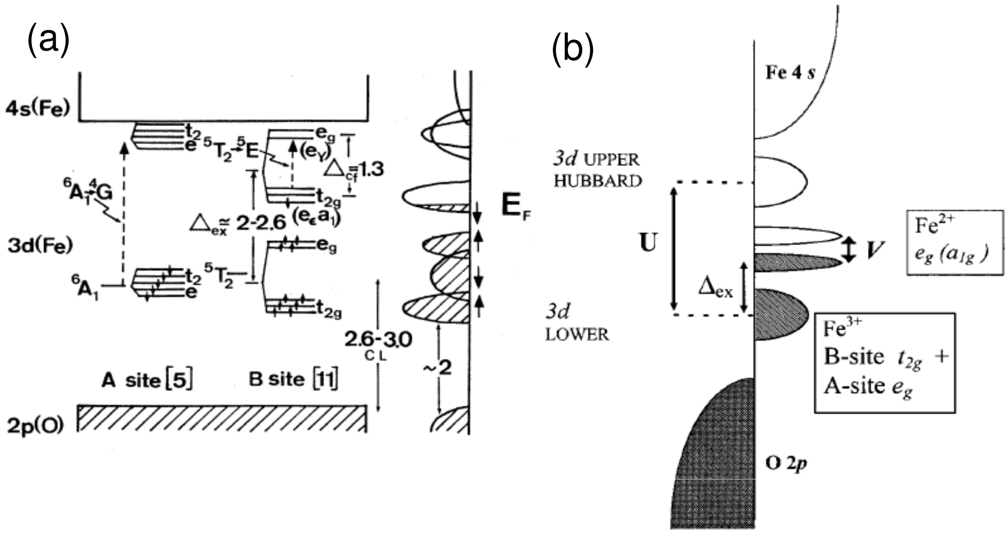

Figure 4.4: (a) The one-electron energy diagram for magnetite at room temperature proposed by [92]. (b) Energy level scheme for magnetite at ambient pressure for $T<T_v$ proposed by [93] where Δ_{ex} is the exchange splitting between spin-up and spin-down orbitals on the same cation. Shaded bands are occupied states.

4.3 Overview of the pressure and spectroscopy studies on magnetite

4.3.1 Pressure effects on magnetite at room temperature

Different studies have been done in order to check the pressure effect on magnetite at room temperature. They are mainly divided into two points of view. The first point of view was supported by different studies as an example Mössbauer and thermoelectric power. The Mössbauer study on magnetite under high pressure and at room temperature [94] did not observe any evidence for a magnetic or crystalline structural change up to 18 GPa and they only noted a discontinuous decrease of the oxygen internal coordinate (u) at around 7.0 GPa. Later this finding was supported by the thermoelectric power studies [95] under pressure at room temperature. They observed a smooth bend (crossover) in magnetite at around (6±1 GPa) which was attributed to the pressure that drove magnetite from the “dominant” inverse spinel to an “ideal” one. Depending on those studies on magnetite, a charge rearrangement is proposed without any evidence of changes in the symmetry of the crystal structure or the structural units with increasing the pressure.

Within the second point of view, according to Equation (4.4), a coordinate crossover (CC) scenario was proposed by the Mössbauer spectroscopy [96], where the existence of a coordinate crossover temperature (T_{cc}) was assumed. This T_{cc} is expected to increase with increasing temperature and reaches room temperature above 7 GPa, while the Verwey transition temperature is expected to decrease with increasing pressure as shown in Figure 4.5. Furthermore, at ambient pressure, the spinel structure changes from inverse to normal spinel during cooling down at around T_v.

The previous finding guides us to check the pressure effects on the electronic and vibrational properties of magnetite at this critical pressure around 6 GPa by using infrared spectroscopy. This issue will be clarified in section 4.6 where our reflectance measurements on magnetite under pressure at ambient temperature will be presented.

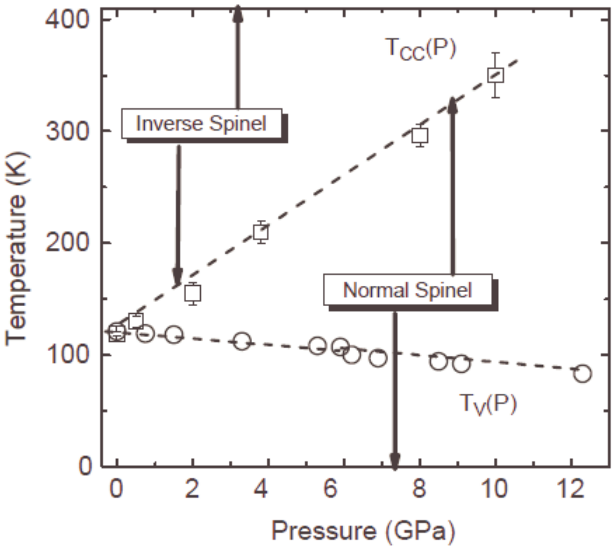

Figure 4.5: The pressure dependance of T_v and of T_{CC} where the T_{CC}(P) curve provides a separation of the normal and inverse-spinal phases, while the T_v(P) curve provides the metal-insulator phases [96].

4.3.2 High-pressure effect of the Verwey transition temperature on magnetite

The changes on the Verwey transition temperature under pressure for Fe_3O_4 have been studied via most of the experimental techniques used in solid state research for instance: electrical transport, thermopower (TEP), XRD, Mössbauer spectroscopy, Raman spectroscopy, magnetic permeability, and neutron powder diffraction. Unfortunately, until now there is a big contradiction among these studies, where the researches are mainly divided into two different opinions. The first opinion claimed that the Verwey transition temperature decreases linearly with increasing pressure up to 6 GPa but with different slope categories (dT_v/dP) depending on the experimental techniques. This opinion was confirmed first by the electrical resistivity and thermopower measurements with $dT_v/dP\approx$ -4.2 K/GPa [97, 98], then later by Raman studies under pressure up to 22 GPa [99] with $dT_v/dP\approx$-5.16±1.19 K/GPa. Additionally, the electric conductivity measurements [100] and magnetic permeability [101] also verified the linear decrease of T_v with increasing pressure with $dT_v/dP\approx$-2.7 K/GPa, while the relative

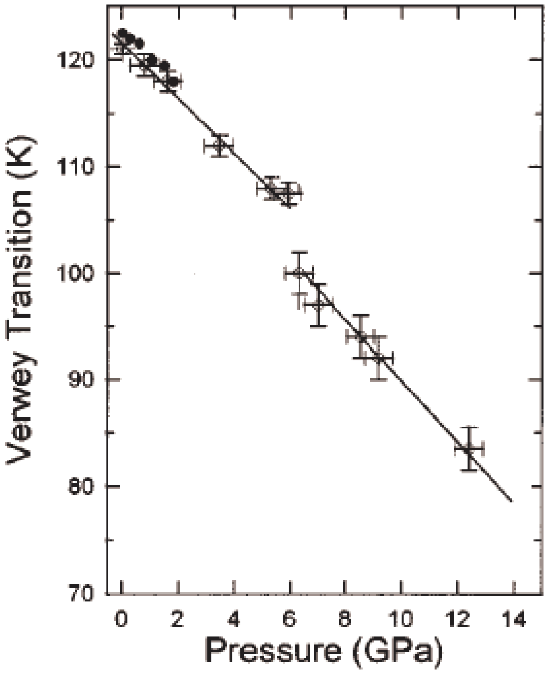

Figure 4.6: Pressure variation of T$_v$ and the proposed P-T phase diagram. The filled circle is corresponding to the data of [100], while the empty circle is corresponding to the data of [93].

conductivity measurements obtained by Rozenberg [93] observed a discontinuous change in the linear pressure coefficient dT_v/dP above 6 GPa from -2.5 K/GPa to -2.9 K/GPa as shown in Figure 4.6.

In contrast to the previous opinion, the electrical resistivity measurements on magnetite from room temperature down to 3 K under pressure up to 10 GPa [102, 103] observed a nonlinear decrease of the Verwey transition temperature with increasing pressure and it disappears at a critical pressure P_c ($\approx$ 8 GPa) which was attributed to the appearance of a metallic ground state of magnetite above P_c. Later x-ray powder diffraction measurements on magnetite under pressure up to 12 GPa and a temperature range from 80 to 150 K [104] claimed also that, outside the observed range of the nonlinear decrease of T$_v$ with pressure (obtained from Ref. [103]), magnetite remains in its metallic nature at all temperatures up to 25 GPa (see Figure 4.7(a)). This finding was then supported by the ac magnetic-susceptibility measurements [105] as they proposed the existence of a quantum critical point at a critical pressure $P_c \approx 8$ GPa. Figure 4.7(b) shows the pressure dependance of the T$_v$ obtained from Ref. [103] combined with the data from Ref. [105].

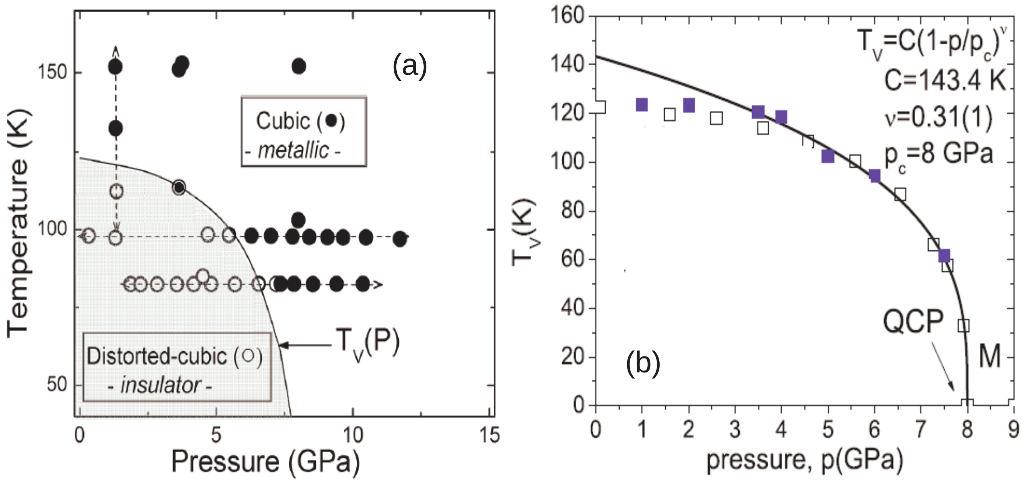

Figure 4.7: The proposed P-T phase diagram of magnetite. (a)Refers to the data from Ref. [104].(b) Refers to the data from Ref. [103]combined with the data from Ref. [105].

The previous discrepancy of clarifying the pressure effect on the Verwey transition temperature of Fe_3O_4 and hence the corresponding pressure-temperature phase diagram motivated us to study the pressure dependance of the Verwey transition in magnetite by reflectance measurements in the far-infrared frequencies range, in order to try to distinguish the phases of magnetite around the Verwey transition from its electronic and vibrational properties in the mentioned frequencies range. Moreover, the pressure-temperature phase diagram depending on our data combined with the previous studies, is proposed. This part of the project will be illustrated in detail in section 4.8.

4.3.3 Spectroscopy studies on magnetite

An additional information on the characterizations of the Verwey transition was also realized from the investigations of the optical properties of magnetite, as several studies were carried out, in order to analyze the optical absorption and reflection spectra besides the infrared phonon spectra of magnetite. Earlier infrared studies of magnetite [106] observed an increase in the infrared reflectivity spectra towards lower photon energies at room temperature. This increase was attributed to the intraband transitions of the conduction electrons. While during

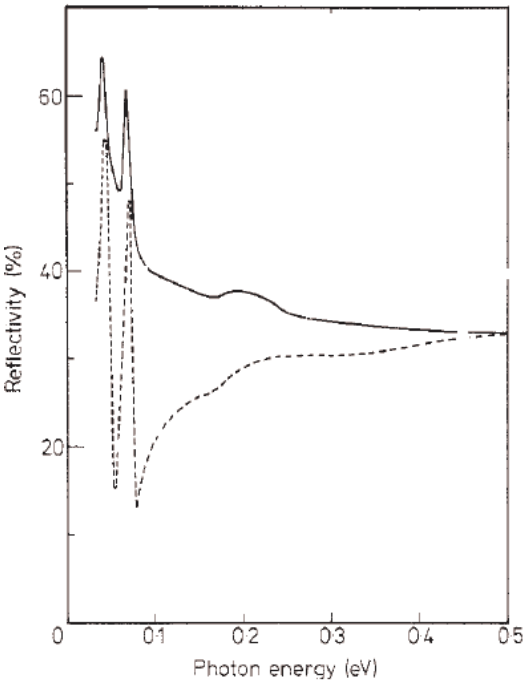

Figure 4.8: Reflectivity of magnetite at 300 K (full curve) and 20 K (broken curve) obtained from Ref. [106].

cooling down through the Verwey transition temperature, the overall reflection spectrum decreases due to the decrease of the conduction electrons contributions (see Figure 4.8). Additionally, two sharp peaks around 350 and 560 cm^{-1} and a broad maximum around 1614 cm^{-1} were observed. The two peaks are claimed to be infrared-active phonon modes.

Later, Raman and IR spectroscopy studies [88, 89] showed significant changes in the phonon modes below the Verwey transition, where new phonon features appear due to the changes in the crystal symmetry and structure below T$_v$. Furthermore, the optical conductivity data [89, 91] displayed a broad mid-infrared temperature-dependant band at around 5000 cm^{-1} (see Figure 4.9). Its origin was claimed to be due to the transition between the Fe^{+3} and Fe^{+2} in the octahedral sites confirming the polaronic nature of this band. Hence, above the Verwey transition some carriers are delocalized, leading to broadening of the band and increase of the low-frequency part of the optical conductivity due to the transfer of the oscillator strength from this band. Then during cooling down through the Verwey transition a charge gap of about 0.14 eV is observed to be opened at T$_v$, where the carriers are assumed to be localized polarons.

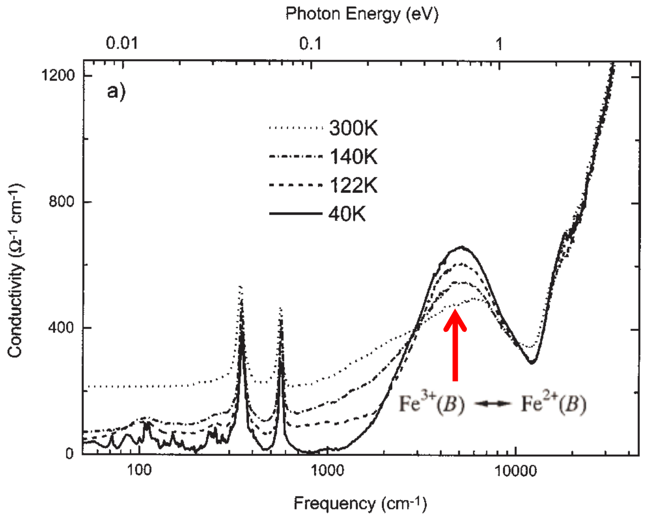

Figure 4.9: The optical conductivity of magnetite calculated by the Kramers-Kronig transformation of the reflectance data obtained from [89].

Up to now the pressure effects on the mid-infrared band (polaronic band) of magnetite at room temperature are still an open issue which will be illustrated in the coming section.

4.4 The electric transport measurements on magnetite at low-temperature

In order to check the Verwey transition temperature of the single crystals of magnetite and hence their quality before starting the pressure-dependant reflectance measurements, the temperature dependant electrical transport measurements on magnetite at ambient pressure are carried out. The single crystals of magnetite used in this work were obtained from the group of Prof. Brabers. The sample crystals were prepared from α-Fe_3O_4 using a floating-zone method with radiation heating [107]. The standard four-probe technique was used to carry out the electric resistivity data. The sample was mounted on a Copper sample holder by using a suitable low temperature glue. Before that the sample holder has to covered by an insulator film in order to isolate the sample from the conducting Copper holder. Two platinum wires are connected to the sample sides by sil-

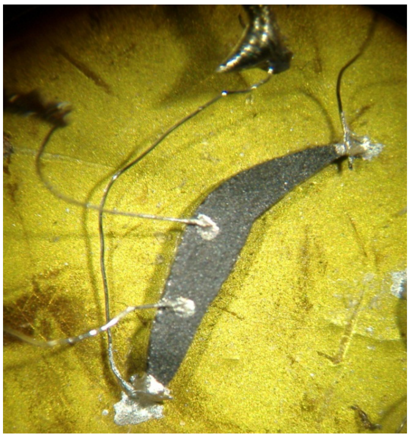

Figure 4.10: The sample mounted on the sample holder.

ver paste for measuring the current passing through the sample during cooling down. The voltage drop across the sample was measured via another two platinum wires connected to the contacts region on the sample surface by Silver paste (see Figure 4.10).

At ambient condition the value of the electrical resistivity (ρ) was found consistent with the value which was recorded from the previous reports, while upon cooling down the electrical resistivity exhibits an abrupt increase with about 100 times at around (T_v $\approx$122 K) which is a typical sign for the Verwey transition (see Figure 4.11). Furthermore, during cooling down and warming up a hysteresis loop was observed which is a signature for the first order nature of the Verwey transition [76, 85].

4.5 Free-standing reflectance measurements of magnetite at ambient conditions

The reflectance spectra at ambient condition “free standing measurements” in the frequency range (200-18000 cm^{-1}) are carried out, in order to compare the electronic and vibrational properties of magnetite with the earlier studies. The measurement procedure is discussed in details in the experimental chapter. The

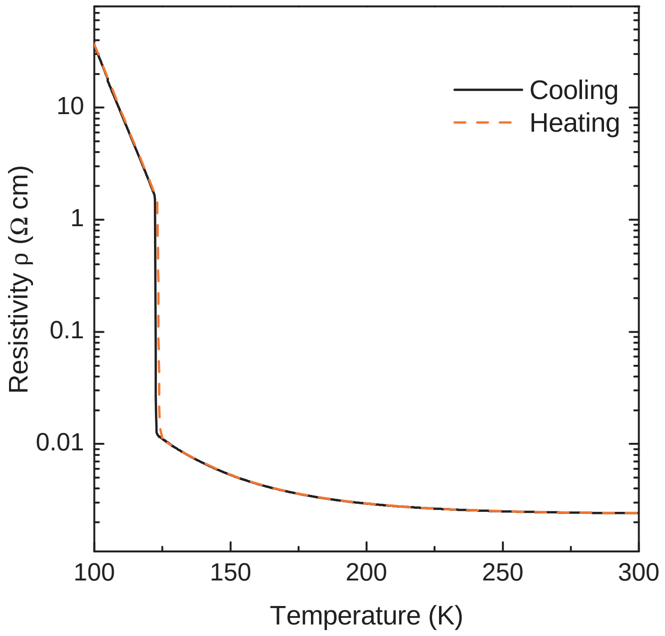

Figure 4.11: Electrical resistivity as a function of temperature at ambient pressure.

resulting reflectance spectrum is shown in Figure 4.12(a). The overall reflectance spectrum showed a similar behavior to that observed in the earlier reports [89, 91]. Then, in order to obtain the corresponding real part of the optical conductivity spectrum from the reflectance spectra via Kramers-Kronig (KK) transformation and thereby its electronic and vibrational properties, the reflectance spectrum was extend by merging our data with the data from Ref. [91]. To extrapolate the high-frequency part (above 18000 cm^{-1}), the Drude-Lorentz fit is used to extrapolate the low frequency part (below 200 cm^{-1}) and fit the overall reflectance spectrum. From the fitting of the reflectance spectrum, the simulated reflectance spectrum was obtained with taking into account the sample diamond interface (see the dashed red spectrum in Figure 4.12(a)). Then for describing the different excitations in the optical conductivity spectrum, the obtained optical conductivity spectrum was fitted by using the Drude-Lorentz model. Two oxygen phonon modes T_{1u} were observed at around 355 cm^{-1} and 565 cm^{-1}. The latter mode is related to the stretching of the A-O bond, while the first mode is due to the

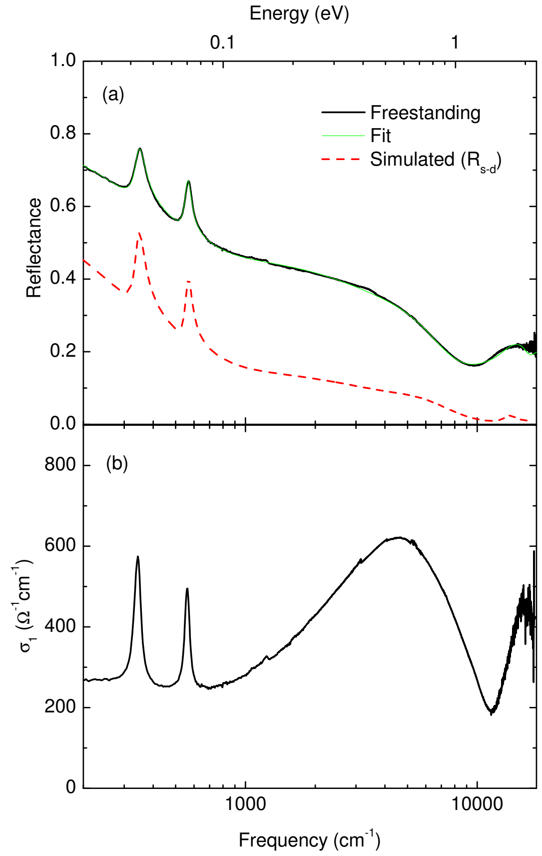

Figure 4.12: (a) The reflectance spectrum of the free-standing sample and its simulated reflectance spectrum at the sample-diamond interface. (b) The real part of the optical conductivity obtained via Kramers-Kronig analysis.

motion of the oxygen perpendicular to this bond [90]. Besides, a pronounced mid-infrared band with a maximum at around 5000 cm^{-1}, which is a typical signature of polaronic charge carriers between the Fe^{2+} and Fe^{3+} ions on the octahedral sites [108], is observed. These observations are in a good agreement with the earlier optical results noticed by different groups [88, 89, 91]. Furthermore, the electrical conductivity value obtained form our dc data is close to the extrapolated value of our optical conductivity at zero frequency.

4.6 Infrared reflectance measurements of magnetite under high-pressure

Within this section, our study of the optical properties of magnetite under high pressure at room temperature is presented. The pressure-dependent reflectance measurements up to 8 GPa at room temperature are reported here. Thereby, its corresponding optical conductivity is studied, in order to check the proposed crossover in magnetite near 6 GPa. Furthermore, theoretical models of small polaron and large polaron are used for fitting our optical conductivity data, in order to verify the polaronic transport in magnetite in the infrared frequency range.

4.6.1 Experiment for the high-pressure reflectance measurements at room temperature

In this part of the work, the pressure dependent reflectance for magnetite at room temperature was studied for the whole infrared and visible frequency range [200-18000 cm^{-1}]. The CryoDAC Mega cell type diamond anvil cell was used for pressure generation up to 8 GPa. The measurements were carried out on small pieces of Fe_3O_4 (about 140 μm×140 μm) cut from a single crystal with thickness of $\approx$ 50 μm. Then the sample was loaded into a hole drilled in a CuBe gasket. Finely ground CsI was chosen as quasi-hydrostatic pressure medium. The measurements were carried out using an infrared microscope coupled to a Bruker IFS 66 v/S Fourier transform infrared spectrometer(FT-IR). All reflectance spectra, which refer to the absolute reflectance at the sample-diamond interface, are denoted as R_{s-d}. In order to improve the signal-to-noise ratio, the far-infrared part of the measurements was carried out at the infrared beamline of the synchrotron radiation source ANKA in Karlsruhe, where the same equipment was installed. In order to ensure consistency and reproducibility of the sample, the measurements were carried out twice for each frequency range. All details about the measurement procedure: The normalization method and how the data was analyzed, are explained in the experimental chapter.

4.6.2 Results and discussion

The pressure-dependant reflectance spectra of magnetite in the infrared and visible frequency ranges under pressure up to 8 GPa at room temperature are shown in Figure 4.13(a). The reflectance data around 2000 cm^{-1} are dominated by the strong phonon absorption of the diamond anvils (explained in detail in the experimental chapter), and thereby they are not shown. With increasing pressure, the reflectance in the frequency part below 5000 cm^{-1} increases monotonically indicating a growth of the spectral weight in the infrared response. Furthermore, for the frequency part above 12000 cm^{-1}, no pressure dependance in the reflectance spectra was observed. Additionally, the two oxygen phonon modes T$_{1u}$ are observed. They have been also observed in the free standing measurements. In order to know the different optical excitations of the sample, it is needed to calculate the real part of the optical conductivity via the Kramers-Kronig transformation. By following the same way for extrapolating the reflectance data, as explained at ambient condition, the real part of the optical conductivity (σ_1) was obtained. Here, it is necessary to mention that the sample diamond interface was taken into account for fitting the reflectance spectrum, the multiphonon diamond absorption area (1800-2760 cm^{-1}) was extrapolated via the Drude-Lorentz fit, and the reflectance data were supposed to be pressure-independent above 18000 cm^{-1}. An example for the fitting of the reflectance at around 1.5 GPa is shown in Figure 4.13(b).

Figure 4.14 shows the obtained real part of the optical conductivity $\sigma_1(\omega)$. The overall optical conductivity spectrum below 5000 cm^{-1} increased with increasing pressure which is attributed to the presence of the Drude-type contribution indicating a metallic-like nature of magnetite. Furthermore, the observed two phonon modes show a blue shift with increasing pressure as shown in the inset of Figure 4.14. This shift of the phonons to higher frequencies is in agreement with the general expression for the vibrational frequency of a phonon [109] given by

$$\omega_0 = \sqrt{\frac{f}{\mu}}, \tag{4.5}$$

where f is the force constant and μ is the reduced mass of the ions involved in

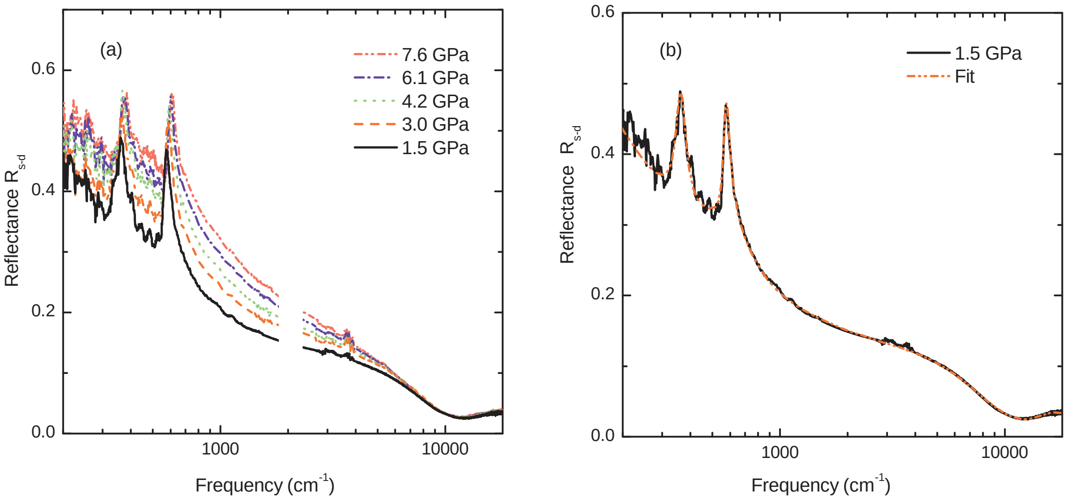

Figure 4.13: (a) Pressure-dependent reflectance spectra of magnetite at RT. (b) Fit of the RT reflectance spectrum at around 1.5 GPa using the Drude-Lorantiz model.

the vibration. According to Eqn. 4.5 increasing the applied pressure leads to increasing the force constant in most cases, i.e., stiffening the lattice and hence shifting the frequency to higher frequencies. For all pressures, the pronounced mid-infrared absorption band which was seen at ambient conditions was observed. This polaronic band showed a pressure-dependant behavior.

In order to specify the changes for each contribution in the optical conductivity spectrum (Drude term, two phonon modes, MIR-band,...etc.) as a function of pressure, the real part of the optical conductivity is fitted by using a Drude-Lorantz model simultaneously with the reflectance spectrum. The fit of the optical conductivity together with the fitting components of magnetite at 1.5 and 7.6 GPa, as examples, are shown in the left panels of Figure 4.15, respectively. For the fitting, it was supposed that the value of ϵ_∞ is pressure independent and fixed it to the value (ϵ_∞ =1) for all the pressures. Moreover, beside the Drude term and the two Lorentzian functions which are used for describing the two T_{1u} oxygen phonon modes, additional two Lorentzian functions were used for describing the MIR-band. Interestingly, in order to obtain a good fit, an additional far-infrared band at around 600 cm^{-1} has to be added to the optical conductivity contri-

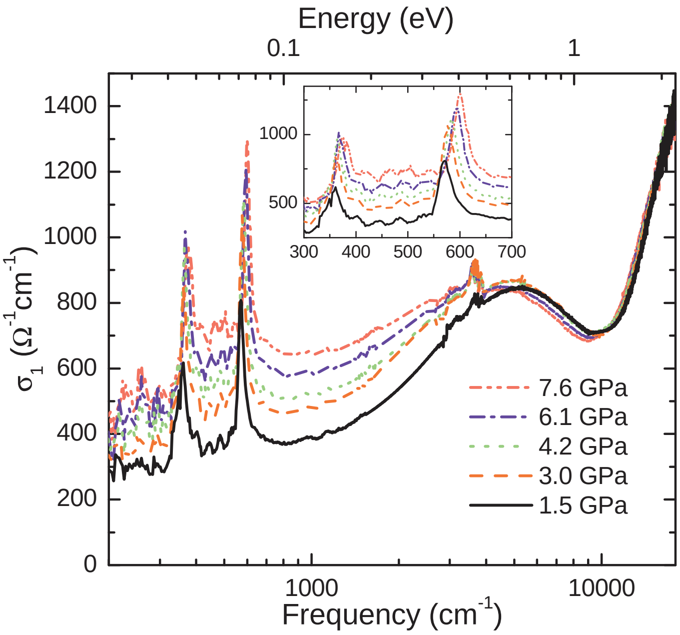

Figure 4.14: Pressure-dependant real part of the optical conductivity spectra of magnetite obtained from the fit of the reflectance spectra using Drude-Lorentz model. The inset shows the phonon modes in linear scale.

butions under pressure and described by one Lorentzian oscillator. It is worth mentioning here that without this far-infrared band, we are not be able to fit the optical conductivity data well (see the right panels of Figure 4.15).

In general, with increasing the pressure, one expects a compression of the lattice which causes an increase in bandwidth and stiffening of the crystal lattice, which in turn results in decrease in the electron-phonon coupling. Below there is a discussion of the observed changes on magnetite sample as a result of the change in the electron-phonon coupling in the crystal lattice with increasing pressure.

The changes in the optical conductivity contributions induced by pressure

By extracting the various contributions (Drude peak, phonon modes, MIR band,...etc) from the fitting of the optical conductivity at each pressure, the following was observed:

- The obtained values for the plasma frequency ω_p and the optical conductivity at zero frequency σ_{dc} from the Drude term increased with increasing

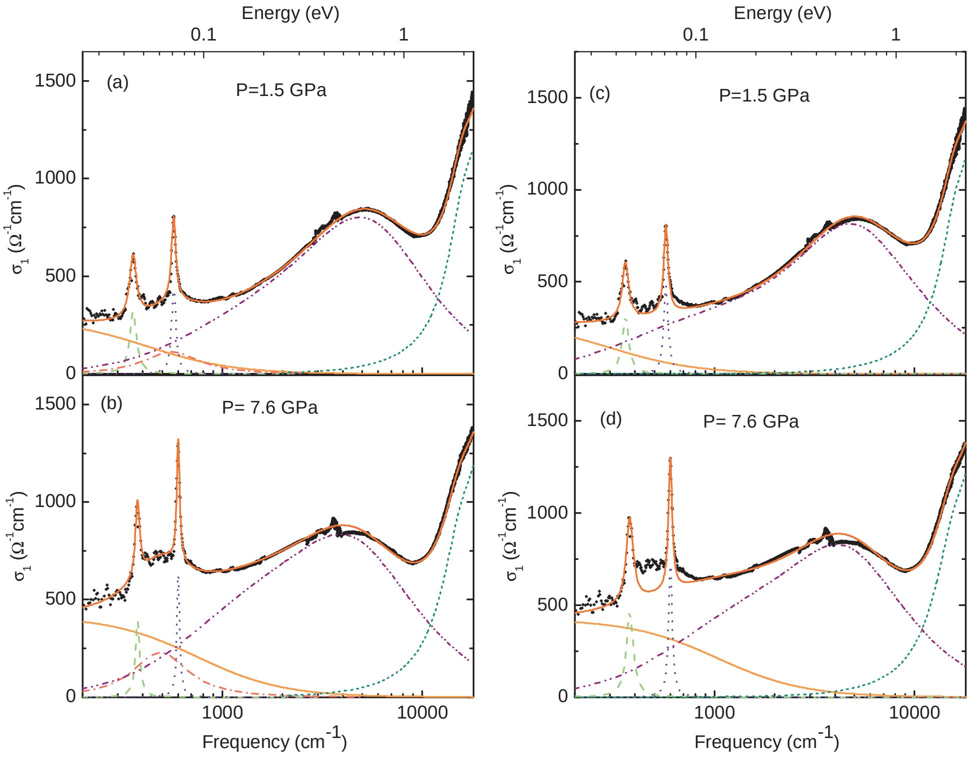

Figure 4.15: The left panels show the RT optical conductivity spectra of magnetite at (a) 1.5 GPa and (b) 7.6 GPa together with the fit components obtained from the fit using Drude-Lorentz model. The right panels show an example of the fitting of the RT optical conductivity spectra of magnetite at (c) 1.5 GPa and (d) 7.6 GPa together with the fit components obtained from the fit using Drude-Lorentz model without taking into accounts the existence of the far-infrared band.

pressure, while above 6 GPa both values seemed to be hardly shifted with increasing pressure (see Figure 4.16).

- The stiffening of the lattice with increasing pressure appears in the hardening of the two T_{1u} oxygen phonon modes (the two phonons shifted linearly to higher frequencies with increasing pressure, while above 6 GPa they seem to be enhanced as shown in Figure 4.17). In order to clarify this observation, the peak positions of the two phonon modes were fitted up to 8 GPa using the function:

$$\omega(P) = A + B \times P$$

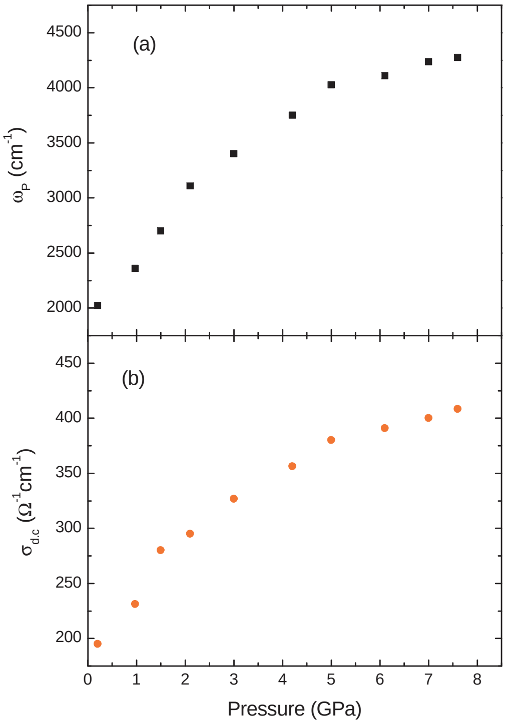

Figure 4.16: Pressure dependance of (a) plasma frequency ω_p and (b) dc conductivity σ_{dc} of the optical conductivity of magnetite obtained from the fit using the Drude-Lorentz model.

where P is the applied pressure and B is the corresponding linear pressure coefficient. The value of B obtained from the fitting of the high-frequency phonon position is $B = 4.9$ cm^{-1}/GPa up to 8 GPa. For the low-frequency phonon, up to 6 GPa, it is found $B = 1.9$ cm^{-1}/GPa followed by a sudden change in the phonon position, indicating a change in the corresponding linear pressure coefficient to $B = 4.9$ cm^{-1}/GPa, which could be due to pressure-induced hardening of the crystal lattice. Furthermore, the linewidths of the two phonon modes decreased with increasing pressure and it seems that both of them tend to saturate above 4 GPa (see Figure 4.17).

- The mid-infrared absorption band slightly narrows and continuously shifts towards low frequency with increasing pressure (see Figure 4.18(a)). This finding confirms the polaronic nature of the band: The frequency position of the polaronic band is a measure of the polaron binding energy and thus the electron-phonon coupling. As it was mentioned before, the electron-phonon coupling tends to decrease with increasing the applied pressure, accordingly

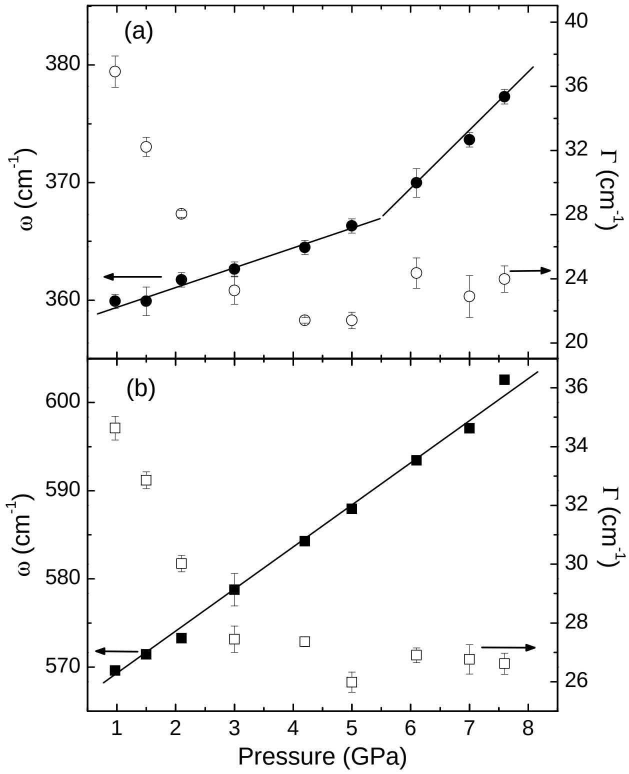

Figure 4.17: The position of the phonon modes and linewidths as a function of pressure obtained by Drude-Lorentz fitting of the optical conductivity spectra. The lines indicated the linear fits of the data point, in order to obtain the linear pressure coefficient.

one can expect the polaron binding energy decreasing upon increasing the pressure. Moreover, the integral of the optical conductivity contribution for the mid-infrared absorption band was calculated according to:

$$SW = \int_0^{\omega} \sigma_1(\omega')\mathrm{d}\omega' = \frac{\omega_p^2}{8}, \tag{4.6}$$

where $\omega = 50000$ cm^{-1}. Figure 4.18(b) shows the plot of the spectral weight (SW) of the mid-infrared band as a function of pressure, where its SW decreases with increasing pressure.

- An additional far-infrared band is observed at around 600 cm^{-1} as shown in Figure 4.19(a). With increasing pressure, it is noticed that a small but a significant shift of this new band to lower frequencies was observed while its SW grows monotonically up to 5 GPa, then it hardly shifted above 6 GPa (see Figure 4.19(b)).

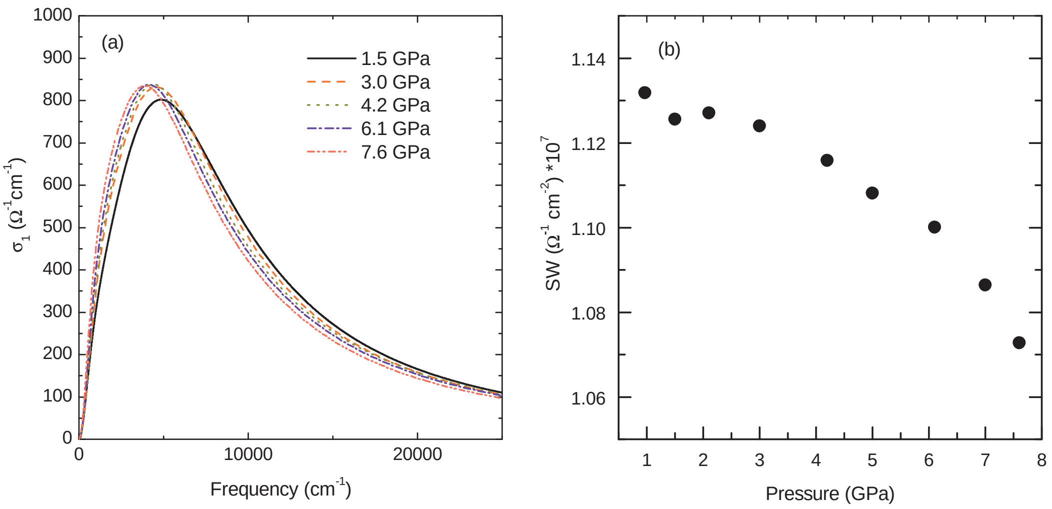

Figure 4.18: MIR absorption band of Fe_3O_4 as a function of pressure extracted by Drude-Lorentz fits of the optical conductivity spectrum. Inset: Spectral weights of the MIR band as a function of pressure.

Two important issues could be addressed from the last observations: First, how to explain the anomaly which appears at around 6 GPa from the spectroscopic point of view. Second, what is the explanation of the origin of the new far-infrared band which is observed at around 600 cm^{-1}. The following is a discussion of these two issues in detail.

The anomaly around 6 GPa

The observed anomaly at around 6 GPa in several contributions of the optical conductivity spectra – saturation of the plasma frequency and σ_{dc} of the Drude term, saturation in the spectral weight of the observed far-infrared band, hardening of the low frequency phonon mode, and the saturation of linewidth of the two phonon modes above 4 GPa – can be attributed to pressure-induced minor changes in the crystal structure which might be due to the occurrence of charge rearrangement within the crystal without changing the structural units or the crystal structure. Interestingly, the charge redistribution between different transition-metal sites due to applied pressure was observed also for β-$Na_{0.33}V_2O_5$ [110, 111], where the pressure induced significant changes in the infrared and Ra-

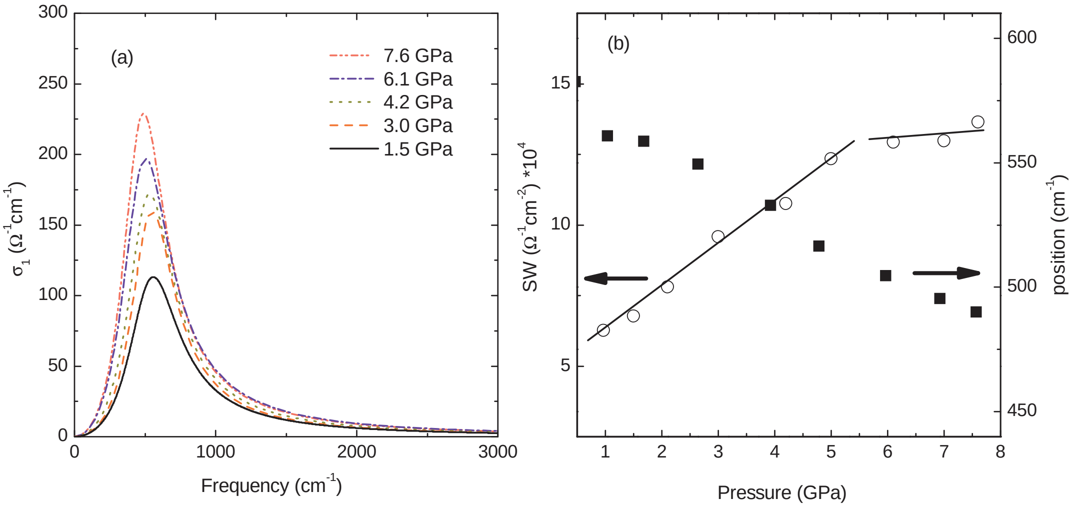

Figure 4.19: (a) Far-infrared band of Fe_3O_4 as a function of pressure extracted by Drude-Lorentz fits of the optical conductivity spectrum. (b) Spectral weights and the position of the far-infrared band as a function of pressure.

man phonon modes which were related to the charge transfer among the different V sites.

Furthermore, as has been mentioned in section 4.3, several anomalies were observed at around 6 GPa for magnetite. The recent thermopower studies of magnetite [95] observed a crossover near (6±1) GPa as a result of the pressure-induced driving of the "perfection" of the electronic transport of magnetite at RT from the "dominant" inverse spinel towards an "ideal" inverse spinel via polaron hopping motion. Furthermore, at RT tiny anomalies are observed in the earlier pressure dependance of the refined hyperfine interaction parameters of magnetite at around 7 GPa and it was claimed to be related to the discontinuous change of the Fe-O bond length [94]. Additionally, the optical conductivity data at low temperature [89] show a sudden increase of the linewidth of several phonon modes near T_v, which was attributed to the weak splitting of the phonons because of the lowering of the crystal symmetry.

Polaronic band

A further open issue is the nature of the polarons in magnetite which will be discussed in detail as follows: From the fact that the nature of the polaron is given by the shape of the MIR absorption band (see Figures 2.12 and 2.13), our optical conductivity data have been analyzed using different theoretical polaron investigations: (i) Large polaron model and (ii) Small polaron model, which are discussed in details in section 2.2.1, in order to further substantiate the above qualitative polaronic picture.

(i) **For the large polaron**: Our optical conductivity data were fitted by using equation 2.13 which was suggested by Emin [26]. By assuming the effective mass for the large polaron to be equal to the free electron mass m_e, the good fitting to our data at 1.5 GPa by using equation (2.13) was achieved with the parameters $n_{\mathrm{P}} = 3.0\times\ 10^{21}$ cm^{-3}, $E_P = 327$ cm^{-1}, and $R = 1.3$ $\mathring{A}$. As shown in Figure 4.20(a), it seems that the LP model describes the asymmetric lineshape of the MIR band reasonably well. Assuming that the conduction via polarons takes place among the octahedral B-sites of the spinel structure, the effective number of charge carriers, N_{eff}, can be estimated from n_P according to

$$N_{eff} = n_P \times \frac{V}{N}, \tag{4.7}$$

where N is the number of B-site atoms (N=16) and V is the volume of the fcc unit cell (V=8.394 Å^3) [112]. The resulting N_{eff}=0.11 can be compared with the effective number of carriers per site obtained from the spectral weight of the MIR band for LPs (see Figure 4.20) according to

$$N_{eff} = [2m_e V/(\pi e^2)]/N \int \sigma_1(\omega')d\omega', \tag{4.8}$$

where m_e and V are the free electron mass and the unit cell volume, respectively. The so-obtained value N_{eff}=0.24 is approximately a factor of two higher than the value from the fitting of the MIR band. It is also a factor ≈5 higher than the value obtained from the sum rule [91]. Furthermore, the value of the LP radius R is smaller than the B–B distance, $a_c\sqrt{2}/4$=2.97 Å with the lattice constant a_c=8.394 Å[112, 113], which is in disagreement with the LP scenario, hence as mentioned in section 2.2.1 the LP radius should extend over multiple lattice sites [26]. This questions the applicability of the LP model for describing the optical data of magnetite [1].

(ii) **For the small polaron model**: Our optical conductivity data were fitted by using the Fratini model [28]. First, the adiabaticity ratio was estimated from our optical data to know whether magnetite belong to the antiadiabatic regime ($\gamma \gg 1$) or to the adiabatic regime ($\gamma \ll 1$). By using the estimated value of the half band width obtained from the calculations of Piekarz [114] $D \approx 0.7$ eV and hence the phonon energies $\omega_0 \approx 75$ meV, the adiabatic ratio for magnetite can be estimated $\gamma \approx 0.1$ eV. From Ref. [28] it was found that this value refers to the formula which was obtained in the adiabatic regime. Additionally, the estimated value for the coupling strength λ for magnetite is, $\lambda = E_{\mathrm{P}}/D \approx 0.52$ at ambient condition, where the polaron binding energy E_{P} was estimated from the position of the MIR band, hence as mentioned in section 2.2.1 that $\omega_{max} \approx 2E_{\mathrm{P}}$ for the small polaron excitations. From the previous estimated values, it is concluded that magnetite lies in an intermediate electron-phonon coupling regime (see Figure 2.16). Hence, there is no analytic expression for this regime but from the estimated value for the coupling strength λ it will be assumed that magnetite lies in the lower boundary of the strong-coupling regime.

Moreover, as mentioned in section 2.2.1, the analytical expressions for the small polaron contribution to the optical conductivity in the adiabatic regime based on DMFT have been interpreted by several authors depending on the ratio between the bandwidth D and the variance s of the phonon-induced broadening of the electronic levels (see equation (2.16)). By checking both of the boundaries ($s \gg D$, and $s \ll D$) it is found that:

- For $s \gg D$: By fitting the mid-infrared absorption band of our optical conductivity spectra at 1.5 GPa via using equation (2.17), the dc conductivity $\sigma(0, \beta) = 34\ \Omega^{-1}\ \mathrm{cm}^{-1}$ and $E_{\mathrm{A}} = 1331\ \mathrm{cm}^{-1}$ (165 meV) were obtained as

---

[1] The discrepancies cannot be reconciled by considering a larger effective mass due to electronic correlations: For $m = 100 \cdot m_e$, as obtained in Ref. [89], a good fit of the MIR band can only be obtained with the fitting parameters $n_P = 3.1 \cdot 10^{23}\ \mathrm{cm}^{-3}$, $E_p = 276\ \mathrm{cm}^{-1}$, and $R = 0.1$ Å.

the best fitting parameters. The so-obtained value of the thermal activation energy from the fitting is consistent with the estimated values from earlier infrared studies [89]. Nevertheless, as shown in Figure 4.20(a), there is a large discrepancy between the fitting curve and the measured data.

- For the opposite limit ($s \ll D$): By fitting our optical conductivity spectra at 1.5 GPa using Eqn.(2.18), it was found that the obtained fitting curve by using this model is more reasonable (see Figure 4.20(a)). Additionally, with increasing the pressure the values of the $2E_\mathrm{P}$, obtained from the fitting parameters, shows a redshift, as presented in Figure 4.20(b). This means that the mid-infrared absorption band is shifted to lower frequencies with increasing pressure.

Depending on the above theoretical models, it can be concluded that the SP model, in the limit ($s \ll D$), is describing well the shape of the mid-infrared band as shown in Figure 4.20(a), while the fitting with the LP model is excluded because the obtained polaron radius from the fitting is very small.

Furthermore, as has been mentioned in section 2.2.1, the temperature dependance of the dc transport data above T$_v$ is another tool for the quasiparticles related to transport. In the case of magnetite, the curve obtained from of our data does not follow a simple linear behavior as shown in Figure 4.21. Here, we will focus on the high temperature range close to room temperature. By fitting our data in the temperature range (250-300K) by using the thermally activated Eqn. (2.22), a hopping energy E_H= 28.5 meV was obtained. This value is a factor of $\approx$ 5 smaller than the activation energy E_A=$E_P/2$ obtained from fitting of our optical data at the lowest pressure by using the small polaron model (E_P= 271 meV at the lowest pressure as shown in Figure 4.20(b)). One has to expect such a discrepancy between the thermal and the optical activation energy, hence in the thermally activated process the lattice has time to relax. In our case, it should be mentioned that such a discrepancy factor between the thermal and the optical activation energy is higher than expected, where the activation energy for the dc conductivity should be half of the optical value. However, we observed a variation in the fitting slope by using Equation (2.22), which leads to a decrease of the discrepancy with decreasing temperature (see Figure 4.21). This

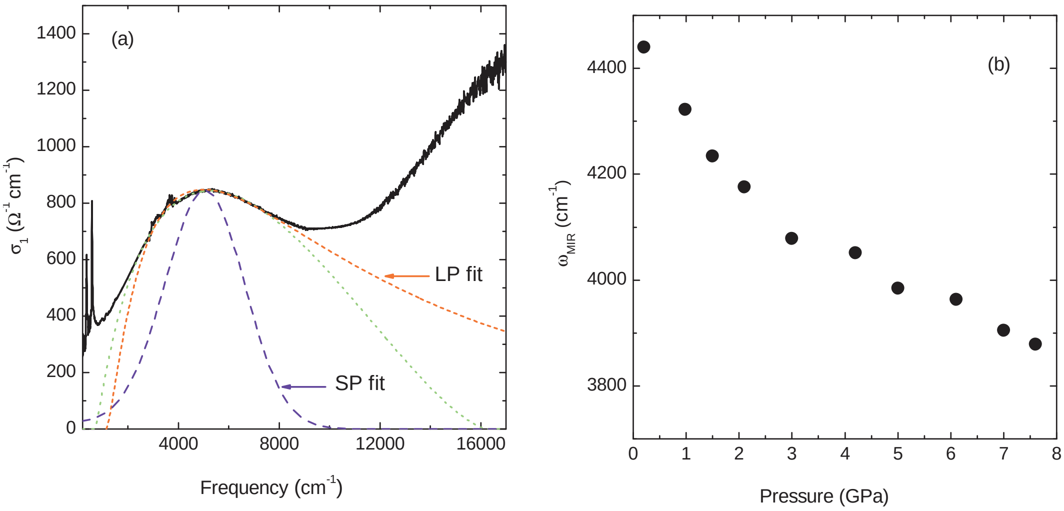

Figure 4.20: (a) Comparison between the fitting curves of the experimental optical conductivity data at 1.5 GPa using the LP model [Eq. (2.13), dashed-dotted line], the SP model in the limit $s \gg D$ [Eq. (2.17), dashed line], and the SP model in the limit $s \ll D$ [Eq. (2.18), dotted line]. (b) The parameter $2E_P$ as a function of pressure, obtained from the fitting using Eq. (2.18).

suggested that the small polaron regime is gradually approached with decreasing the temperature. Interestingly, recent hard X-ray photoemission measurements on Fe_3O_4 [115] observed a gradual variation from the small polaron regime to the large polaron regime during increasing the temperature for the temperature range (250-330 K). Finally, by applying all of these theoretical models to our optical data of Fe_3O_4, it can be concluded that magnetite lies in an intermediate electron-phonon coupling regime and the dominant character is temperature-dependent.

For this intermediate coupling regime, a transfer of the spectral weight to lower frequency is expected, beside the appearance of PIT at frequencies of the order of the phonon frequencies. Interestingly, in our optical data of magnetite under pressure, it was supposed that the observed far-infrared band at around 600 cm^{-1} has a polaronic nature (PIT). This band shifts to lower energy while its spectral weight is growing with increasing pressure (see Figure 4.19). As mentioned in section 2.2.1 the appearance of this band was also observed at low temperature for other materials [41, 42]. In β-$Sr_{1/6}V_2O_5$ [41] these peaks have been assigned

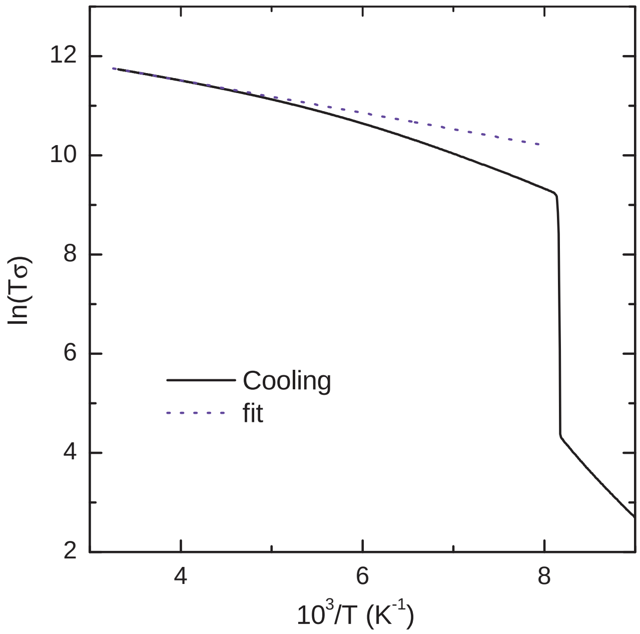

Figure 4.21: Arrhenius plot (solid line) and fit (dashed line) of the ln(σT) at temperatures between 250 and 300 K according to equation (2.22) for small polaron hopping.

to a small polaron absorption for intermediate electron-phonon coupling in the adiabatic regime. While in $LaTiO_{3.41}$ [42] they related the appearance of the far-infrared band to the spin degree of freedom which could be involved in the polaron formation beside the vibrational one.

4.7 Infrared reflectance measurements of magnetite under high-pressure and at low-temperature

Within this section, the far-infrared reflectance study of magnetite under pressure up to 10 GPa as a function of temperature is presented. The characteristic phases of magnetite close to the Verwey transition from the infrared spectroscopy point of view are reported here. Our results are compared with the earlier pressure-temperature studies. Based on this, the pressure-temperature phase diagram for magnetite was concluded.

4.7.1 Experimental details for the high-pressure reflectance measurements at low-temperature

In this part of the work, the pressure dependant reflectance measurements of magnetite at low temperature were studied in far-infrared frequency range (200- 700 cm^{-1}). The single crystals of magnetite used in this work were prepared as mention in Ref. [107]. The CryoDAC Mega cell diamond anvil cell with type IIA diamonds was used for pressure generation. The measurements were carried out on a small pieces of Fe_3O_4 (about 140 μm×140 μm) cut from a single crystal polished to a thickness of $\approx$ 50 μm. The sample was loaded into a hole drilled in a CuBe gasket. Finely ground CsI was chosen as quasi-hydrostatic pressure medium. The DAC was then mounted to a continuous-flow helium cryostat (Cryo Vac KONTI cryostat) via a suitable holder. The data were recorded for several pressure cycles between 0 and 10 GPa. For each pressure cycle, the measurements were carried out upon temperature decreasing, where the reflectance spectra were measured at several temperature steps from 300 down to 10 K. The pressure in the diamond anvil cell (DAC) was determined in situ by the ruby luminescence method. After warming up, the applied pressure has to be increased at room temperature. The measurements were carried out using a home-built infrared microscope coupled to the FTIR spectrometer and maintained at the same vacuum conditions, in order to avoid absorption lines of H_2O and CO_2 molecules. All reflectance spectra are refer to the absolute reflectance at the sample-diamond interface, denoted as R_{s-d}. Part of the measurements were carried out at the infrared beamline of the synchrotron radiation source ANKA in Karlsruhe, while the other part was measured in our lab in Augsburg university. The measurements were repeated with many different samples to ensure consistency and reproducibility. All details about the measurement procedures are explained in chapter 2.

4.7.2 Results and discussion

In order to recognize the pressure effects on the Verwey transition temperature in magnetite, the pressure-dependant reflectance measurements in the far-infrared range as a function of temperature [116] were carried out. Figure 4.22 shows the measured reflectance spectra for the pressure cycles at around (2.5, 3.3, 7.8, and 10.1 GPa) for different chosen temperatures. For illustration, there will be an explanation of the changes in the reflectance spectra for the pressure cycle at around 2.5 GPa (as an example). At room temperature, two oxygen phonon modes near 355 cm^{-1} and 565 cm^{-1} are observed for all pressures, consistent with earlier studies [88, 89, 91] and our room temperature study on magnetite under pressure [108], which was discussed in detail in the previous section. As the temperature decreases to 150 K, the overall reflectance spectra started to decreases slowly in a good agreement with the "bad metal" behavior which was observed through the decrease of the dc resistivity with increasing temperature above T_v (see Figure 4.11). As the temperature falls through T_v, a huge decrease in the overall reflectance spectrum is observed which tends to saturate below ≈102 K. Hence, the Verwey transition manifests itself by remarkable changes. Accordingly, the split and the activation of additional phonon modes are observed in the low frequency mode. These changes were even recognized in the phonon modes at temperatures above T_v (below 150 K) due to the stiffening of the lattice under high pressure. Additionally, we noticed slight variation in the whole reflectance spectra between the measured pressure cycles during cooling down, meaning that the applied pressure does not strongly affect the evaluation of the overall reflectance spectra during cooling down. Moreover, the overall reflectance spectra tend to rise slightly through increasing the pressure at a fixed temperature, confirming the observed increase in the conductivity with increasing the pressure which was mentioned by the dc transport [103] and also by our optical conductivity at room temperature under pressure [108], as discussed in the previous section.

In order to analyze the variations in the optical response induced by pressure and temperature, our reflectance spectra were fitted by using the Drude-Lorentz model combined with the Fresnel equation for the normal-incidence reflectivity with taking into account the diamond-sample interface, as explained in detail in the experimental chapter. For example, Figure 4.23 illustrates the fitting curves for the reflectance spectra at around 10.1 GPa for various temperatures, starting from room temperature down to 10 K. To describe well the various excitation in the reflectance spectra starting from room temperature down to 120 K, the fitting parameters have to consist of a Drude term and several Lorentz oscillators.

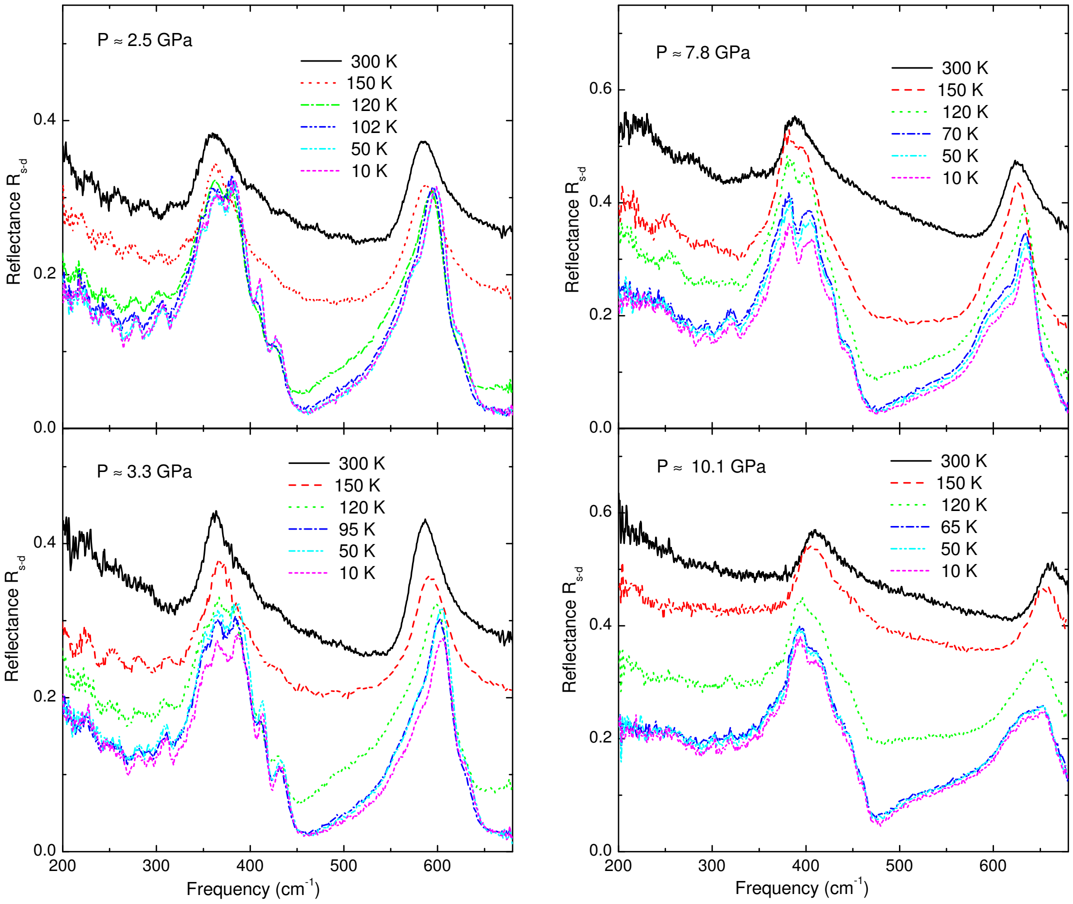

Figure 4.22: Reflectance spectra of magnetite for various temperatures at around 2.5 GPa, 3.3 GPa, 7.8 GPa, and 10.1 GPa.

For the low temperature reflectance spectra (below 120 K) the best fitting was obtained by a sum of Lorentz oscillators for describing the full number of the phonon modes. The related optical conductivity spectra obtained from the fitting of the reflectance are shown in Figure 4.24, while Figure 4.25 shows an example for the obtained real part of the optical conductivity of magnetite together with the various contributions (Drude term, phonon modes) for various temperatures at around 10.1 GPa.

Furthermore, the phonon modes frequency positions were extracted based on

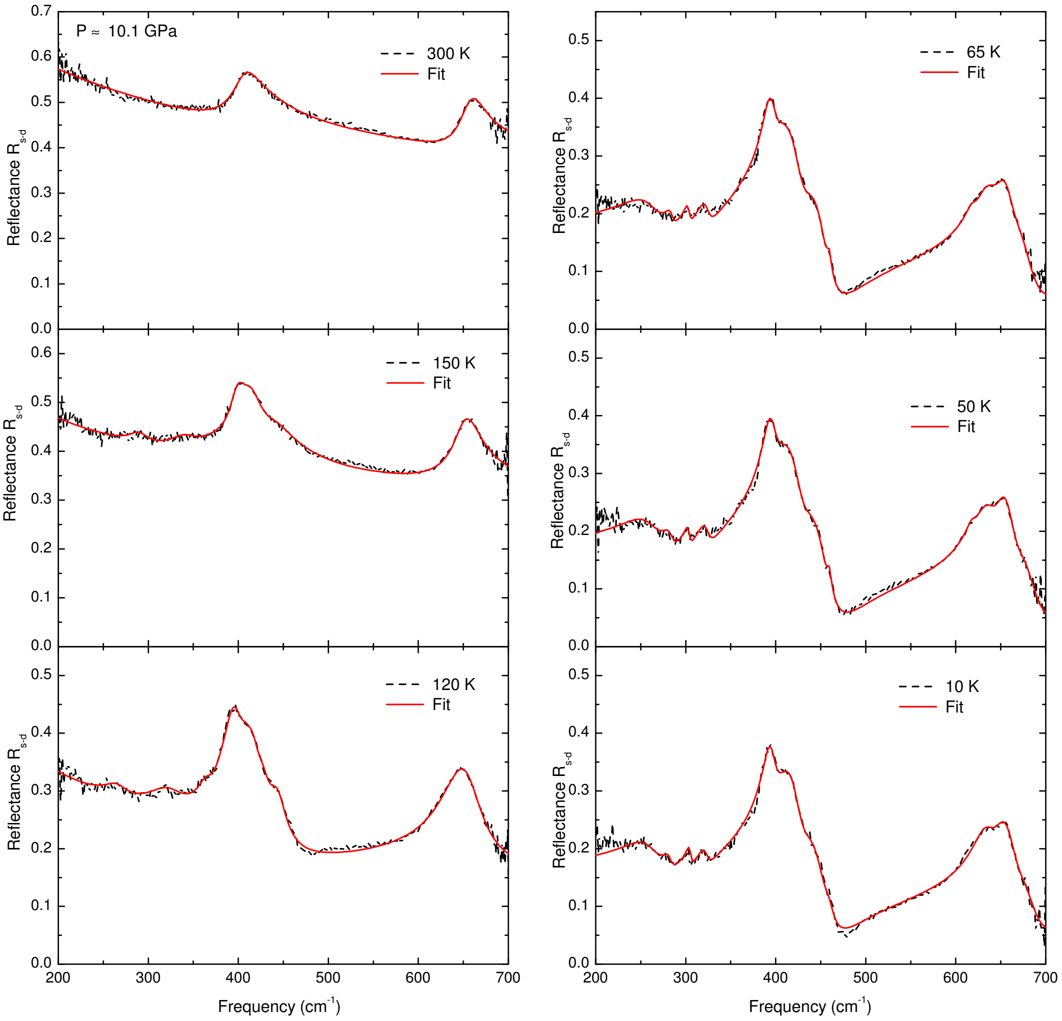

Figure 4.23: The fitting curves based on Drude-Lorentz model for the reflectance spectrum for various temperatures at around 10.1 GPa.

the Drude-Lorentz fitting as a function of temperature for each pressure.

Figure 4.26 shows the phonon modes frequencies as a function of temperature at 2.5, 3.3, 7.8, and 10.1 GPa. Starting from the main two T_{1u} oxygen phonon modes observed at room temperature, there are several splittings and activation of new IR-phonon modes appear upon decreasing the temperature. However, as mentioned in section 4.2, below the Verwey transition magnetite has a different unit cell as a result of the lattice distortion due to the atomic displacement which

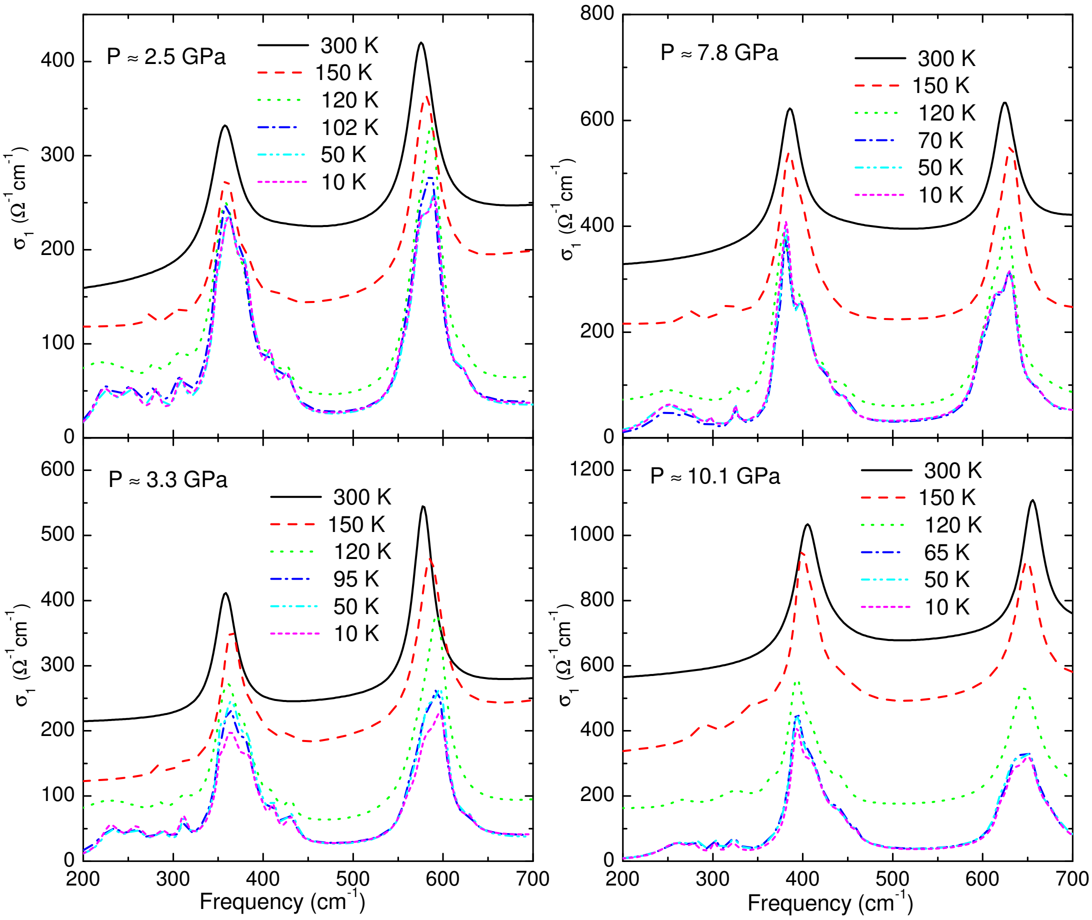

Figure 4.24: Real part of the optical conductivity of magnetite for various temperatures at around 2.5 GPa, 3.3 GPa, 7.8 GPa, and 10.1 GPa, obtained from the fitting of the reflectance spectrum with Drude-Lorantz model.

will lead to a decrease of the crystal symmetry where one can expect a dramatic increase in the number of the phonon modes at low temperature [79]. Depending on our data, it was noticed that the splitting and activation of the expected new phonon modes reached their maximum number below T_v, where no changes are observed in the number of phonon modes down to 10 K. These observed anomalies can be explained as follows: Above the transition the inverse spinel cubic structure (charge-disorder phase) still exists, where most of the phonon modes are highly degenerate modes. Below the transition there is a monoclinic crystal

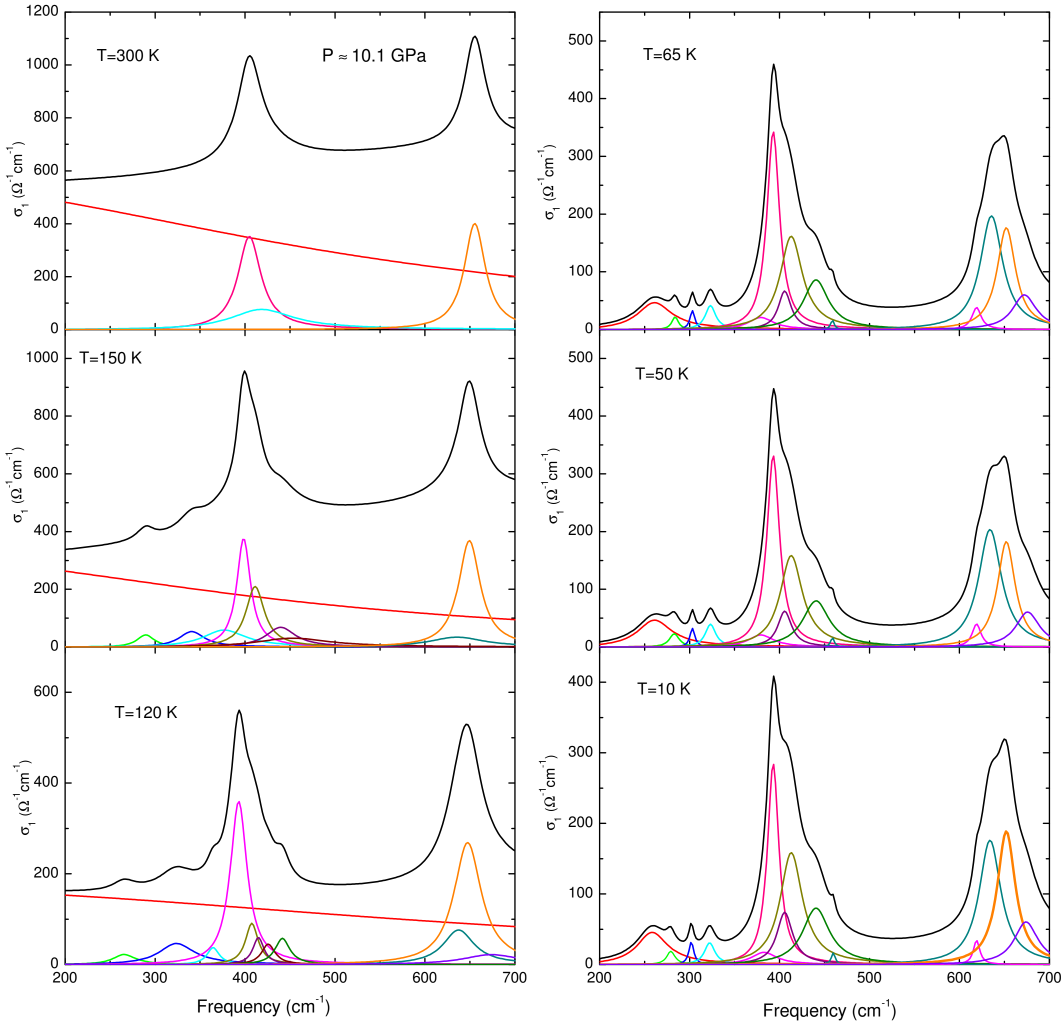

Figure 4.25: The Real part of the optical conductivity of magnetite with the contributions: Drude term , lorentz oscillators at (300, 150, 120 K) and Lorentz oscillators at(65, 50, 10 K), obtained from the fitting at around 10.1 GPa.

structure (charge-ordered phase) leading to reduction of the crystal symmetry and lifting of the degeneracy of modes where only a shift to higher frequencies in the phonon positions is observed with increasing the pressure. Accordingly, the saturation of the number of the phonon modes will be taken as a criterium for entering the charge-ordered phase. Moreover, the activation and the splitting in the phonon modes began to be observed at around 150 K, which is above

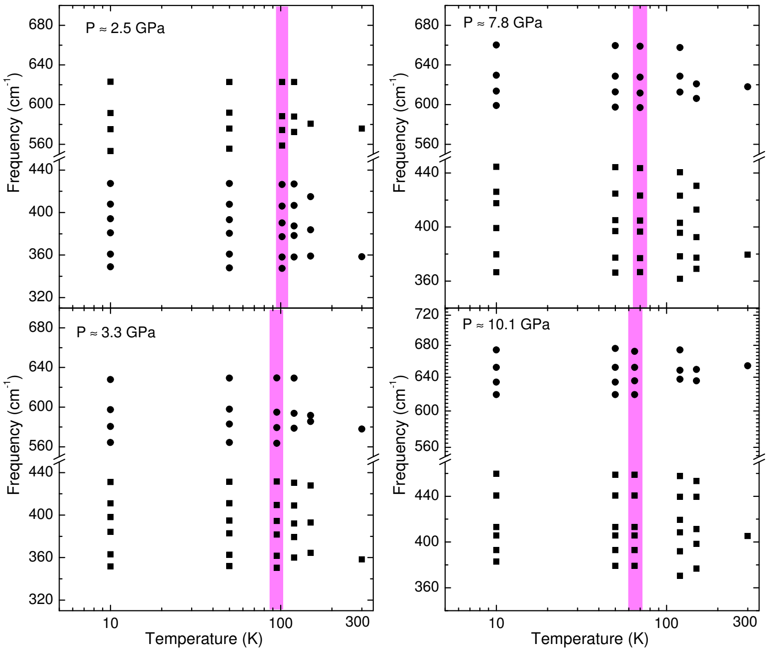

Figure 4.26: The splitting of the two phonon modes observed at room temperature and the activation of the new phonon modes during decreasing the temperature down to 10 K at 2.5, 3.3, 7.8, and 10.1 GPa. The maximum number of the phonon modes is reached at a critical temperature which is highlight with the magenta bar.

the Verwey transition temperature. This is consistent with the previous infrared studies [88, 89, 117]. At a fixed temperature for example at 150 K, it is found that the number of the phonon modes increase with increasing the pressure (see Figure 4.26) which can be explained to be due to the stiffening of the lattice under high pressure.

From our data, there was a possibility to estimate the (P, T) phase diagram between bad metal phase (disorder phase) and insulator phase (charge-order phase) based on two criteria for reaching the lower boundary of T_v:

- The absence of the Drude term which is also combined with the saturation in the down-shift of the reflectance spectra is taken as a first criterium.
- The saturation in the splitting and activation of the phonon modes is taken as a second criterium.

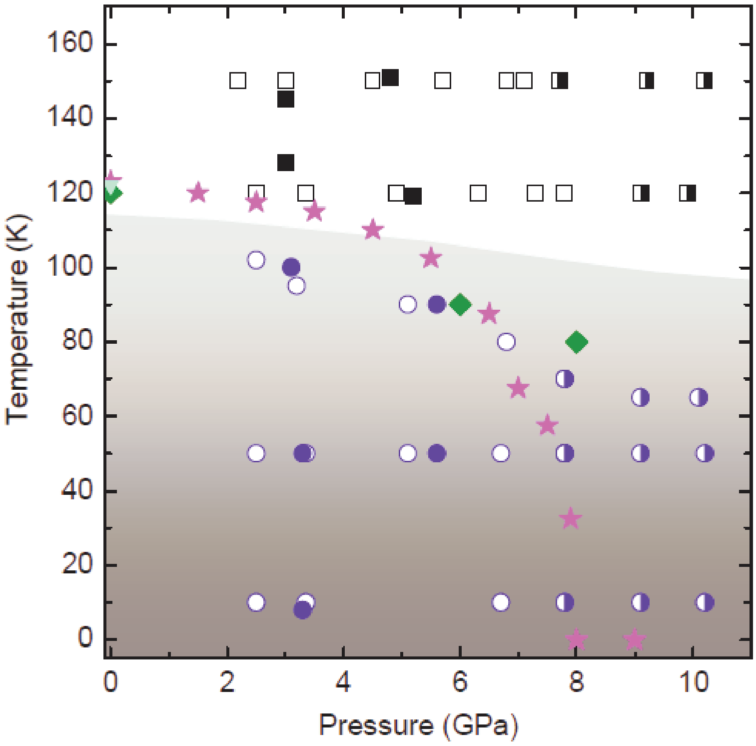

Figure 4.27: Pressure-temperature phase diagram of magnetite for temperatures below 160 K and pressures up to ≈10 GPa. The squares correspond to the "bad metal" state and the circles to the insulating state. The results from three data sets are distinguished by empty, filled, and half-filled symbols. The gray region indicates the charge-ordered, insulating phase as observed by our optical data. The Verwey transition temperature based on earlier dc transport measurements at ambient pressure is marked by the filled down triangle [108].The results for the Verwey transition temperature T_v of Ref. [103] are marked by filled stars, and those of Ref. [99] by filled diamonds.

Figure 4.27 shows the (P, T) phase diagram of magnetite for pressures up to 10 GPa and temperatures from 150 K to 10 K. The displayed data points are based on our data together with the earlier electrical resistivity measurements on the Verwey transition temperature under pressure [103] (filled stars) and Raman measurements [99] (filled diamonds). With increasing the pressure up to 10 GPa the insulator state still exists and no metallic ground state is observed. This is consistent with the previous temperature dependence of the electrical conductivity under pressure, magnetic permeability measurements, the relative conductivity measurements, the thermopower and electrical resistance measurements, and the recent Raman study of the Verwey transition under pressure [93, 97–101]. This finding is in contradiction with the electrical resistivity measurements, the X-ray powder diffraction studies and the recent ac magnetic-susceptibility [102–105], as they claimed the disappearance of the Verwey transition temperature to be due to the metallization of magnetite above 8 GPa and the existence of a quantum critical point.

4.8 Summary

Within this chapter, the electronic and vibrational properties of magnetite under pressure were studied at room temperature for the frequency range (200-18000 cm^{-1}). The main contributions of the optical conductivity spectra in the studied frequency range were: a Drude term, two sharp phonon modes, a far-infrared band at around 600 cm^{-1}, and a pronounced mid-infrared absorption band (polaronic band) around 5000 cm^{-1}. With increasing pressure both absorption bands showed a red shift, while the phonon modes shifted linearly to higher frequencies [108]. The shape of the mid-infrared absorption band was described well by using the SP model in the limit ($s \ll D$). Additionally, the fitting of our dc transport data at low temperature showed that the small polaron regime is expected to dominate at low temperature. Accordingly, the polaronic coupling strength in magnetite at room temperature could be classified rather as intermediate. This was confirmed by the appearance of a far-infrared band in the optical conductivity spectrum at room temperature. At around 6 GPa an anomaly was observed in several contributions of the optical conductivity spectra (saturation of the plasma frequency and σ_{dc} of the Drude term, saturation in the SW of the observed far-infrared band, and an abrupt increase of the linear pressure coefficient for the lower energy phonon mode), which could be due to minor alterations of the charge distribution among the different Fe-sites.

Furthermore, the pressure-dependance of the electronic and vibrational properties of magnetite were studied up to 10 GPa at temperatures from 300 K down to 10 K by far-infrared reflectance measurements [116]. It was found that the Verwey transition manifests itself by remarkable changes, namely:

- The overall reflectance spectra showed a huge decrease followed by a saturation of their down-shift at a critical temperature.
- The splitting of the phonon modes beside the activation of additional phonon modes is due to the lowering of the crystal symmetry, where phonon modes reach their maximum number at a critical temperature.

This critical temperature sets the lower bound for the Verwey transition temperature. Based on these optical results, a pressure-temperature phase diagram for magnetite was proposed. It shows the “bad metal” and the insulating phases. From our data, the sharp drop of T_v to zero and the occurrence of the metallization of magnetite above 8 GPa were ruled out.

Chapter 5

The physical properties of TiOCl

5.1 Introduction

The research on high-Tc superconductors raised a significant interest in low dimensional spin-1/2 transition-metal oxide compounds, in order to understand their strong electronic correlation mechanism and magnetism in low-dimensional structures. This has motivated us to study TiOCl as an example of the spin-1/2 transition-metal oxides series. In this chapter, the basic properties of TiOCl will be summarized. A survey on the previous studies which are important for understanding the electronic properties of TiOCl will be provided. Finally, the results of the current work will be extensively presented and discussed, namely:

- The pressure-induced two structural phase transitions in TiOCl based on the room temperature data from XRD measurements under pressure up to 22 GPa.

- The high-pressure and low-temperature investigations on TiOCl based on the transmittance and reflectance spectra at temperatures from 300 down to 50 K under pressure up to 22 GPa in the mid-infrared frequency range.

5.2 Basic properties of TiOCl

5.2.1 Crystal structure of TiOCl

The structural determination of TiOCl was first achieved by Schäfer et al., in 1958 [118]. TiOCl is formed by distorted $TiCl_2O_4$ octahedra. At ambient conditions, TiOCl crystallizes in an orthorhombic layered structure (FeOCl-type) with space group (Pmmn) and Z = 2 atoms of each sort per unit cell. The lattice parameters at ambient condition are (a=3.789 $\mathring{A}$, b=3.365 $\mathring{A}$, c=8.060 $\mathring{A}$) [70, 119, 120]. Figure 5.1 shows the crystal structure of TiOCl. The basic parts of this structure are the ab-plane which consists of bilayers of Ti^{3+} and O^{2-} ions sandwiched by Cl^- layers along the crystallographic c-axis creating a quasi 2-dimensional structure. The layers repeat themselves along the crystallographic c-axis with only weak van der Waals forces connecting them. Therefore, one expects the existence of a distance which will separate the layers from each other along the crystallographic c-axis and the possibility of the electronic or magnetic interactions will restrict to the ab plane, i.e., to two dimensions. Locally, the strongly distorted octahedra consist of four O ions (two of them belong to the same Ti-O chain, while the other two belong to the neighbouring chain) and two Cl ions lying outside the bilayer where they share edges and corners along the b-axis and along the Ti-O chains in the a-axis, respectively. The distance between Ti ions in different layers (Ti-Ti_{ba} is about 3.17 $\mathring{A}$) is slightly shorter than the Ti-Ti distance within the b layer (Ti-Ti_b= 3.355 $\mathring{A}$) [121, 122]. TiOCl has a side symmetry $C_{2\nu}$ of the Ti ion with a twofold rotational axis parallel to the c-axis and two mirror planes including the c-axis.

5.2.2 Crystal field and band structure

The electronic configuration of Ti is $3d^2 4s^2$ which ionizes to Ti^{3+} in the case of TiOCl leading to the $3d^1$ configuration. Magnetically, the $3d^1$ configuration (i.e., Ti^{3+} ions) forms a spin 1/2 quasi-2D lattice. The octahedral coordination of the Ti-site is an important feature in TiOCl. Within the octahedron unit, the degeneracy of the 3d -orbitals is lifted by electrostatic crystal field. For example, in the local cubic symmetry, the five fold degenerate 3d-orbitals split to the higher-

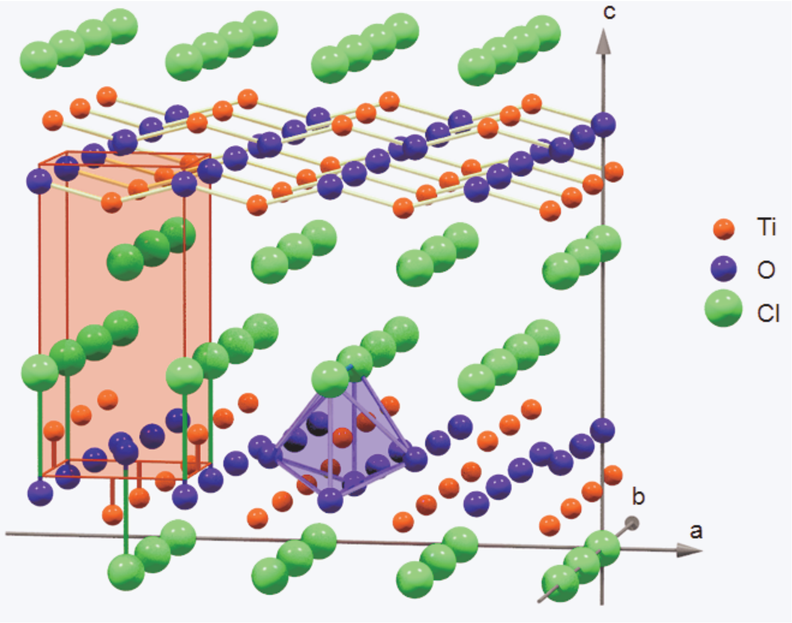

Figure 5.1: Crystal structure of TiOCl. A single bilayer is shown. Note that each Ti is surrounded by 4O and 2Cl, forming a distorted octahedron. These octahedra are corner sharing along *a* and edge sharing along *b*-axis [121].

energy doublet e_g and the lower-energy triplet t_{2g} orbitals (see Figure 5.2). The splitting value is denoted by 10 Dq. In TiOCl crystals, the description of the energy levels is more complex, where the e_g and t_{2g} orbitals will form the e_g band and the t_{2g} band. In the case of $3d^1$ configuration, the Fermi level will intersect the t_{2g} orbitals. Therefore to determine the orbital occupations, the theoretical calculation for the band structure is needed.

The calculation of the band structure of TiOCl and hence the orbital occupation was done by Seidel et al. [121]. First, they calculated the band structure of TiOCl by using the local density approximation (LDA) (see Figure 5.5(a)). They predicted that TiOCl is a metal with a partially filled band, in contrast to the experimental results, where TiOCl at ambient condition is an insulator. In order to solve this contradiction, they modified the (LDA) approximation via adding the orbital dependance of the Coulomb and exchange interactions to the (LDA) approximation. As a result, Seidel et al. arrived to the (LDA+U) calculations [121, 126]. The (LDA+U) calculations predicted that, in the case of the $3d^1$

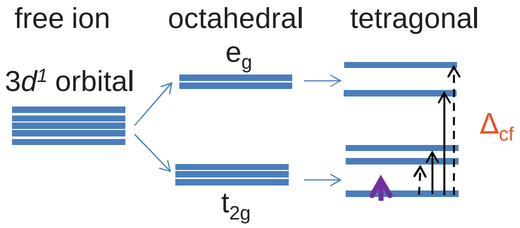

Figure 5.2: Octahedral splitting of 3d-orbitals in TiOCl. The lowest t_{2g} orbital is occupied by one electron, indicated by purple arrow. The full black arrows refer to the allowed optical crystal field excitations.

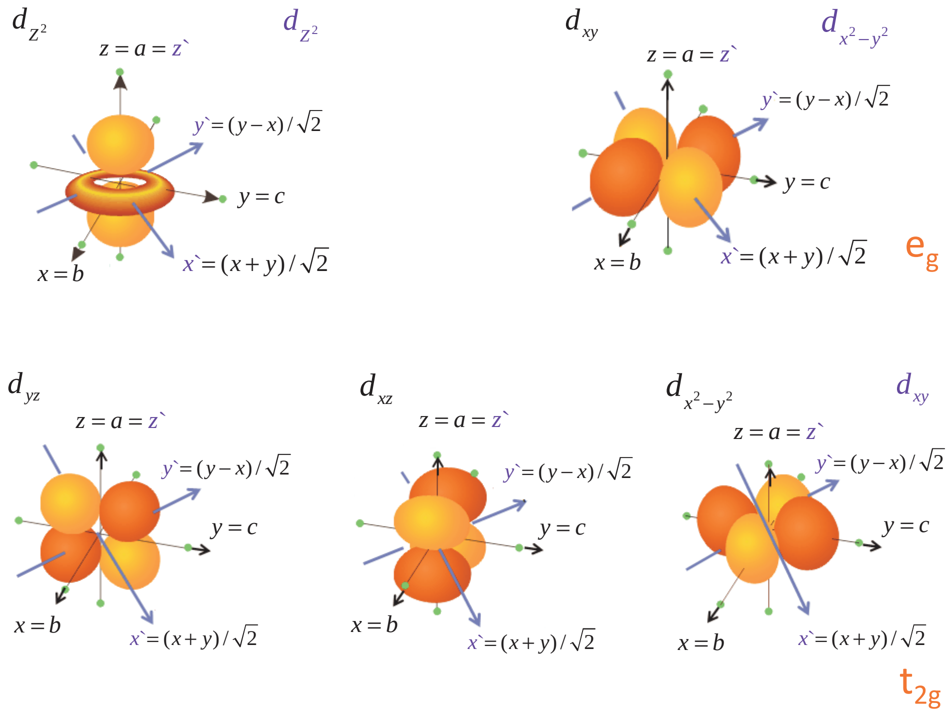

Figure 5.3: Schematic representation of the 3d-orbitals. The nomenclatures with black color refer to the orbitals obtained by using LDA/GGA approximation [123–125], where the axes set z=a, x=b, and y=c (black arrows) were used. The nomenclatures with violet color refer to the orbitals obtained by using Seidel et al. approximation [121], where the axes set z`=$a$ and the $x$`- and y`- axes are rotated by 45° with respect to the b- and c-axes (blue arrows) were used.

electronic configuration, the Fermi level intersects the t_{2g} band where the two degenerate (d_{xz} and d_{yz}) bands will split off from the rest of the t_{2g} bands (d_{xy}) creating a Mott-Hubbard insulator with localized charge carriers. These considerations suggest that the electron of the 3d^1 Ti^{3+} occupies the energetically lowest crystal field level, i.e., d$_{xy}$ level was proposed to be the ground state for TiOCl at ambient conditions (see Figure 5.2). Here, the z-axis is chosen along the crystallographic a-axis and the x- and y- axes are rotated by 45° with respect to the b- and c-axes. With this choice of axes, the d$_{x^2-y^2}$ and d$_{z^2}$ point towards the O and Cl neighbours as is common for the e$_g$ bands. Accordingly, the d$_{xy}$, (d$_{xz}$-d$_{yz}$)/$\sqrt{2}$, and (d$_{xz}$+d$_{yz}$)/$\sqrt{2}$ form the t$_{2g}$ block with d$_{xy}$ being the ground-state orbital and d$_{x^2-y^2}$, d$_{z^2}$ form the e$_g$ block.

The density-functional theory (DFT) calculations within the local-density or generalized-gradient approximation (LDA/GGA) found that this choice of the axes leads to a non-diagonal form of the Hamiltonian [127]. Within the LDA/GGA concepts, the diagonal Hamiltonian will be obtained by choosing z=a, x=b, and y=c as the basis [123–125, 127]. Accordingly, the d$_{x^2-y^2}$, d$_{xz}$, and d$_{yz}$ form the t$_{2g}$ block with d$_{x^2-y^2}$ being the ground-state orbital and d$_{xy}$, d$_{z^2}$ form the e$_g$ block. Thus, the d$_{x^2-y^2}$ orbital is expected to be occupied. Figure 5.3 illustrates the 3d-orbitals with respect to both LDA/GGA concept [123–125](see the black nomenclatures) and Seidel et al. [121] concept (see the blue nomenclatures). The excitation of the 3d^1 Ti^{3+} electron in TiOCl to higher orbitals (i.e., crystal field splitting energies) were obtained by using different theoretical models and experimental techniques [123–125, 127–129]. The excitation energies from the ground state orbital to the other t$_{2g}$ orbitals or the e$_g$ orbitals are presented in table 5.1. Accordingly, the lowest-energy crystal field excitation occurs between the d$_{xy}$-orbital and the (d$_{xz}$+d$_{yz}$)/$\sqrt{2}$-orbital (see the first full black arrow in Figure 5.2). The higher-energy crystal field excitation occurs between the d$_{xy}$-orbital and the d$_{x^2-y^2}$-orbital (see the second full black arrow in Figure 5.2).

The orbital excitations can be directly observed experimentally in the optical conductivity contributions due to the lack of inversion symmetry on the Ti sites. The transmittance measurements on a single crystal of TiOCl for the two polarization directions ($E\|a$, b), at T=300 K and 4 K, were carried out in order to determine the orbital excitations. For $E\|a$, an absorption dip was observed at around 0.6-0.7 eV, while for $E\|a$, an absorption dip was observed at around 1.5-1.6 eV (see Figure 5.4). Above 2 eV, a strong suppression was observed and the sample was opaque due to excitations across the Mott-Hubbard gap. The

Character (Seidel et al. nomenclature)	$d_{x^2-y^2}$ d_{xy}	d_{xz} $(d_{xz}\text{-}d_{yz})/\sqrt{2}$	d_{yz} $(d_{xz}+d_{yz})/\sqrt{2}$	d_{xy} $d_{x^2-y^2}$	d_{z^2} d_{z^2}
GGA	0	0.24	0.46	1.54	2.08
RIXS	0	0.36	0.59	1.45	2.05
Cluster	0	0.25	0.69	1.24	2.11
Optical spectroscopy	0	-	0.65	1.5	-
Polarization	0	-	$E\|a$	$E\|b$	-

Table 5.1: Crystal-field splitting energies (in eV) of $3d^1$ Ti^{3+} in TiOCl and polarization dependance for infrared absorption obtained from different theoretical and experimental methods at room temperature. The GGA results taken from [124, 125], the resonant inelastic x-ray scattering (RIXS) results taken from [123, 125], and optical spectroscopy and cluster model taken from [125, 128, 129]

only difference which was observed between the room temperature spectra and the spectra at 4 K, was the decreasing of the line width with decreasing the temperature as shown in Figure 5.4.

The splitting of the d-orbitals by the crystal field can also seen in the band structure. Hence, varying U will not affect the shape or the width of the occupied bands but its significant effect appears in the splitting between the occupied and unoccupied bands as shown in Figure 5.5(b).

As it was mentioned above, Seidel et al. [121] hypothesized that the d_{xy}-orbital is considered as the predominantly occupied orbital after the splitting and is also responsible for forming a linear chain along the b (or y) direction which supports the one dimensionality of TiOCl. Additionally, the d_{xz} orbital will be responsible for forming a zig-zag chain along the a-direction (see Figure 5.6(a) and (b)). Also, when the Ti sites of one bilayer are projected onto the (a,b) plane, one notices the triangular arrangement of Ti ions between neighbouring chains with the inherent chance of geometrical frustration of the magnetic interactions across the chains [130] (see Figure 5.6(c)). Accordingly, TiOCl with its spin 1/2 magnetic frustration becomes one of the candidates for the investigation of the resonating valence bond (RVB) state [131], which, if doped, could result in exotic superconductivity which is not verified yet[132].

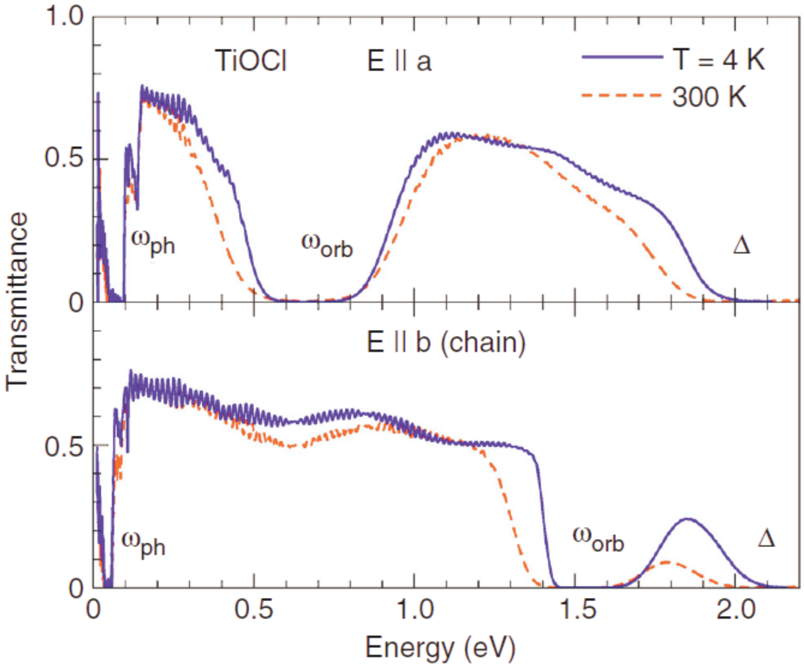

Figure 5.4: (Transmittance spectra of TiOCl with phonon absorption below ≈ 0.1 eV, multi-phonon peaks up to about 0.15 eV, orbital excitations at about 0.65 eV ($E \| a$) and 1.5 eV ($E \| b$), and the Mott-Hubbard gap ≈2 eV. The periodic Fabry-Pérot fringes in the highly transparent range indicate multiple reflections within the sample [128].

5.2.3 Low-temperature phase transitions in TiOCl

In order to prove the scenario of the quasi-one dimensionality of TiOCl, Seidel et al. [121] measured the magnetic susceptibility for this material. They found that TiOCl at high temperature can be described magnetically along the crystallographic *b*-axis as spin-1/2 Ti^{3+} Heisenberg chains, where d_{xy}-orbitals form linear chains running along the b-direction, giving rise to the strong direct exchange between Ti ions on different layers and neglecting the coupling in the other directions. This finding is supported by the electron-spin resonance studies (ESR) on TiOCl where the analysis of the g tensor justifies this scenario [133]. Then by fitting the high-temperature range of the data (above 130 K) to the Bonner-Fisher curve which is described numerically by

$$B(x) = \frac{A + Bx}{C + Dx + x^2}, \tag{5.1}$$

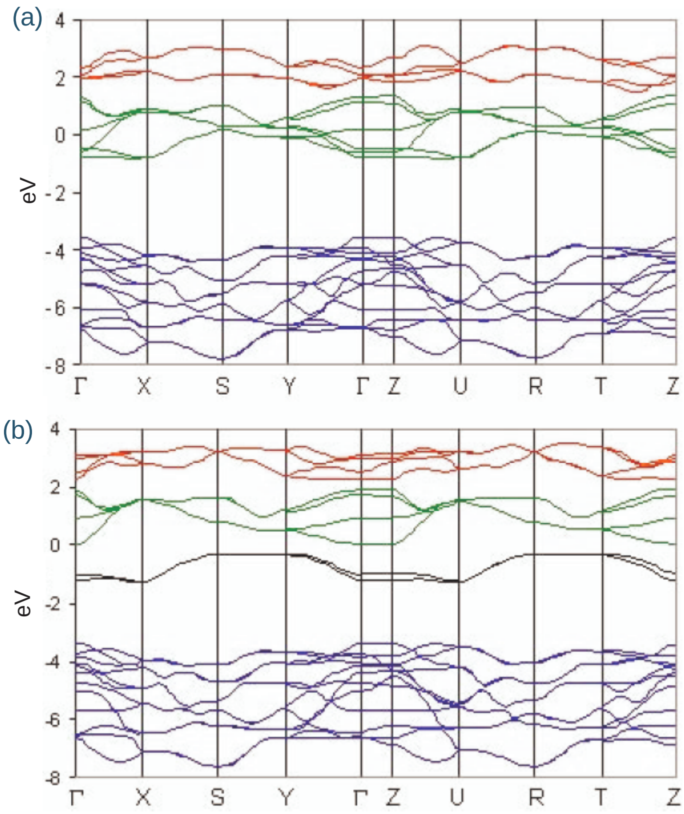

Figure 5.5: (LDA) band-structure calculation for TiOCl. The Brillouin zone is orthorhombic with $X = 2\pi\hat{x}/a$, $Y = 2\pi\hat{x}/b$, $Z = 2\pi\hat{x}/c$ and S is the zone corner. The unit cell contains 2 Ti atoms. 6 bands around the Fermi level are identified as t_{2g} bands well separated from the e_g bands. (b) (LDA+U) band-structure calculation with split-off d_{xy} bands (see the black lines) [121].

where A, B, C, D are constants. $x = T/J$, where J is the exchange constant[1]. It was found that the data followed the Bonner-Fisher model above 130 K with a relatively high nearest-neighbour exchange constant $J = 660$ K. Upon cooling down, a drop in the magnetic susceptibility data was observed at around 130 K, in good agreement with the picture of the opening of a spin pseudogap at T≈135 K due to the structural fluctuations, which were detected by NMR [134]. By further cooling down, a kink at around $T_{c2} = 92$ K is observed followed by a sharp drop to zero at around $T_{c1} = 65$ K (see Figure 5.7). This could be

---

[1] The exchange constant is given by $J = 4t/U$ where t is the nearest neighbour hopping in a one-dimensional tight binding model.

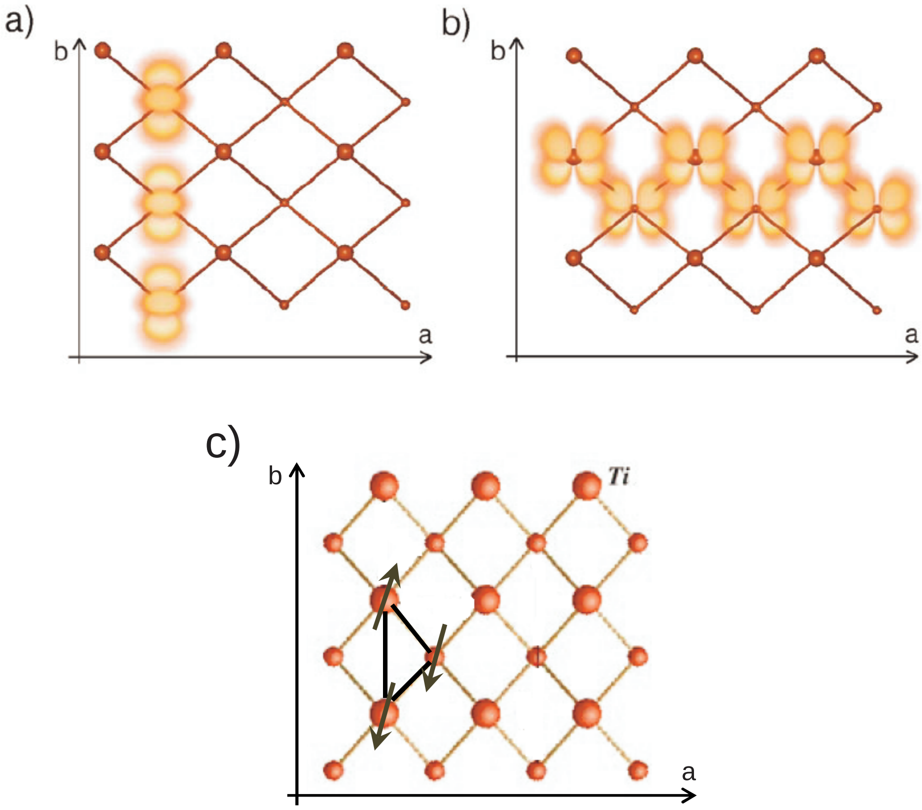

Figure 5.6: Top view on linear, zig-zag chains and triangular arrangement of Ti ions. (a) Linear chains along the *b*-direction formed by the d_{xy} orbitals. (b) Zig-zag chains along the *a*-direction formed by d_{xz} orbitals. Note that the plane of the orbital is tilted by 45° out of the plane and two of its lobes point directly at the Ti ions on the adjacent layer [121]. (c) Triangular Ti mesh of TiOCl, projected along the *c*-axis [130].

ascribed to the dimerization of the chains of Ti ions along the *b*-axis with their spins coupled by direct exchange during cooling down, leading to a nonmagnetic ground state[121, 133, 135].

Not only the magnetic susceptibility is a useful tool to characterize the phase transitions of TiOCl at low temperature but also other techniques (e.g., thermal expansion, specific heat, NMR, ESR, and XRD) are used. As shown in the lower panel of Figure 5.8, the heat capacity shows two peaks at the temperatures T_{c1} and T_{c2}. By analyzing these peaks by using one Debye- and two Einstein-like parts, they obtained a small amount of residual entropy (ΔS) released at the

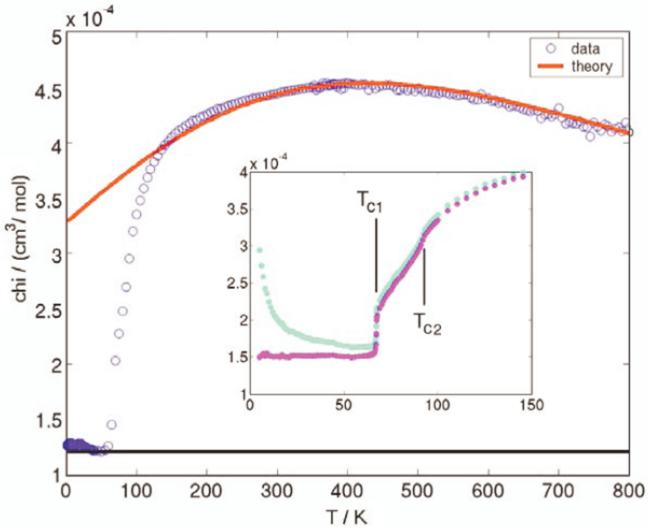

Figure 5.7: Susceptibility of crushed crystals of pure TiOCl. The inset shows single crystal data with and without subtraction of the small curie tail resulting from paramagnetic impurites within the sample [121].

two transitions of $\Delta S = 0.12R^1$ compared to the expected value for spin S=1/2 system or a doubly-degenerate orbital state $\Delta S = R \ln 2$ [136]. Furthermore, the XRD measurements along (2, k, -1) [135, 137] show that the phase transition at T_{c2} corresponds to lowering of the lattice symmetry than orthorhombic. At T_{c1}, a superlattice reflection develops at (2, 1.5, -1) with a doubling of the lattice constant b along the chains of the Ti atoms, leading to the formation of spin-singlet pairs through direct exchange between neighbouring Ti atoms.

In this respect, it can be concluded that TiOCl undergoes two consecutive phase transitions, one of first-order nature at T_{c1} = 67 K followed by another one of a second-order nature at T_{c2} = 91 K. Below T_{c1} = 67 K, the chains are commensurately dimerized with the lattice [135, 138] and a spin gap opens where the Ti^{3+} ions are simultaneously dimerized, which leads to a singlet dimerization of the lattice, supporting the spin-Peierls transition scenario [2]. In between T_{c1}

---

[1] R is the ratio of Debye to Einstein modes and the ratio between the Einstein modes.

[2] The spin-Peierls transition is the transition from the uniform chain to the dimerized chain among the nearest neighbour spin interaction. The spin-Peierls scenario was first observed in the organic compound TTF-CUBDT. After several years, $CuGeO_3$ was the first inorganic compound described the spin-Peierls system. During the last decade, TiOX(X=Cl, Br) has been distinguished as new inorganic candidate for a spin-Peierls system.[121, 133, 135, 139]

and T_{c2}, the chains are dimerized incommensurately [135, 137, 139], which is expected due to the frustration of the interchain interactions in the TiOCl bilayers. Accordingly, this finding supports that TiOCl can be one of the favorite candidates for exotic electronic configurations, as in the RVB state [132] and for superconductivity depending on the dimer fluctuations [121].

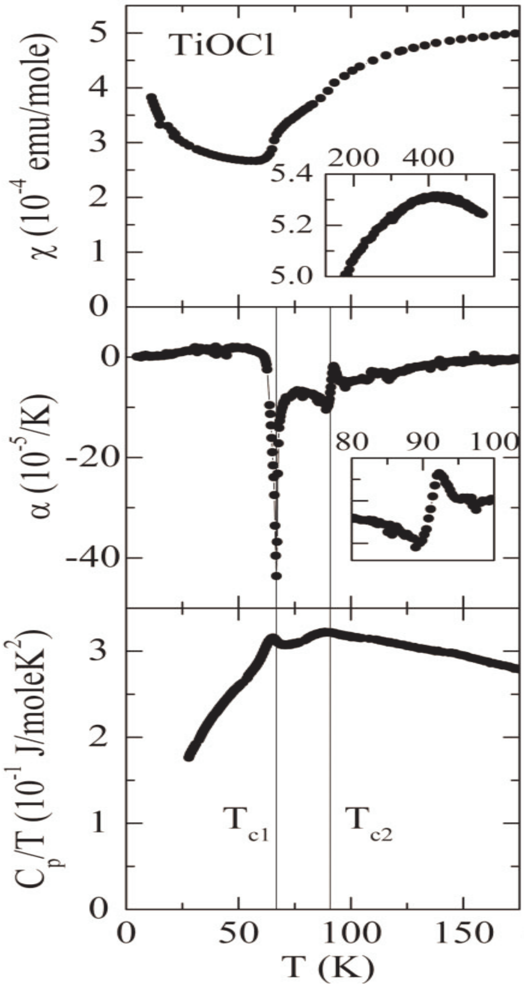

Figure 5.8: Magnetic susceptibility χ, thermal expansion α, and specific heat C_p of TiOCl [128].

5.3 An Overview of the pressure studies on TiOCl

Understanding the metallization of the Mott insulator in strongly correlated systems is still one of the greatest tasks in the condensed matter physics since the discovery of high-temperature superconductivity. As mentioned in chapter 2, a Mott-insulator can be driven into the metallic phase by two ways:

- Application of chemical doping leading to a change in the band filling.
- Application of chemical or external hydrostatic pressure leading to a change in bandwidth, i.e. electron correlation strength (U/t).

In this respect, TiOCl as a Mott insulator, is an interesting compound for investigating the external pressure-induced metal-insulator transition. The focus here will be only on the effects of applying hydrostatic pressure on the properties of TiOCl. The previous high-pressure infrared spectroscopy studies of our group on TiOCl at room temperature [70, 130, 140, 141] found a remarkable change in the optical response: At a critical pressure P_c, depending on the hydrostaticity of the pressure medium, a strong suppression of the transmission spectra was observed in the energy range from near-infrared to visible, associated with a change of the sample colour from orange to black (see Figure 5.9(c)). Below P_c, two absorption peaks were observed at around 0.66 eV and 1.53 eV in the transmittance spectra due to the excitation between the Ti 3d energy levels as shown in Figure 5.9(a,b), similar to the room temperature observations which were discussed in details in Section 5.2.2. These absorption peaks are broadened and show a blue shift with increasing the pressure, suggesting the increase in the crystal field splitting of the Ti 3d levels [140]. Furthermore, above this critical pressure an abrupt increase in the reflectance spectra was observed. These changes were attributed to the appearance of additional charge excitations which fill the Mott gap and give also an indication of the pressure-induced metal-insulator transition. For understanding the observed changes in the optical properties, our group furthermore studied the pressure effect on the crystal structure of TiOCl by using the x-ray powder diffraction technique [70]. Pronounced changes of the diffraction diagram at P_c

were observed which indicate the pressure-induced structural phase transition but resolving the crystal structure above P_c was not specified, which will be clarified in section 5.4.

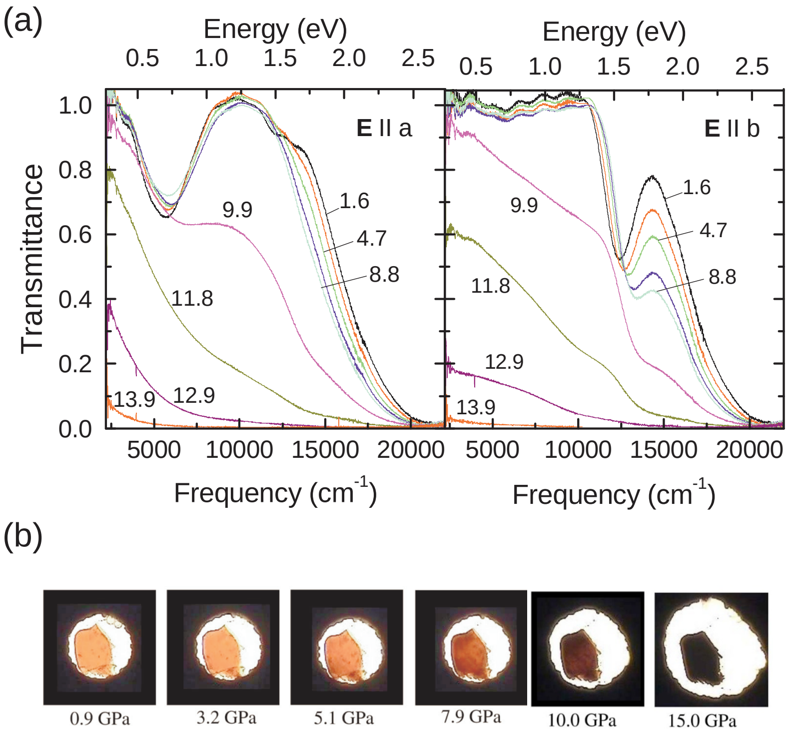

Figure 5.9: (a) Room temperature transmittance spectra of TiOCl as a function of pressure for the polarization $E\|a$ and $E\|b$. (b) View inside the diamond anvil cell during the pressure-dependent optical measurements, where the sample colour changes from orange to black with pressure increasing, while the sample completely recovers to its original colour during releasing the pressure [140].

In contrast, the temperature dependance of the electric transport on a TiOCl polycrystalline sample up to 24 GPa [142] ruled out that pressure induces an insulator-to-metal transition, where they found an anomalous decrease of the activation energy with increasing pressure around a critical pressure $P \approx 13$ GPa at room temperature, which indicates an electronic structure change above this critical pressure (see Figure 5.10). From the decrease of the activation energy ($E_g \approx 0.3$ eV) and the high increase of the specific resistivity ($\rho \approx 10^{-1}$ Ωcm) an insulator-to-semiconductor transition was predicted. This estimation was confirmed by their x-ray powder diffraction analysis under pressure. This analysis shows an anomalous compression of the lattice parameter a above 11 GPa with respect to the decrease of the lattice parameters b and c, indicating the pressure independence of the effective hopping along the a axis. This finding supports their insulator-to-semiconductor transition scenario up to 24 GPa [142]. Here, it must be noticed that the quality of the contacts and the transport across grain boundaries in a polycrystalline sample might affect the results. This is why the electric transport measurements on single crystals along the ab plane are needed, but first one must be sure about the contact quality which is not an easy task.

Recently, the high pressure x-ray diffraction measurements on TiOCl by Blanco-Canosa et al. [120], have confirmed the occurrence of a structural phase transition above 10 GPa, which was predicted by Refs. [70, 140, 142]. This observed phase transition changes the structure from the orthorhombic phase (space group Pmmn) to the monoclinic phase (space group $P2_1/m$) and is combined with strong dimerization of the Ti^{3+} ions along the b axis at room temperature (see Figure 5.11(a)). Additionally, they expected an unusual increase of the spin-Peierls temperature with increasing pressure. Moreover, the extrapolation of the magnetic susceptibility data assumed that the spin-Peierls transition will cross the room temperature at around 10 GPa. Furthermore, a dramatic reduction of the electronic band gap from about 1.5 eV at ambient conditions to approximately 0.3 eV above 10 GPa was expected for the dimerized monoclinic structure (see Figure 5.11(b)), while their *ab intio* theoretical calculations predicted changes in electronic structure due to the structural transitions. Accordingly, a molecular orbital (electron-lattice coupling) will be formed within the dimer which could lead to a crossover from spin-Peierls to usual Peierls dimerization.

Another theoretical study on TiOCl under pressure was achieved via using the Car-Parrinello molecular dynamics model [143]. This research predicted that TiOCl undergoes two phase transitions with increasing the pressure: The first phase transition is an insulator-to-metal transition which happened at the critical pressure $P = P_c$, where all the lattice parameters show sudden changes. Hence, a big compression occurs along the b and c axis, while an expansion occurs along the a axis where we have a superexchange interaction between the Ti ions, as shown in Figure 5.12(b). At this transition a structural change from orthorhombic (Pmmn)

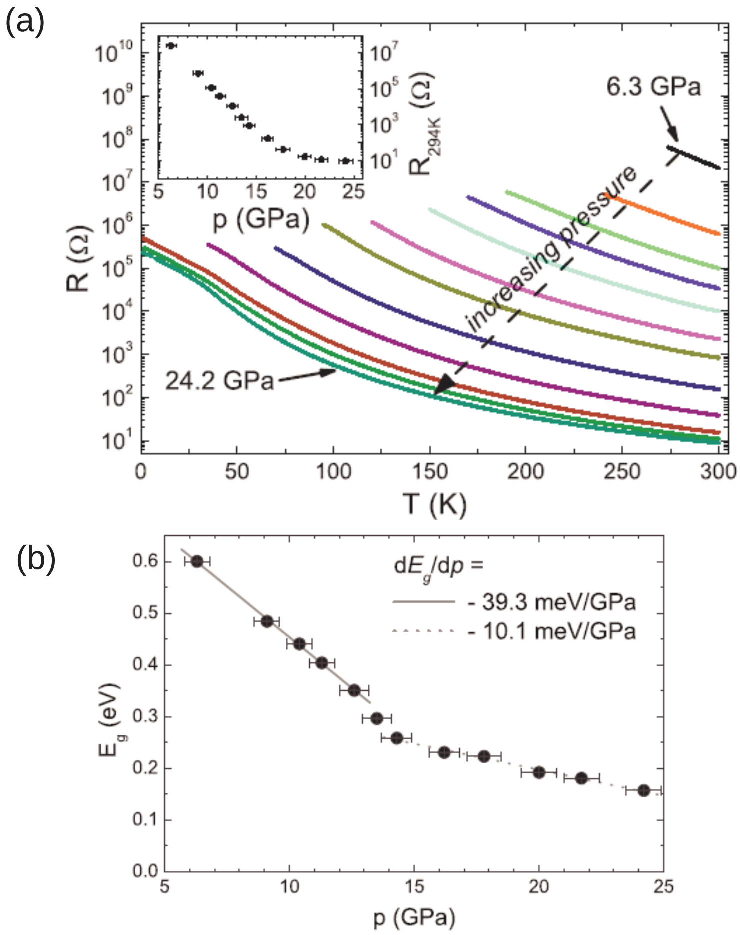

Figure 5.10: (a) Electrical resistance of TiOCl for various pressures between 6.3 and 24.2 GPa in the temperature range 1.6 to 300 K in the logarithmic plot. The inset shows the pressure dependance of the electrical resistance at T=294 K. (b) Pressure dependance of the activation energy around 300 K obtained from the temperature dependance of the electrical resistance [142].

to monoclinic ($P2_1/m$) is predicted, combined with a lattice dimerization along the b axis. At P_c'=1.26P_c, a second phase transition is expected from dimerized metal to a uniform metal (undimerized), where a sudden expansion occurs along the a and b axis, while the lattice along the c axis is compressed more with pressure increasing (see Figure 5.12(b)). At the second phase transition at P_c', a structure change from monoclinic ($P2_1/m$) to orthorhombic (Pmmn) is predicted.

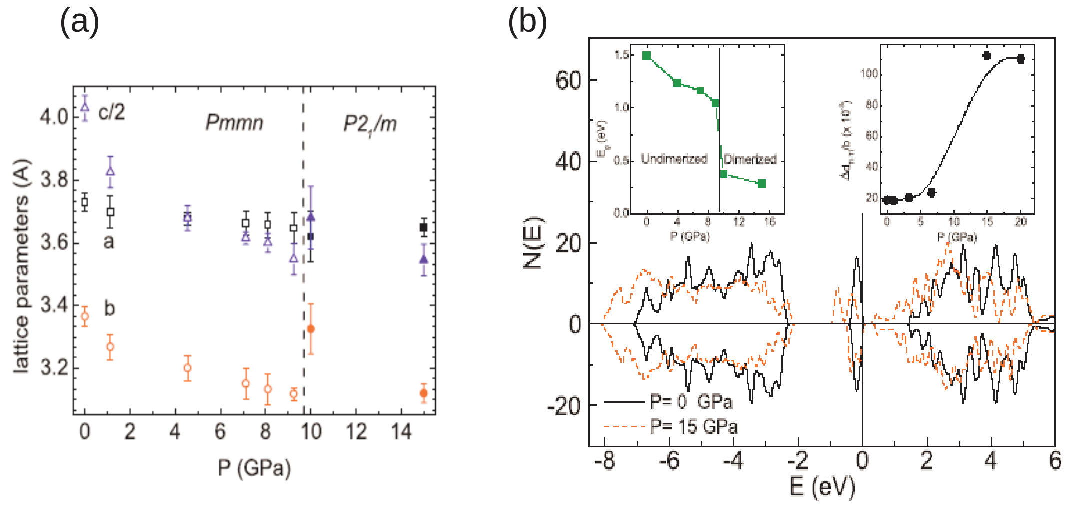

Figure 5.11: (a) Pressure dependance of the lattice parameters of TiOCl at RT as obtained from the Rietveld refinement in both the orthorhombic and monoclinic phase above 10 GPa. (b) Density of states for TiOCl at ambient pressure (Pmmn) and at 15 GPa ($P2_1/m$). The vertical line marks the Fermi energy. [120].

Furthermore, at $P = 0.5\ P_c$, where the insulator phase exists, the DOS shows a gap, which separates the occupied $d_{x^2-y^2}$ state from the unoccupied d_{yz} and d_{xz} states (see Figure 5.12(a)). At $P = 1.03\ P_c$, the gap disappears and the d-states are suddenly rearranged. The Fermi level crosses the d_{yz} and d_{xz} states while a gap within the $d_{x^2-y^2}$ state still exists, indicating an insulator-to-metal transition at P_c. At $P = 1.54\ P_c$, i.e., above P_c', the gap in the $d_{x^2-y^2}$ state and also the structural dimerization along b-direction disappear. The system shows a uniform metallic phase.

In the previous paragraphs, a short summary was given about the pressure effects on TiOCl by using different experimental and theoretical techniques. Within this project, the effects of applying external pressure on the crystal structure of TiOCl up to 25 GPa at room temperature were studied, using x-ray powder diffraction measurements, in order to check the possibility of pressure induced structure phase transitions. Furthermore, in order to follow up the previous work of our group on TiOCl, the transmittance and reflectance spectra of TiOCl were studied at temperatures from 300 down to 50 K under pressure up to 22 GPa

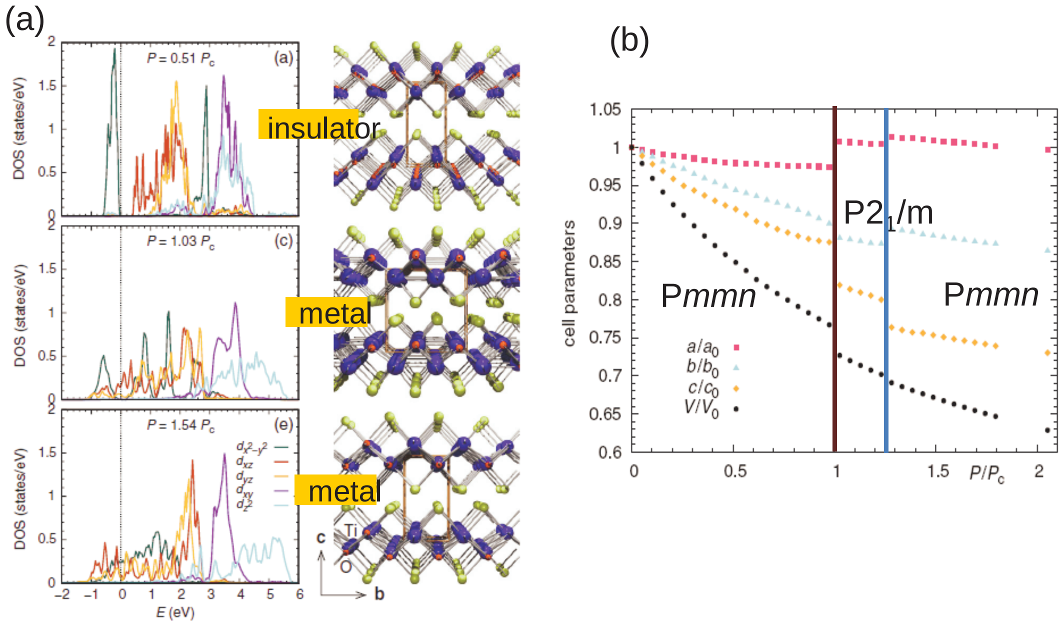

Figure 5.12: (a) a, c, and e are the partial density of states at three different values of pressure in different phases. b, d, and f are the structures at these three different values of pressure. (b) Pressure dependance of the lattice parameters and volume. Pressure is normalized to a critical pressure for the insulator-to-metal transition and the lattice parameters are normalized to their values at ambient pressure [143].

in the mid-infrared frequency range. From the transmittance, the temperature and pressure-dependence of the crystal field splitting could be studied via the frequency position of the orbital excitations. Furthermore, from the pressure dependent reflectance measurements at low temperature, a search was conducted for a direct proof of the existence of the Drude term in the optical response where a large redistribution of the spectral weight of the optical conductivity could occur with the variation of the band width by applying external pressure and/or variation of the temperature. As mentioned in section 2.1.3, the appearance of the Drude term in the optical conductivity spectra below a certain low temperature (T_{coh}) was predicted [10, 13–15], which will be discussed in detail in section 5.6.

5.4 High-pressure XRD-measurements at room temperature

The aim of this section is to reveal the existence of a structural phase transition at high pressure in TiOCl to interpret the observed behaviour of the optical data of TiOCl at high pressure. Within this section the investigation of the crystal structure of TiOCl by x-ray powder diffraction measurements (XRD) is presented as a function of pressure at room temperature, where two structural phase transitions are observed at P_{c1}=15.4 GPa and P_{c2}=22.6 GPa.

5.4.1 Experiment for high-pressure XRD-measurements on TiOCl at room temperature

The single crystals of TiOCl used in this part of the work were provided by the group of Prof. R. Claessen (Würzburg University). The crystals were synthesized by using the chemical vapor transport from $TiCl_3$ and TiO_2, the preparation method is illustrated in Ref. [118]. The structural analysis of TiOCl under high pressure up to 25 GPa was performed by x-ray powder diffraction experiments at the European Synchrotron Radiation Facility(ESRF) on the ID09A high-pressure beamline with monochromatic radiation ($\lambda = 0.4128 \mathring{A}$). The measurements were carried out by C. A. Kuntscher et al. [70]. The membrane-type diamond anvil cell was used for pressure generation. Gaskets were made out of a stainless steel sheet that was pre-pressed to 40 μm. Holes of 150 μm diameter were drilled in the gasket, centered on the indentation. The crystals were gently ground and placed into a diamond-anvil cell (DAC). Helium was used as a pressure transmitting medium. The recorded diffraction patterns were integrated by using the FIT2D program [71], to obtain the intensity versus 2θ diagrams. The LeBail fits were carried out by using JANA 2006 program [72], in order to determine the lattice parameters and hence the unit-cell volume as a function of pressure. All details about the measurement procedure and the method used in analyzing the data are explained in the experimental chapter.

5.4.2 Results and discussion

The resultant integrated data for various measured pressures up to 25 GPa are presented as an intensity versus the diffraction angle 2θ in Figure 5.13. The XRD diffraction diagram shows significant variations in the intensity and multiplicity of the Bragg peaks at P_{c1}=15.4 GPa and at P_{c2}=22.6 GPa, which reveal the existence of two structural phase transitions. With increasing pressure up to 15 GPa, broadening of the Bragg peaks is observed with a progressive displacement of the peaks to higher angles. Above 15 GPa, numerous weak reflections appear in the diffraction pattern which are an evidence of the appearance of a first structural phase transition at P_{c1}. A further increase of the pressure induces again significant changes in the x-ray diffraction diagram indicating a second structural phase transition at P_{c2} [144].

In order to obtain the unit cell parameters as a function of pressure, the diffraction patterns were fitted with the LeBail method by using the crystallographic computing program JANA2006 [72]. The diffraction diagrams of TiOCl for few selected pressures together with the LeBail fits are shown in Figure 5.14. For fitting the lowest-pressure data, it is assumed at ambient condition that there is an orthorhombic unit cell with space group (Pmmn) and lattice parameters a = 3.789 $\AA$, b = 3.365 $\AA$, and c =8.060 $\AA$, consistent with previous studies on TiOCl [70, 119, 120]. The diffraction diagrams up to 15 GPa were fitted well with the ambient-pressure crystal structure (Pmmn). However, the appearance of new diffraction peaks in the diffraction diagrams leads to significant changes in the fitting, indicating a first structural phase transition at P_{c1}. To fit our data for P >15 GPa, a new crystal structure with doubling of the a and b axes (monoclinic crystal structure with space group P2$_1$/m) has to be added in addition to the ambient pressure orthorhombic crystal structure. For the pressure range from 15.4 GPa up to 22 GPa, a good fitting of the diffraction diagrams is achieved with the existence of those two crystal structure phases (the monoclinic crystal structure and the orthorhombic crystal structure). Interestingly, strong changes in the peak intensities and new peaks appeared again above 22 GPa indicating a second structural phase transition at P_{c2}, where the two phases still exist with significant changes in the lattice parameters of the monoclinic phase.

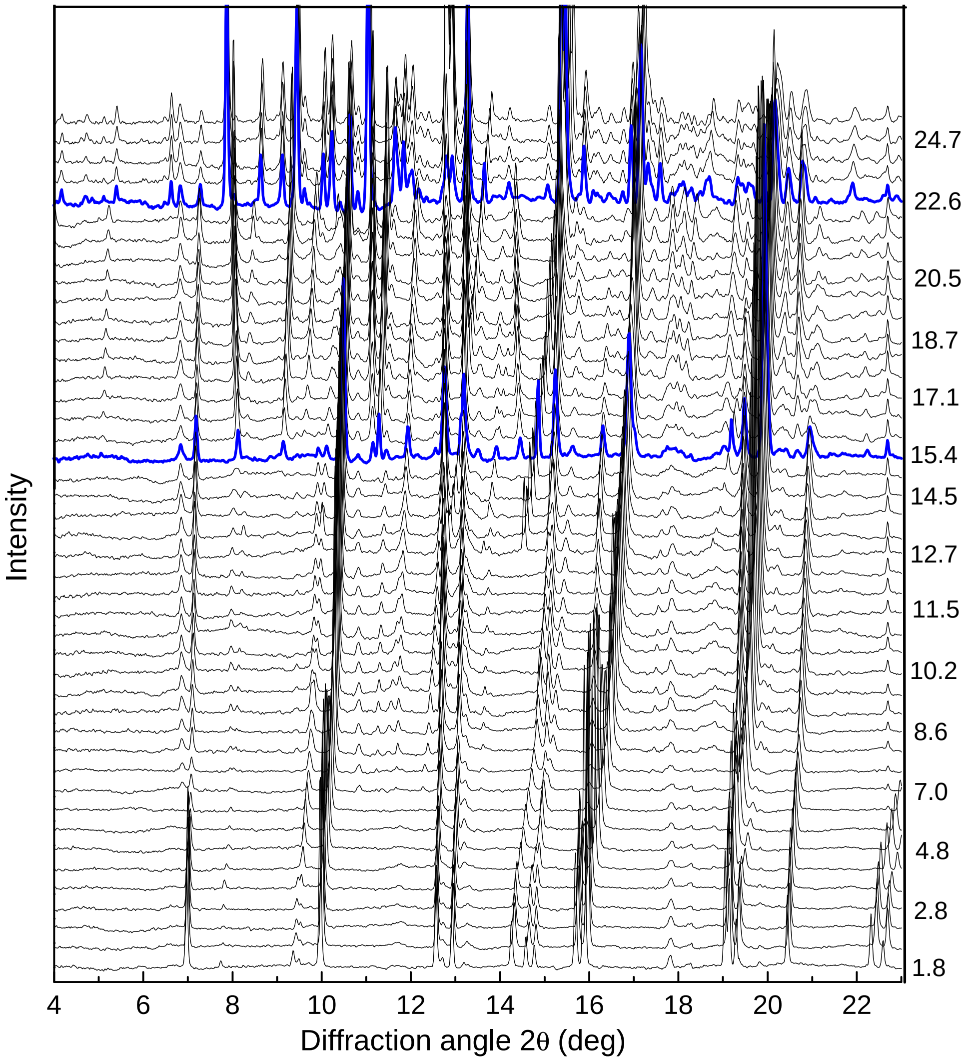

Figure 5.13: Room-temperature x-ray powder diffraction diagrams of TiOCl at high pressures. The numbers on the right, vertical axis indicate the applied pressures in GPa. The diffraction diagrams at the critical pressures P_{c1}=15.4 GPa and P_{c2}=22.6 GPa are highlighted by bold blue lines [144].

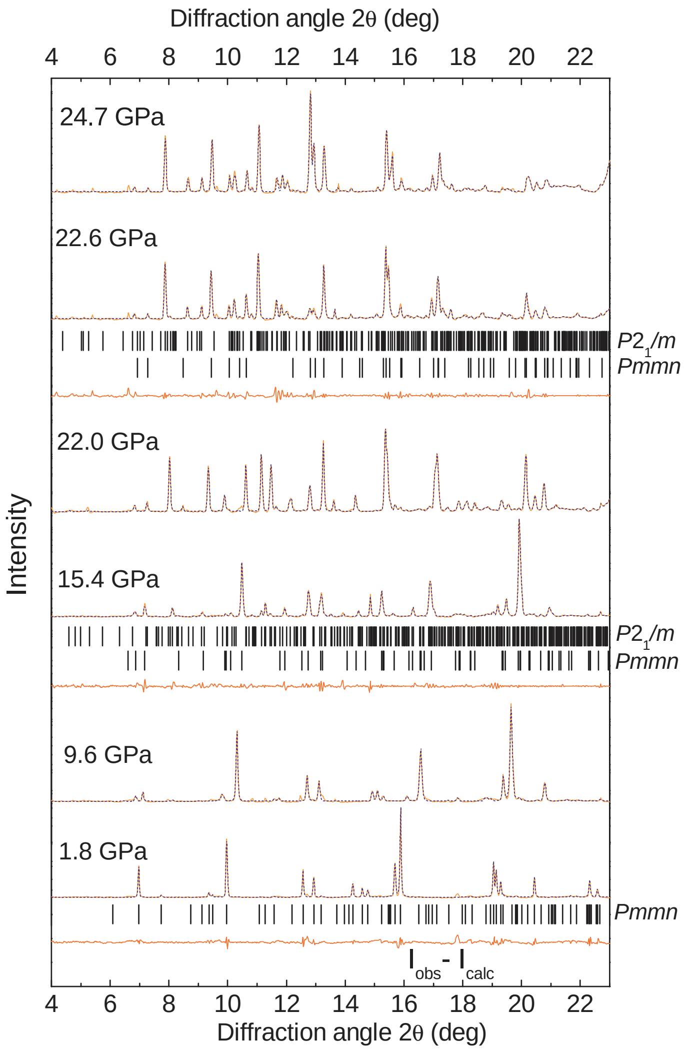

Figure 5.14: Room-temperature x-ray powder diffraction diagrams (full, orange lines) of TiOCl at high pressures together with the Le Bail fits (dotted, blue lines). For the pressures (1.8, 15.4, and 22.6 GPa) the difference curve (I_{obs}-I_{calc}) between the diffraction diagram and the Le Bail fit is shown. Markers show the calculated peak positions for the various phases.

Figures 5.15 and 5.16 show the pressure dependence of the lattice parameters and unit cell volume, which are instructive for the two structural phase transitions. In these figures, the open black symbols ($\triangle, \square, \circ$, and $\diamond$) represent the lattice parameters (a, b, c) of the orthorhombic phase and the unit cell volume respectively, while the full red symbols represent the monoclinic phase. For normalizing the lattice parameters, they were divided by their respective ambient-pressure values [119].

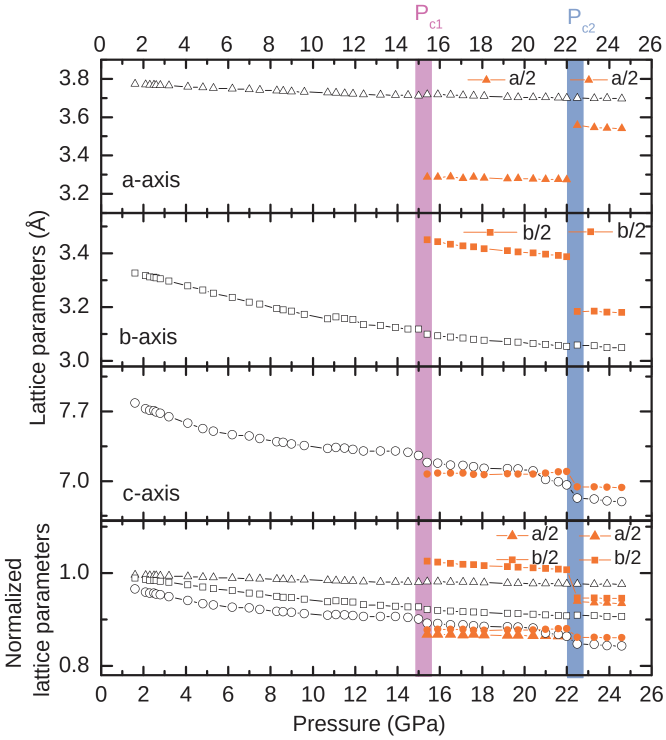

Figure 5.15: Results of the Le Bail fits of the room temperature x-ray powder diffraction diagrams of TiOCl: lattice parameters as a function of pressure.

With increasing the pressure, the orthorhombic phase (space group Pmmn) is clearly influenced, which appears significantly in the anisotropic compression of the lattice parameters. Up to 15 GPa, all lattice parameters for the orthorhombic phase show changes with increasing pressure. For the *ab* plane, it was observed that the *b* axis is much more compressible than the *a* axis in agreement with the previous reported data [70, 120, 130, 143]. Along the *b* axis (the direction of the Ti chains) a direct exchange between Ti-Ti ions is expected, while a superexchange interaction between (Ti-O-Ti) ions is expected along the *a* axis. Furthermore, a high compression is observed along the *c*-axis, where the Van der Waals bonding exists between neighbouring bilayers.

Above the first phase transition P_{c1}, both the monoclinic phase (space group

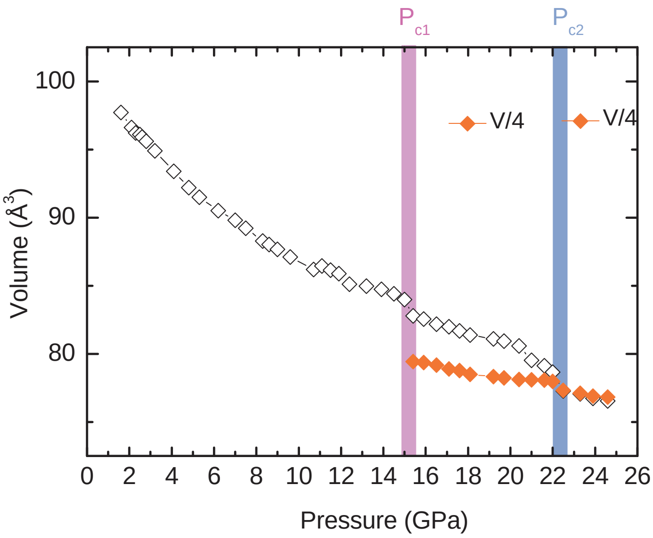

Figure 5.16: Results of the Le-Bail fits of the room temperature x-ray powder diffraction diagrams of TiOCl: unit cell volume as a function of pressure.

P2_1/m) and the orthorhombic phase (space group Pmmn) coexist. Hence the monoclinic phase is characterized by an alternating tilting on the TiO_4Cl_2 octahedra induced by pressure. In order to obtain the best fitting, the monoclinic phase needs to have a b-axis unique with a monoclinic angle β around 98° and the superstructure ($2a\times2b\times c$). As mentioned in section 5.3, the doubling of the b axis in the monoclinic unit cell was observed in the recent high pressure x-ray diffraction measurements at room temperature [120]. They observed a monoclinic crystal structure with a space group P2_1/m $a\times2b\times c$ superstructure and b-axis unique with monoclinic angle $\beta \approx 99^0$ and strong dimerization of the one-dimensional spin chain along the b-axis at around 10 GPa [120]. They supposed that the dimerization is of pure electronic origin and the monoclinic symmetry is not a subgroup of the ambient-pressure orthorhombic symmetry. Therefore, the high-pressure phase requires major rearrangement affecting the connectivity between atoms[120, 144]. In contrast, an approximate doubling of the a axis in the monoclinic unit cell was observed in the recent high-pressure x-ray diffraction measurements at T=6 K as a result of the Fermi-surface nesting of an itinerant electron state [145].

Within the region which lies between the two phase transitions ($15 < P_{c1} <$ 22 GPa), all the lattice parameters of both phases (orthorhombic with Pmmn symmetry and monoclinic with P2$_1$/m symmetry) decrease with increasing pressure leading to a reduction of the unit cell volume, with a slow decrease of the β angle of the monoclinic phase from 98° (at 15.4 GPa) to 97.5° (at 22 GPa).

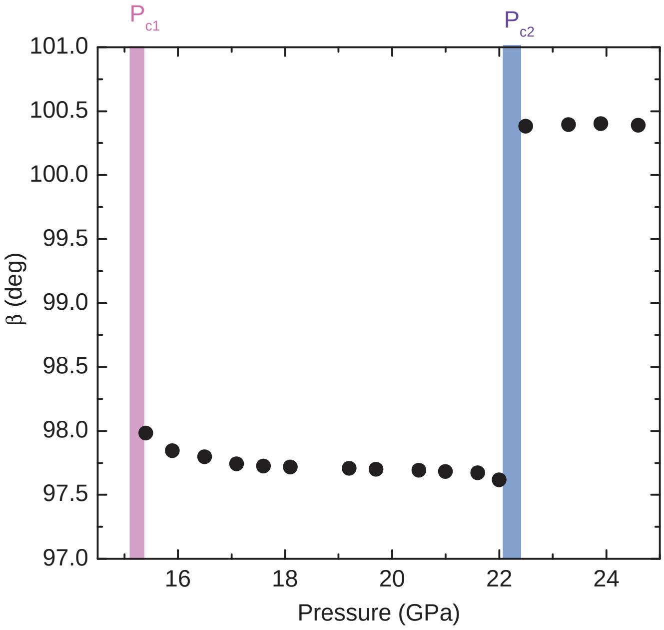

Figure 5.17: Angle β of the unit cell of the P2$_1$/m monoclinic crystal structure at room temperature as a function of pressure.

Another important finding observed with further pressure increasing above 22 GPa, is that all the lattice parameters of the monoclinic phase show an abrupt jump at P_{c2} with a sudden jump for the β angle to $\approx$ 100.4° (see Figures 5.15 and 5.17) indicating the appearance of a second structural phase transition at P_{c2}. This second phase transition is also assumed to consist of two phases: the orthorhombic phase (space group Pmmn) and the monoclinic phase (space group P2$_1$/m) and the superstructure $2a \times 2b \times c$. Within the region of the second phase transition ($P_{c2} >$ 22 GPa), the lattice parameters of both phases are hardly changed with increasing pressure up to 25 GPa. It must be mentioned here that Zhang et al.[143] predicted two phase transitions [143] where the second phase

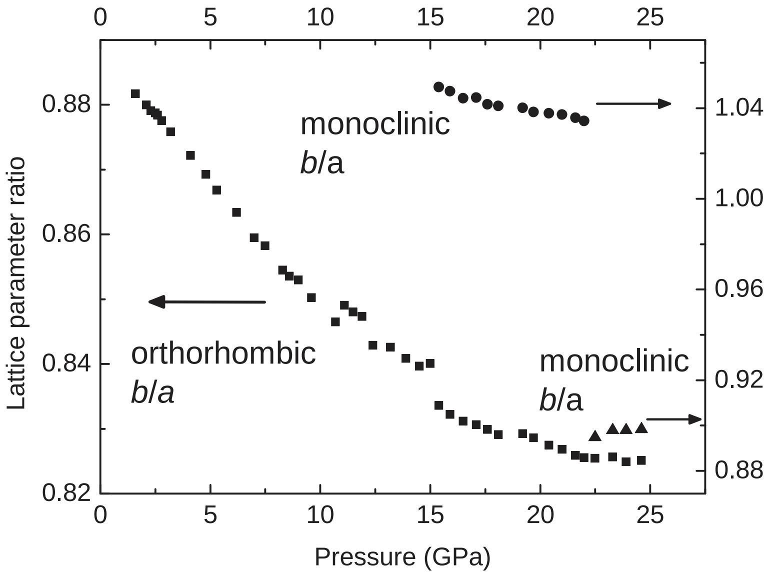

Figure 5.18: Lattice parameter ratio as a function of pressure: Square symbols refer to the ratio b/a for the orthorhombic phase (Pmmn) for the whole studied pressure range, circle symbols refer to the ratio b/a for the monoclinic phase ($P2_1/m$) for the pressure range $P_{c1} < P < P_{c2}$, triangle symbols refer to the ratio b/a for the monoclinic phase ($P2_1/m$) for the pressure range $P > P_{c2}$.

transition was expected to be an undimerized metallic state with orthorhombic (Pmmn) symmetry. Our data did not confirm this undimerized metallic state, since there is a mixture of both the orthorhombic and the monoclinic phases up to 25 [144].

Additionally, the dimensionality of the system was estimated from the pressure-dependent crystal structure data, in order to understand the mechanism behind the structural phase transitions. Figure 5.18 shows the ratio of b/a of the different crystal structure phases as a function of pressure. In the case of the orthorhombic phase, it can be observed that with increasing pressure the ratio b/a decreases, then it seems to be saturated above 23 GPa. Accordingly, this suggests that TiOCl tends to be more one-dimensional under pressure due to the larger compressibility of the lattice parameter in the b direction compared to the a direction (see Figure 5.15). This finding is in a good agrement with the earlier studies [70, 120]. At P_{c1} = 15.4 GPa, as mentioned before, the first structural phase transition indicates the appearance of a monoclinic phase which is energetically degenerate with the orthorhombic phase. If we look at the changes of the lattice parameters of the monoclinic phase (see Figure 5.15), it is found that the unit cell enlargement occurs along the b direction while along the a direction it shows a big shrinkage leading the b/a ratio to become close to *one* which means that the system is close to two-dimensional. This indicates that the both of the interchain interaction and the intrachain interaction are important, i.e., it appears from our result that the interchain and intrachain interactions are expected to play a major role for the determination of the electronic and magnetic properties of TiOCl in the pressure range $P_{c1} < P < P_{c2}$. Furthermore, as shown in Figure 5.15, at $P_{c2}\approx$ 22.6 GPa, where the two structures still exist, the unit cell of the monoclinic phase shows enlargement along the a direction and a shrinkage along the b direction leading to a decrease of the b/a ratio to 0.9, which means that the system is close to one-dimensional.

5.5 Transmittance measurements on TiOCl under high-pressure and at low-temperature

In this section, the pressure-dependent transmittance measurements at low temperatures of TiOCl in the mid-infrared frequency range (550-8000 cm^{-1}) will be presented and discussed. Our goal here is to study the temperature and pressure dependence of the crystal field splitting via the frequency of the orbital excitations, where the orbital excitation can be directly observed due to the lack of inversion symmetry on the Ti sites as mentioned in section 5.2.2.

5.5.1 Experiment for the low-temperature and high-pressure transmission measurements

In order to continue the previous work of our group, the pressure-dependent transmittance measurements were studied on single crystals of TiOCl in the mid-infrared frequency range (550-8000 cm^{-1}) at low temperatures for both polarization directions ($E\|a$, b). The Syassen-Holzapfel type diamond anvil cell was used for pressure generation. The measurements were carried out on a small piece of

TiOCl (about 90 μm×90 μm) cut from a single crystal with a thickness of ≈ 5 μm. The sample was then placed inside a small hole that is drilled in a stainless steel gasket. Finely ground CsI was chosen as quasi-hydrostatic pressure medium. The DAC is then mounted to a continuous-flow helium cryostat (Cryo Vac KONTI cryostat) via a suitable holder. The data were recorded for several pressure cycles between 0 and 22 GPa. For each pressure cycle, the measurements were carried out upon temperature decreasing where the transmittance spectra were measured at several temperature steps from 300 down to 50 K. The pressure inside the diamond anvil cell (DAC) was determined in situ by the ruby luminescence method. After warming up, the applied pressure has to be increased at room temperature. The measurements were carried out using a home-built infrared microscope coupled to the FTIR spectrometer under vacuum, in order to avoid absorption lines of H_2O and CO_2 molecules. All details about the measurements procedure are explained in the experimental chapter.

5.5.2 Results and discussion

The transmittance spectra of TiOCl were measured for the two polarization directions which are laying parallel to the buckled Ti-O bilayer ($E\|a$, $E\|b$). At the lowest pressure, an absorption feature is observed in the polarization direction ($E\|a$) which is symmetric and has a Gaussian-shaped dip. By fitting this absorption feature with a Gaussian function, it was found that it lies at around (0.66 eV). This absorption dip is identified as an orbital excitation due to the excitation between the splitting crystal field within the Ti 3d states, hence the degeneracy of the Ti 3d energy level is lifted by the crystal field splitting as mentioned in section 5.2 (see Figure 5.2). This observation is in a good agreement with the previous studies [128–130, 140].

Here we study the pressure effects on the optical properties of TiOCl during cooling down. The pressure-dependant transmittance measurements were carried out in the mid-infrared range as a function of temperature. For illustration, Figure 5.19 shows the transmittance spectra of the two polarization directions for the temperatures at around (295 and 50 K) for different selected pressures between 0 and 22 GPa. The transmission spectra at around (250, 200, 180, 150, and 100 K)

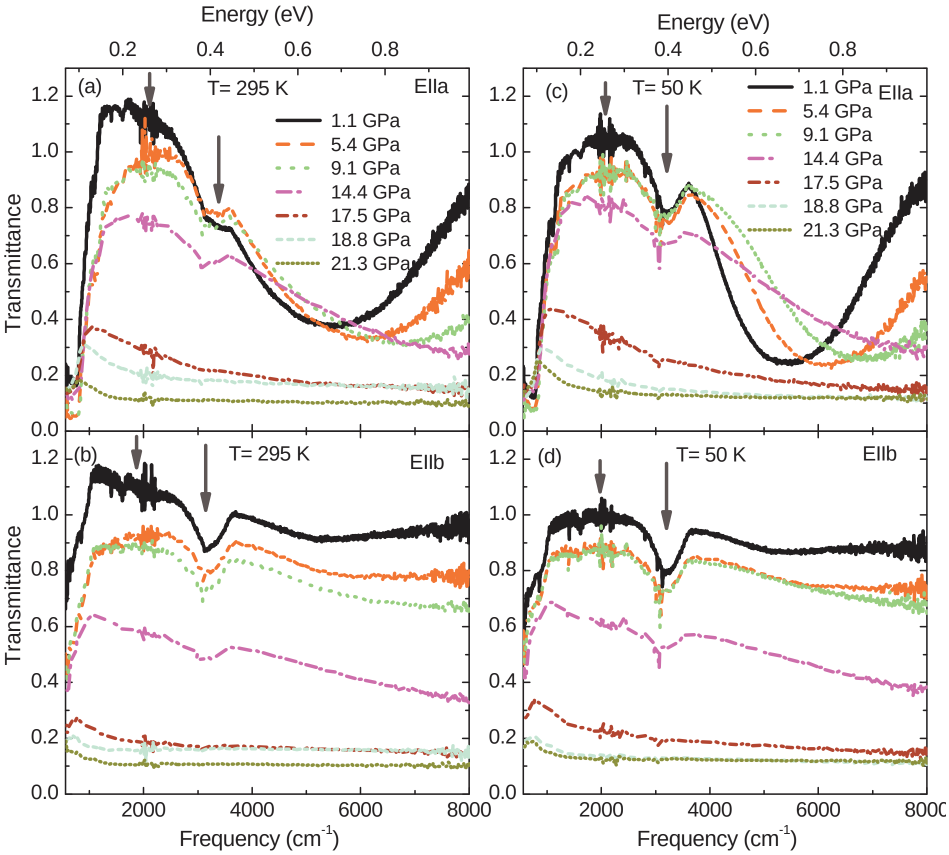

Figure 5.19: Transmittance spectra of TiOCl for various pressures for the polarization directions $\mathbf{E}\|a$, $\mathbf{E}\|b$ at around 295 and 50 K from left to right. Arrows refer to artifacts due to diamond absorption.

for different selected pressures between (0 and 22 GPa) are presented in Appendix A. The transmittance data around 1800 cm^{-1} and 3000 cm^{-1} are dominated by the multi-phonon absorption of the diamond anvils (explained in detail in the experimental chapter). The changes which happened in the transmittance spectra due to increasing the pressure at around 50 K will be clarified as an example, where the sample is in the spin-Peierls state at ambient pressure. At all pressures, the transmittance spectra are suppressed by phonon absorption below 0.1 eV for both polarization directions ($E\|a$, $E\|b$), in addition to an orbital excitation in the polarization direction $E\|a$ at around 0.66 eV, consistent with earlier optical absorption studies [128, 129](see Figure 5.4). Upon increasing the pressure, the overall transmittance spectra decrease for both polarization directions, while the orbital excitation becomes broader and slightly shifts to higher frequencies. This could be due to the increase of both of the crystal field strength and the octahedral distortion. Above 14 GPa, a clear suppression of the overall transmittance spectra for both polarization directions is observed which might be attributed to the filling of the Mott-Hubbard gap with additional states. This leads to the appearance of new excitations in the infrared frequency range which could be an evidence of a possible appearance of a metallic phase at high pressures. This observation is in accordance with our structural phase transition finding which was discussed in section 5.4 and in the previous pressure studies on TiOCl at room temperature [70, 130, 140, 144], where a structural phase transition is observed approximately at the same pressure. Additionally, for the overall transmittance spectra between the measured pressure cycles, from ambient pressure up to 9.1 GPa, very small variations are noticed for $E\|a$ during cooling down, where the frequency position of the orbital excitation seems to be slightly decreased with decreasing the temperature (see Figure 5.20). For the pressures above 9.1 GPa, the absorption peak becomes broader and starts to lose its symmetric shape (Gaussian shape) as sown in Figure 5.21.

In order to distinguish between the changes on the crystal field splitting induced by pressure at low temperature, our transmittance spectra were fitted by using the Gaussian function. Figure 5.22 illustrates the obtained frequency positions of the orbital excitation as a function of temperature at (1.1, 5.4, and 9.1) based on the Gaussian fitting. At a fixed temperature, for example at 100 K, a significant shift of the orbital excitation ($E\|$a) is observed, where it shifts linearly to higher frequency as the pressure increases. This observed shift can be explained as follows: Applying external pressure leads to a monotonically increasing strength of the crystal field related to the decreasing volume of the TiO_4Cl_2 octahedra. It could also induce a change in the octahedra distortion which may cause this shift [70]. While at a fixed pressure, let us take for example the spectra at around 1.1 GPa: The orbital excitation shows a very small shift to higher frequencies during cooling down from room temperature to 150 K, then below 100 K the orbital excitation seems to be hardly shifted. This can be interpreted as follows: For the temperature range 295-150 K, the changes in

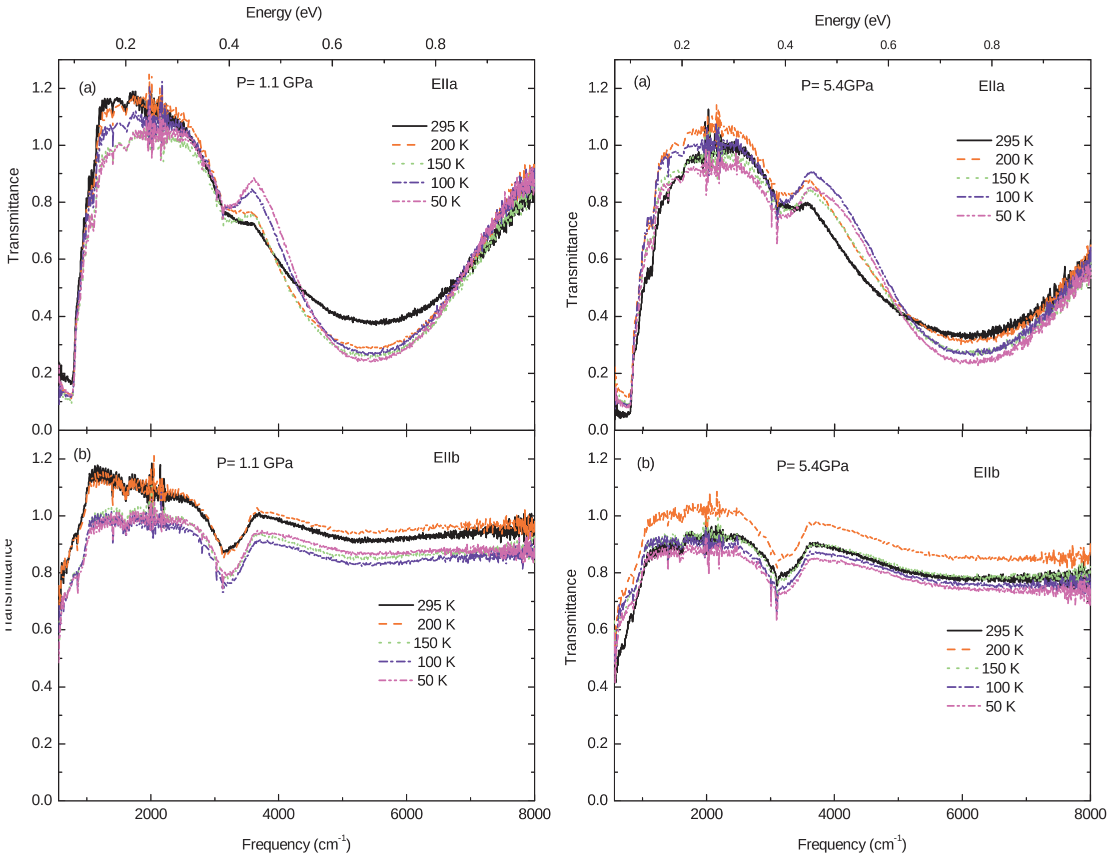

Figure 5.20: Transmittance spectra of TiOCl for various chosen temperatures for the polarization directions $E\|a$, $E\|b$ at around 1.1 and 5.4 GPa.

the thermal contraction of the lattice during cooling down are supposed to have an effect on the TiO_4Cl_2 octahedra volume by decreasing it with decreasing the temperature and hence the crystal field strength becomes stronger, leading to the observed small change in the orbital excitation. For the temperatures below 100 K, where it is already the temperature region of the two consecutive phase transitions which are characteristic for TiOCl (T_{c2}=91 K and T_{c1}=67 K), one expects that orbital fluctuations are strongly suppressed. Accordingly, the changes of both of the strength of the crystal field and the octahedral distortion will be slight. Interestingly, this finding is in agreement with the previous spectroscopy and electron spin resonance studies on both TiOCl and TiOBr [70, 128, 129, 146] where only slight changes were observed in the absorption features during cooling

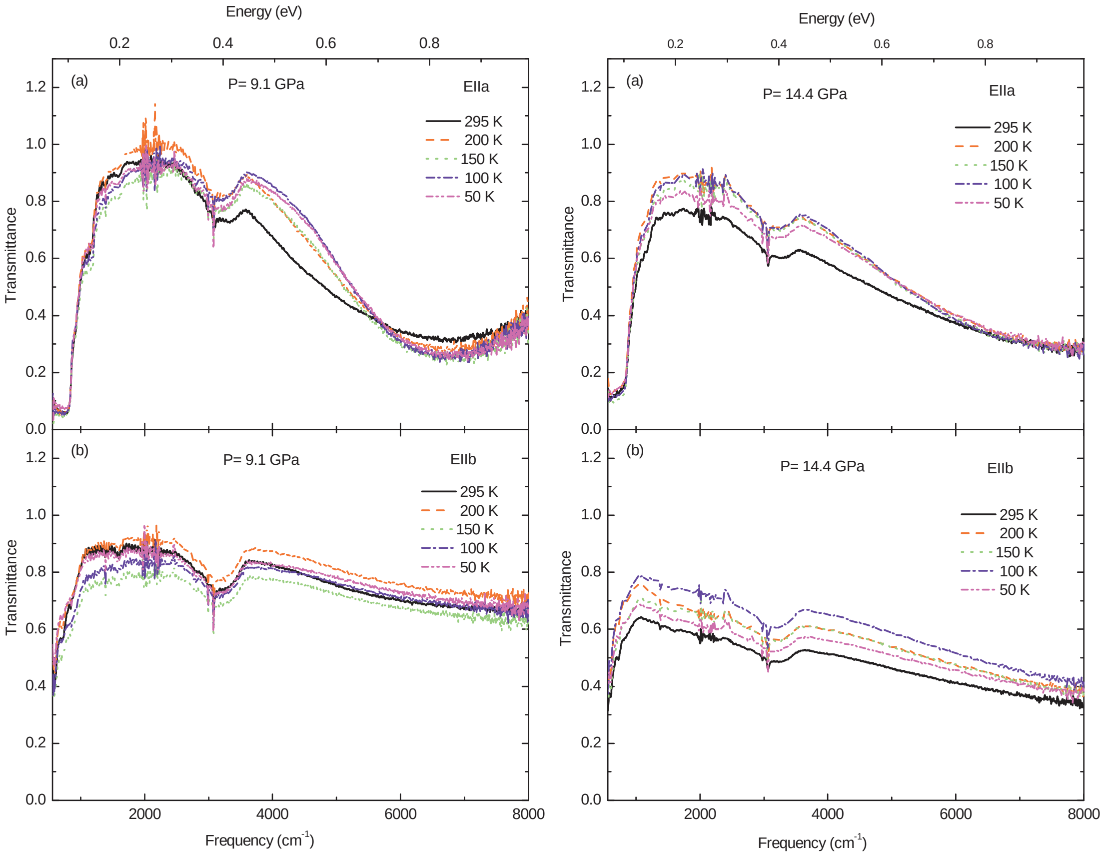

Figure 5.21: Transmittance spectra of TiOCl for various chosen temperatures for the polarization directions $\mathbf{E}\|a$, $\mathbf{E}\|b$ at around 9.1 and 14.4 GPa.

down from (100 to 4 K), which were attributed to the suppression of the orbital fluctuations.

5.6 Reflectance measurements on TiOCl under high-pressure and at low-temperature

In this part of the work, the study of the electronic properties of TiOCl via the reflectance measurements as a function of low temperature and high pressure, is presented. Here, the possibility of a metallic state for TiOCl will be discussed through the additional information obtained from the changes induced by pressure

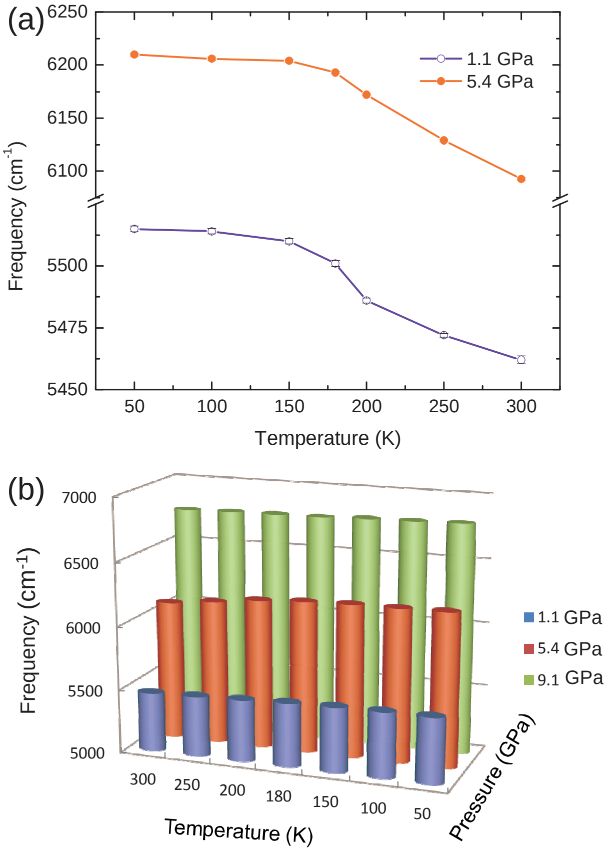

Figure 5.22: The frequency positions of the orbital excitation, due to the crystal field splitting, as a function of temperature and pressure obtained from the fitting by using Gaussian function.

in the reflectance spectrum at low temperatures and hence its corresponding optical response in the mid-infrared frequency range (550- 8000 cm^{-1}).

5.6.1 Low-temperature and high-pressure reflectance measurements

The pressure-dependent reflectance measurements up to 21.3 GPa at temperatures from 300 K down to 50 K in the mid-infrared range were studied for TiOCl. Because of the difficulty to carry out the polarization-dependent reflectance measurements under high pressure and low temperature, the unpolarized reflectance measurements were carried out. At this point, it was assumed that the reflectance spectrum will be an average of both polarization directions ($\mathbf{E}\|a$, b). The measurements were carried out on a small piece of TiOCl (about 100 μm×100 μm) cut from a single crystal with a thickness of ≈ 5 μm. The Syassen-Holzapfel type diamond anvil cell was used for pressure generation. For the reference measurements, a silver layer was evaporated on the pre-pressed area of the stainless steel gasket and used as a reference. The sample is then placed inside the gasket hole. Finely ground CsI is used as a quasi-hydrostatic pressure medium.

5.6.2 Results and discussion

As mentioned in section 5.4, the changes in the crystal structure might influence the electronic properties and hence the characteristics of the material, e.g., changing the frequency position and the intensity of the MIR band. Furthermore, in order to have a complete description of the strongly correlated system phase diagram, not only the U/t ratio has to be considered but also both the temperature and the degree of magnetic frustration (simulated by the ratio of the next-nearest-neighbour hopping amplitude to the nearest neighbour one) have to be added [10]. Accordingly, the solution of the Hubbard model by using the DMFT at finite temperature [13–15] predicted that below a critical temperature T_{coh} which is close to the first-order Mott transition temperature, the MIT transition is expected to take place (see section 2.1.3). At this transition a transfer of spectral weight to the low-frequency end of the optical conductivity spectrum is predicted. This indicates the appearance of a quasiparticle peak around the Fermi energy, involving coherent excitations, as a result the Fermi-liquid description will be used. Therefore, the optical conductivity spectrum is expected to consist of the following contributions: A Drude term, a mid-infrared absorption band, and a high-frequency band (see Figure 2.7(b)). These findings motivated us to search for a proof of the existence of the Drude responce, i.e., the signature of coherent transport, in the optical conductivity spectra of TiOCl.

The pressure-dependent reflectance measurements were carried out in the mid-infrared range as a function of temperature. The upper panels of Figures 5.23 and 5.24 show the measured reflectance spectra for the pressure cycles at around

12, 14, 16.5, and 19 GPa for various selected temperatures. The frequency region around 2000 cm^{-1} is cut out from the reflectance spectra because it is dominated by multi-phonon absorption of the diamond anvils (explained in detail in the experimental chapter). A growth in the overall reflectance spectra starts to be observed above 14 GPa. Nevertheless, for each pressure cycle a slight change was observed in the overall reflectance spectra during cooling down to 50 K.

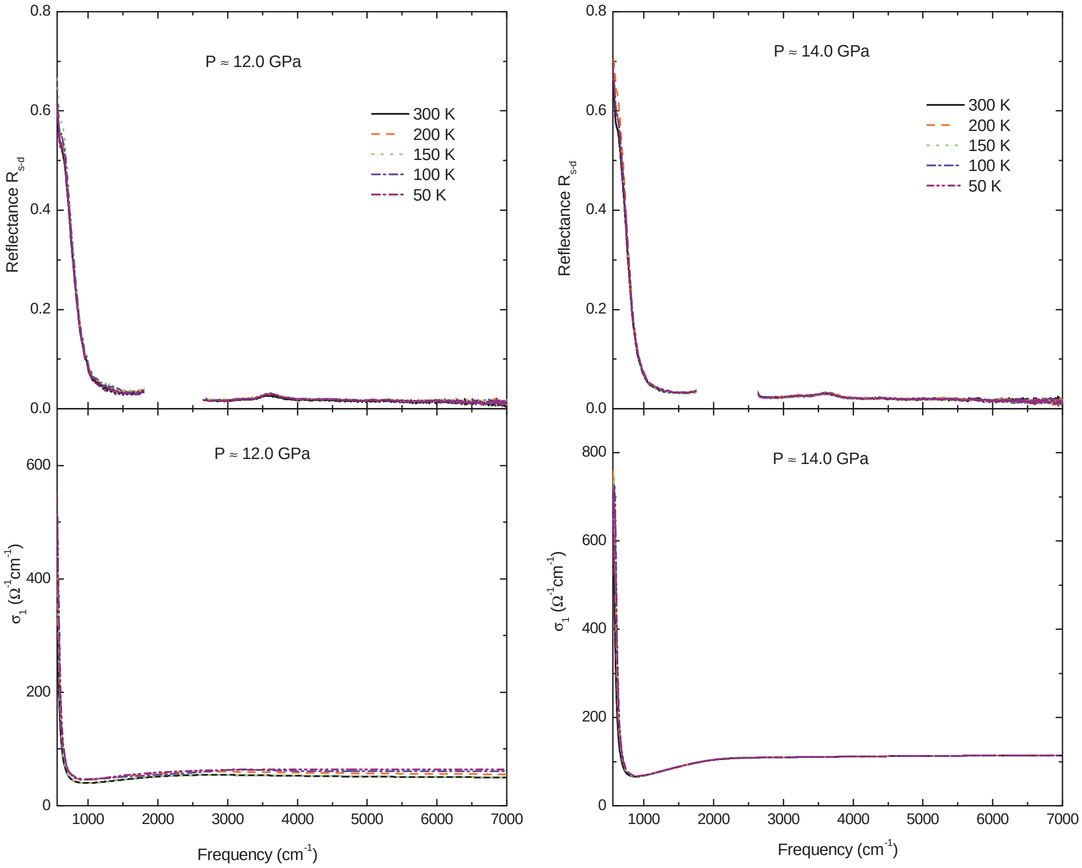

Figure 5.23: Reflectance spectra of TiOCl as a function of temperatures at around 12 and 14 GPa. The lower graph shows the corresponding real part of the optical conductivity $\sigma_1(\omega)$ obtained by fitting the reflectance data with the Drude-Lorentz model.

Now let us discuss the observed changes in the reflectance spectra for different chosen pressures at a fixed temperature. For illustration, the changes in the reflectance spectrum at 300 K will be spoken about for several selected pressures

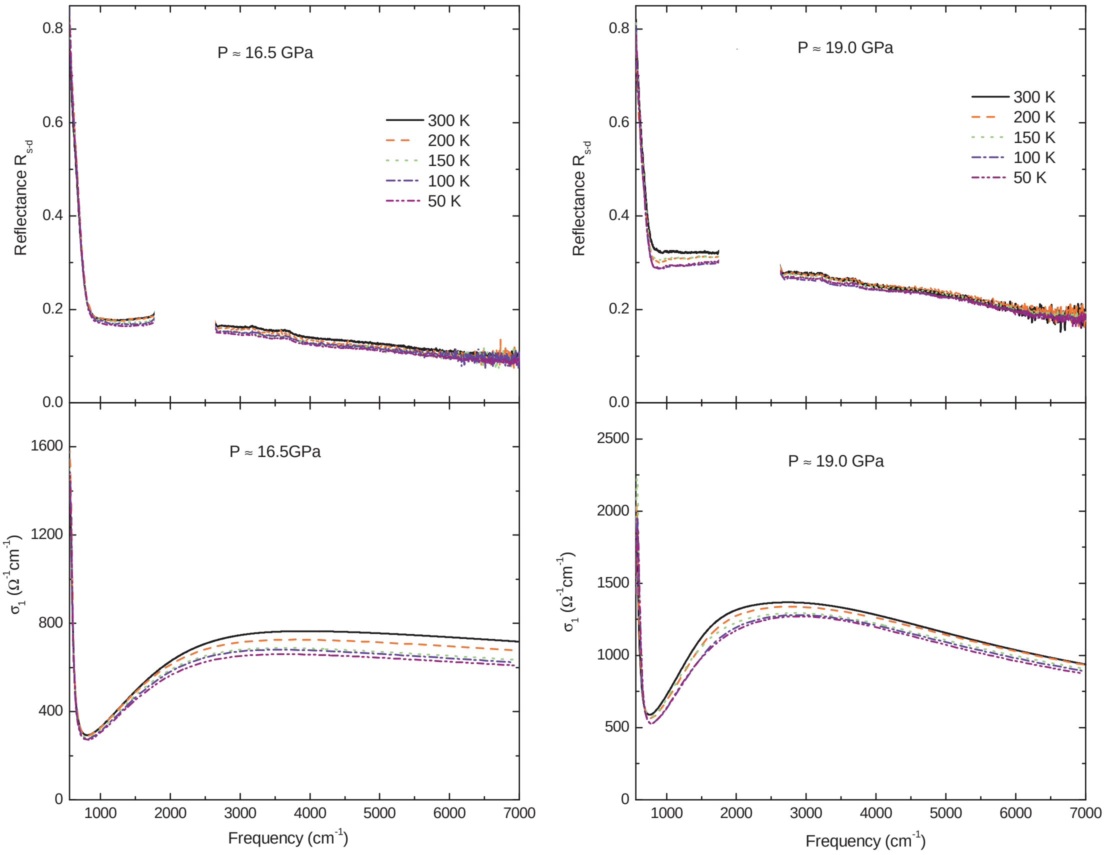

Figure 5.24: Reflectance spectra of TiOCl as a function of temperatures at around 16.5 and 19 GPa. The lower graph shows the corresponding real part of the optical conductivity $\sigma_1(\omega)$ obtained by fitting the reflectance data with the Drude-Lorentz model.

between 12 - 21.5 GPa as an example. Below 0.1 eV, the reflectance spectra are affected by phonon excitations consistent with earlier studies [70, 132, 140]. Furthermore, at the lowest two pressures (12 and 14 GPa), the overall reflectance spectra are approximately constant, revealing the insulating behavior of the material as expected from the previous studies [70, 140]. With increasing pressure above 14 GPa, a sudden growth in the overall reflectance spectra is observed. This growth seems to increase monotonically with increasing the pressure up to 21.5 GPa (see upper panel of Figure 5.25 at 300 K). Hence, as mentioned in section 5.5, a suppression of the transmittance spectra is observed at the same pressure, which suggests the occurrence of new excitations in the infrared frequency range. This sudden increase will be interpreted in terms of the development of a plasma edge.

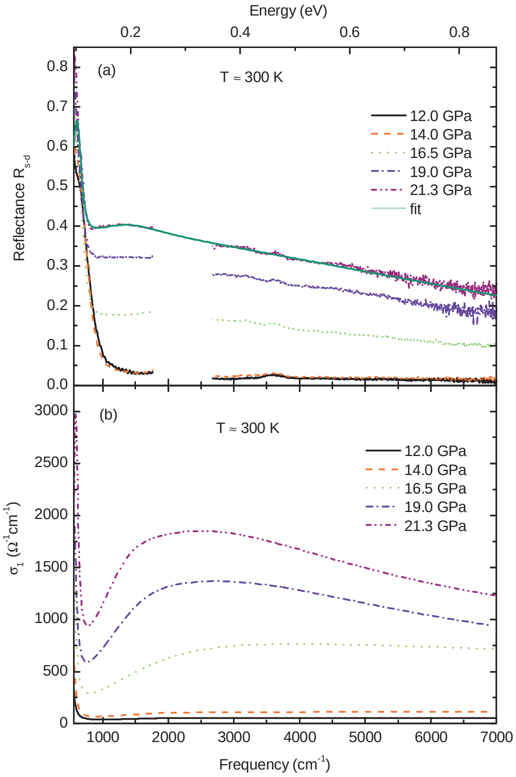

Figure 5.25: Reflectance spectra of TiOCl for several pressures at around 300 K. The lower graph shows the corresponding real part of the optical conductivity $\sigma_1(\omega)$ obtained by fitting the reflectance data with the Drude-Lorentz model.

In order to get more information about these expected excitations and the observed changes in the optical response, which is induced by pressure and temperature, our reflectance spectra were fitted by using the Drude-Lorentz model combined with the Fresnel equation for the normal-incidence reflectivity (explained in detail in the experimental chapter). Furthermore, here it was assumed that the changes of ϵ_∞ at low temperatures are not that significant (temperature independent) compared to its changes under pressure. ϵ_∞ as a function of pressure

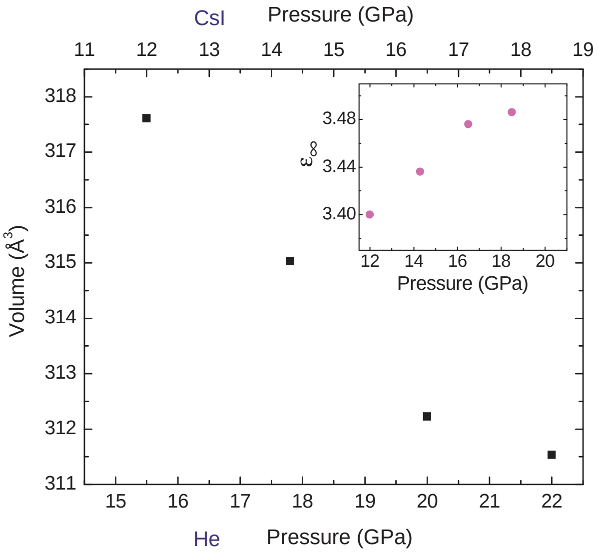

Figure 5.26: The unit cell volume of TiOCl as a function of pressure for both He and CsI as transmission medium. The inset represents the high-frequency permittivity $\epsilon_\infty(P)$ as a function of pressure, calculated according to the Clausius-Mossotti relation [Eqn.(5.2)]

was derived from the Clausius-Mossotti relation [147]

$$\frac{\epsilon_\infty(P)-1}{\epsilon_\infty(P)+2}=\frac{\tilde{\alpha}}{3\epsilon_0 V(P)}, \tag{5.2}$$

where $V(P)$ is the unit cell volume as a function of pressure, ϵ_0 is the permittivity of free space, and $\tilde{\alpha}$ is the average atomic polarizability of the unit cell. By assuming that $\epsilon_\infty \approx 3.4$ at 12 GPa. Then by using the corresponding value of the unit cell volume at 12 GPa obtained from our XRD data calculation, taking into account the difference between the transmission medium as shown in Ref.[70], the value of $\tilde{\alpha} \approx 37.49 \times 10^{-40}$ was obtained. By assuming that the value of $\tilde{\alpha}$ is pressure independent and by pluging in this value in Equation 5.2, the high-frequency permittivity $\epsilon_\infty(P)$ is obtained as a function of pressure (see the inset of Figure 5.26).

Additionally, in order to describe well the various excitations in the reflectance spectra starting from ambient pressure up to 14 GPa, the fitting parameters have to consist of a sum of Lorentz oscillators: one Lorentz oscillator for describing the phonon line below 1000 cm^{-1}, two Lorentz oscillators for describing the spectra range up to 8000 cm^{-1} and one Lorentz oscillator for the extrapolation. Hence, as mentioned in section 2.1, the solution of the Hubbard Model by using the DMFT predicted that the appearance of the mid-infrared band is concurrent with the appearance of the coherent excitation. Therefore, above 14 GPa, due to the appearance of the mid-infrared band, a sum of Lorentz oscillators for fitting our reflectance spectra was not enough for describing the frequency range below 1000 cm^{-1} . The fitting parameters of the reflectance spectra for the pressures above 14 GPa consist of a Drude term and four Lorentz oscillators. Here, we have to mentioned that the sample-diamond-interface was taken into account for fitting the reflectance spectra. The multiphonon diamond absorption area (1800-2760 cm^{-1}) is extrapolated via the Drude-Lorentz fit. An example of the fitting of the reflectance spectrum around 21.3 GPa and at 300 K is shown in the upper left panel of Figure 5.25. Accordingly, the real part of the optical conductivity spectra $\sigma_1(\omega)$ will be derived from Eqn. 3.38.

The corresponding real part of the optical conductivity spectra obtained from the fitting of the reflectance spectra by using the Drude-Lorentz model are shown in the lower panels of Figures 5.23- 5.24. The most interesting feature in the optical conductivity spectrum is the occurrence of the mid-infrared absorption band above 14 GPa. With increasing pressure, the intensity of the mid-infrared band increases and it seems to be shifted slightly to lower frequencies (see the lower panel of Figure 5.25). These observations are consistent with our XRD measurements, where applying external pressure leads to the appearance of structural phase transitions, which might influence the electronic properties by changing the electronic bandwidth near the Fermi level which appears also in the suppression of the transmittance spectra and growth of the mid-infrared band in the reflectance spectra above 14 GPa. Accordingly, an insulator-to-metal transition is expected above this pressure compatible with the previous reports [70, 140].

Furthermore, by comparing the optical conductivity spectra at a certain pressure during cooling down, for example at 19 GPa for several chosen temperatures between 300 and 50 K, no significant changes are observed in the overall optical conductivity spectra during cooling down, but only small decrease of the spectral weight of the mid-infrared absorption bands are noticed (see the lower panel of Figure 5.24). These slight changes confirm that the cooling down does not

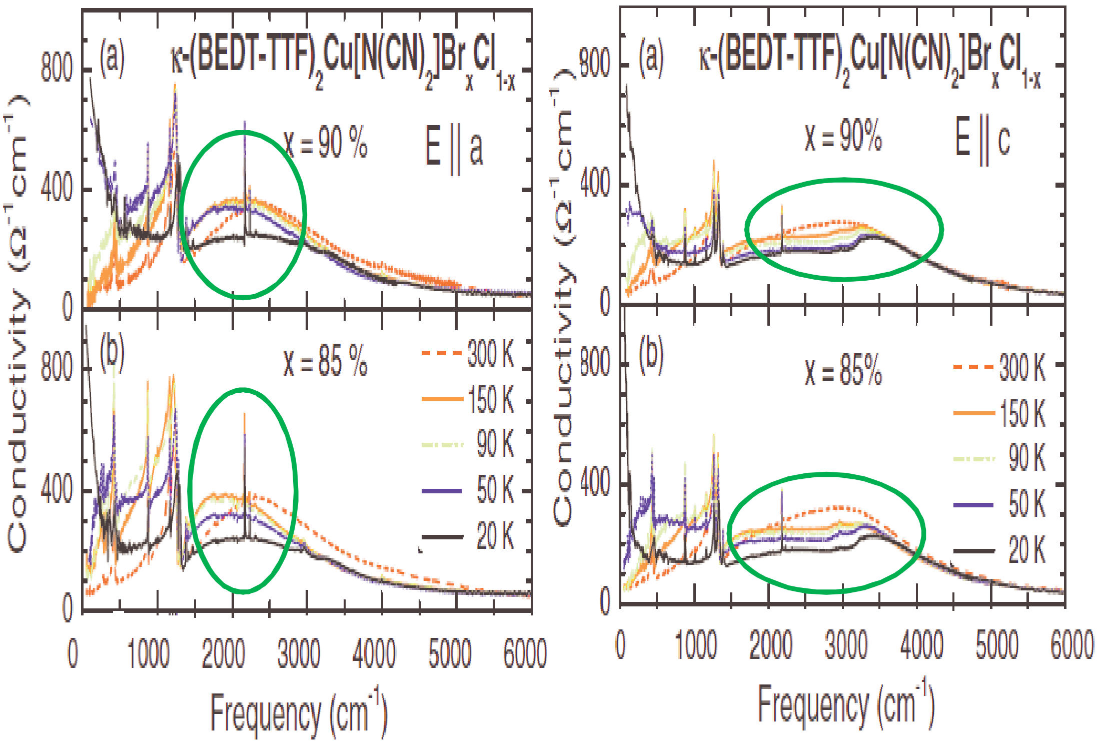

Figure 5.27: Optical conductivity spectra ($\mathbf{E}\|a$) and ($\mathbf{E}\|c$) for [κ^{-}(BEDT-TTF)$_2$Cu[N(CN)$_2$]Br$_x$Cl$_{1-x}$] salts for Br contents of $x=$ 0.85 and 0.9 measured at various temperatures: T=300, 150, 90, 50, and 20 K, obtained by a Kramers-Kronig analysis [17]. The green circles show the observed changes in the mid-infrared range during cooling down.

strongly affect the growth of the overall optical conductivity spectra through increasing the pressure, which is in agreement with the earlier reports at ambient pressure [132, 138]. Interestingly, the observed changes in the mid-infrared absorption band of the [κ^{-}(BEDT-TTF)$_2$Cu[N(CN)$_2$]Br$_x$Cl$_{1-x}$] salts during cooling down at 20 K for Br contents of $x=$ 0.85 and 0.9 are similar to our observation [15, 17]. For example at $x=$ 0.85 , only small changes in the mid-infrared frequency range were observed, where the mid-infrared absorption band shows a slight decrease of its spectral weight during cooling down (see Figure 5.27). The major changes were observed in the far-infrared range: here the coherent excitation appears. Unfortunately, it is very difficult to carry out the reflectance measurements in this frequency range for the case of the Mott-insulator TiOCl [1].

Based on our data, it cannot be confirmed that the observed growth of the optical conductivity in the mid-infrared range with increasing pressure is related to the presence of a Drude-term (coherent excitation) which could be due to the appearance of a quasiparticle peak around the Fermi level. As a final remark, in order to interpret the behavior of the transmission and reflectance spectra of TiOCl under high pressure and low temperature, the dc transport measurements on a single crystal of TiOCl along the *ab* plane and their dependence on pressure are required. However, the contacts quality are still an important open issue.

5.6.3 Pressure-temperature phase diagram of TiOCl

Finally, the pressure-temperature phase diagram of TiOCl will be proposed depending on our data and the experimental findings of Refs. [70, 120, 130, 140, 142, 144, 145]. Figure 5.28 shows the pressure-temperature phase diagram of TiOCl for pressures up to 25 GPa and temperatures from 300 K to 0 K. Starting from ambient conditions, TiOCl has an orthorhombic crystal structure with space group (Pmmn). During cooling down at ambient pressure, TiOCl goes through a second order phase transition at T_{c2}≈91 K to an incommensurately modulated structure. At T_{c1}≈67 K, it undergoes a first order phase transition to a dimerized spin-Peierls phase with a monoclinic crystal structure with space group P2_1/m and a-axis unique with monoclinic angle $\alpha \approx 90^0$ [135, 148, 149]. Furthermore, it was predicted that the spin-Peierls temperature will increase with increasing the pressure and reach room temperature above 10 GPa [120]. At T = 6 K it was found that the spin-Peierls phase can be driven into a charge-density wave (CDW) phase at high pressure with dimerization along the *a* axis with a modulation factor $[q=(1\text{-}\epsilon)/2]$ and discommensuration ϵ=0.02 [145]. From the present data, a first structural phase transition is observed at $P_{c1} \approx$ 14 GPa leading to the coexistence of both the space groups Pmmn and P2_1/m . The monoclinic phase at P_{c1} has a superstructure $2a \times 2b \times c$ and a b-axis unique with the monoclinic angle $\beta \approx 98°$. Furthermore, the dimensionality of the TiOCl tends to be

---

[1] In the case of TiOCl the reflectance spectra start to grow above 14 GPa, therefore in order to measure up to 22 GPa, the size of the gasket hole has to be about 120 μm. Accordingly, the sample size will be small for the far-infrared range measurements.

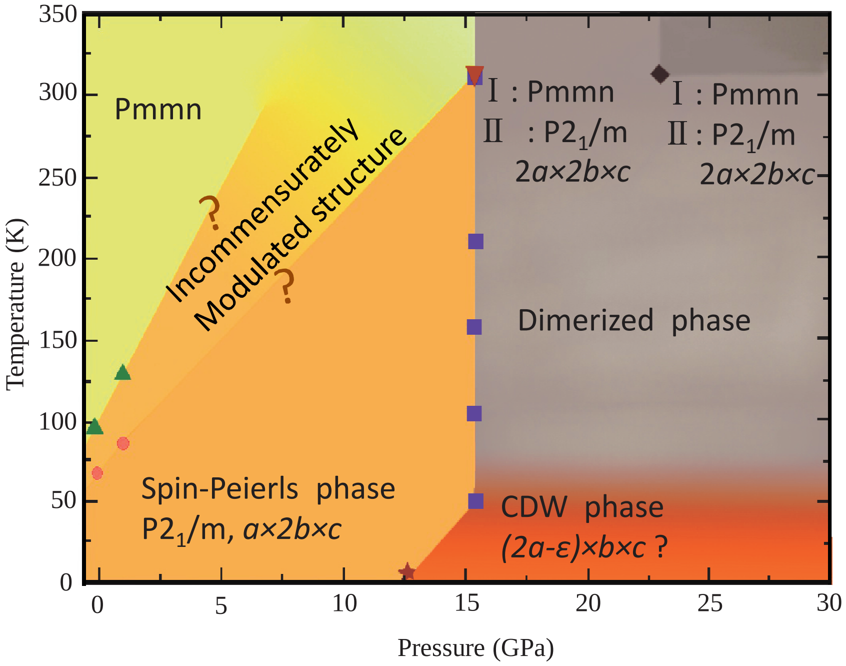

Figure 5.28: The proposed pressure-temperature phase diagram of TiOCl for pressures up to 25 GPa and temperatures from 300 K to 0 K based on the experimental findings of Refs. [70, 120, 130, 140, 142, 144, 145] and the present work. The filled up triangles and filled circles crossposting to the incommensurate and the Spin-Peierls phase at ambient pressure [120, 135, 148, 149]. The filled star crossposting to the Peierls phase at T=6 K with $2a\times 2b\times c$ supperstructure [145]. The filled down triangle and the filled diamond crossposting to the two structural phase transitions which were obtained from our data [144]. Finally, the filled squares refer to the present and the earlier infrared data [70, 140]

more two-dimensional for the monoclinic structure. At this critical pressure, a suppression in the transmittance spectra is observed. This is combined with the occurrence of new excitations which appear in the optical conductivity spectra, accordingly a gap closure could be predicted. During cooling down to 50 K, no significant changes are observed in the optical conductivity at this pressure. At P_{c2} ≈22 GPa a second structural phase transition is observed at room temperature leading to the coexistence of both space groups (Pmmn and P2$_1$/m). The monoclinic phase at P_{c2} has a superstructure $2a\times 2b\times c$ and b-axis unique with monoclinic angle $\beta \approx 100.4^\circ$. Additionally, the dimensionality of the system will tend to be more one-dimensional for the monoclinic structure.

5.7 Summary

According to our XRD measurements under pressure on TiOCl at room temperature, two structural phase transitions were observed at P_{c1} ≈15 GPa and P_{c2} ≈22 GPa. Above P_{c1} two phases were observed (orthorhombic phase and monoclinic phase) where a dimerization along the a and b was observed for the monoclinic phase. At P_{c2} the two phases still exist, but all the lattice parameters of the monoclinic phase showed pronounced anomalies. The above findings prove that the pressure application induces significant structural modifications on TiOCl. In order to identify the effects of these crystal structure modifications on the electronic properties, the optical transmittance and reflectance spectra of TiOCl were studied at temperatures from 300 K down to 50 K and for pressures up to 22 GPa in the mid-infrared frequency range. Suppression of the overall transmission spectra was observed above the critical pressure $P\approx$ 14 GPa. Moreover, a linear shift of the orbital excitation to higher frequencies with increasing pressure at certain temperature occurs, while it hardly shifts to higher frequencies during cooling down to 50 K at a fixed pressure. Above the critical pressure P_{c1}, a huge growth of the spectral weight was observed in the optical conductivity spectrum. This can be attributed to the closure of the Mott-Hubbard gap under external pressure where additional excitations are expected to appear which will be described by the Drude term in addition to the mid-infrared absorption band. At 50 K, no significant changes with increasing the pressure were observed in the optical conductivity spectra compared to the room temperature spectra. Electrical transport measurements on a single crystal of TiOCl are strongly recommended to explain our findings and the possibility of a metal-to-insulator transition in TiOCl.

Chapter 6

Conclusions

Within the present work two classes of transition-metal oxides, namely: Fe_3O_4 and TiOCl were investigated. The main experimental techniques used are: optical spectroscopy and x-ray powder diffraction (XRD).

Magnetite belongs to the strongly electronically correlated systems. It shows many interesting physical properties, including the Verwey transition at T_V=122 K. Within the present work, our study on magnetite was divided into two parts. In the first part, the optical properties under pressure were studied at room temperature from 200 cm^{-1} to 18000 cm^{-1}. The main contributions of the optical conductivity spectra in the studied frequency range were: a Drude term, two sharp phonon modes, a far-infrared band at around 600 cm^{-1}, and a pronounced mid-infrared absorption band (polaronic band) around 5000 cm^{-1}. With increasing pressure both absorption bands showed a red shift, while the phonon modes shifted linearly to higher frequencies. One of our goal was to confirm the polaronic nature of the observed mid-infrared band via several theoretical models. The shape of the mid-infrared absorption band was described well by using the SP model in the limit ($s \ll D$). Additionally, the fitting of our dc transport data at low temperature showed that the small polaron regime is expected to dominate at low temperature. Accordingly, the polaronic coupling strength in magnetite at room temperature could be classified rather as intermediate. This was confirmed by the appearance of a far-infrared band in the optical conductivity spectrum at room temperature. Furthermore, we checked the changes in the spectral features at around 6 GPa, where earlier pressure studies observed a crossover transition around this pressure. Several contributions of the optical conductivity spectra (saturation of the plasma frequency and σ_{dc} of the Drude term, saturation in the SW of the observed far-infrared band, and an abrupt increase of the linear pressure coefficient for the lower energy phonon mode), were observed around 6 GPa. These changes could be due to minor alterations of the charge distribution among the different Fe-sites.

In the second part, the pressure-dependance of the electronic and vibrational properties of magnetite were studied up to 10 GPa at temperatures from 300 K down to 10 K by far-infrared reflectance measurements [116]. It was found that the Verwey transition manifests itself by remarkable changes, namely:

- The overall reflectance spectra showed a huge decrease followed by a saturation of their down-shift at a critical temperature.
- The splitting of the phonon modes beside the activation of additional phonon modes is due to the lowering of the crystal symmetry, where phonon modes reach their maximum number at a critical temperature.

This critical temperature sets the lower bound for the Verwey transition temperature. Based on these optical results, a pressure-temperature phase diagram for magnetite was proposed. It shows the "bad metal" and the insulating phases. From our data, the sharp drop of T_v to zero and the occurrence of the metallization of magnetite above 8 GPa were ruled out.

TiOCl is a low-dimensional Mott-Hubbard insulator. Recently, the application of pressure on this compound revealed strong changes in its electronic and structural properties. Based on these results, the possibility of a pressure induced insulator-to-metal transition was suggested. Within the present work, our study on TiOCl was divided into two parts. In the first part, the crystal structure of TiOCl was studied up to 25 GPa at room temperature by XRD measurements. Two structural phase transitions were observed at P_{c1} ≈15 GPa and P_{c2} ≈22 GPa. Above P_{c1} two phases were seen (orthorhombic phase and monoclinic phase) where a dimerization along the a and b is observed for the monoclinic phase. At P_{c2} the two phases still existed, but all the lattice parameters of the monoclinic phase showed pronounced anomalies. The above findings prove that the pressure application induces significant structural modifications on TiOCl.

In the second part, in order to identify the effects of these crystal structure modifications on the electronic properties, the optical transmittance and reflectance spectra of TiOCl were studied at temperatures between 300 K and 50 K and for pressures up to 22 GPa in the mid-infrared frequency range. Suppression of the overall transmission spectra was observed above the critical pressure $P \approx$ 14 GPa. Moreover, a linear shift of the orbital excitation to higher frequencies with increasing pressure at a certain temperature occurred, while it hardly shifted to higher frequencies during cooling down to 50 K at a fixed pressure. Above the critical pressure P_{c1}, a huge growth of the spectral weight was observed in the optical conductivity spectrum. This can be attributed to the closure of the Mott-Hubbard gap under external pressure where additional excitations are expected to appear which will be described by the Drude term in addition to the mid-infrared absorption band. At 50 K, no significant changes with increasing the pressure were observed in the optical conductivity spectra compared to the room temperature spectra. Electrical transport measurements on a single crystal of TiOCl are strongly recommended to explain our findings and the possibility of a metal-to-insulator transition in TiOCl.

Appendix A

Transmittance spectra of TiOCl of the two polarization directions for temperatures at around (250 and 100 K) for different selected pressures between 0 and 22 GPa.

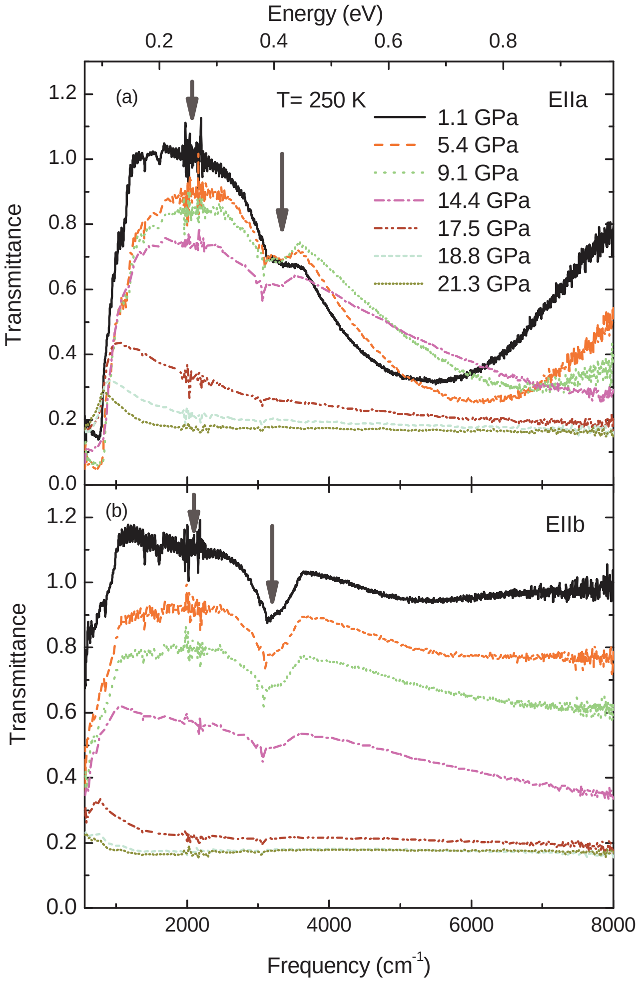

Figure 1: Transmittance spectra of TiOCl for various pressures for the polarization directions $E \| a$, $E \| b$ at around 250 K. Arrows refer to artifacts due to diamond absorption.

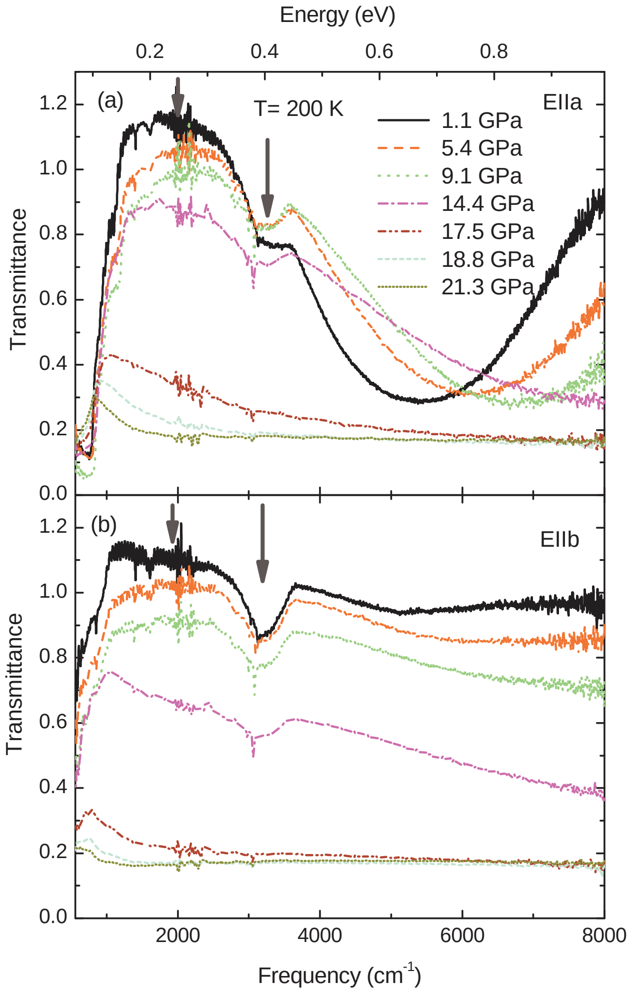

Figure 2: Transmittance spectra of TiOCl for various pressures for the polarization directions $E\|a$, $E\|b$ at around 200 K. Arrows refer to artifacts due to diamond absorption.

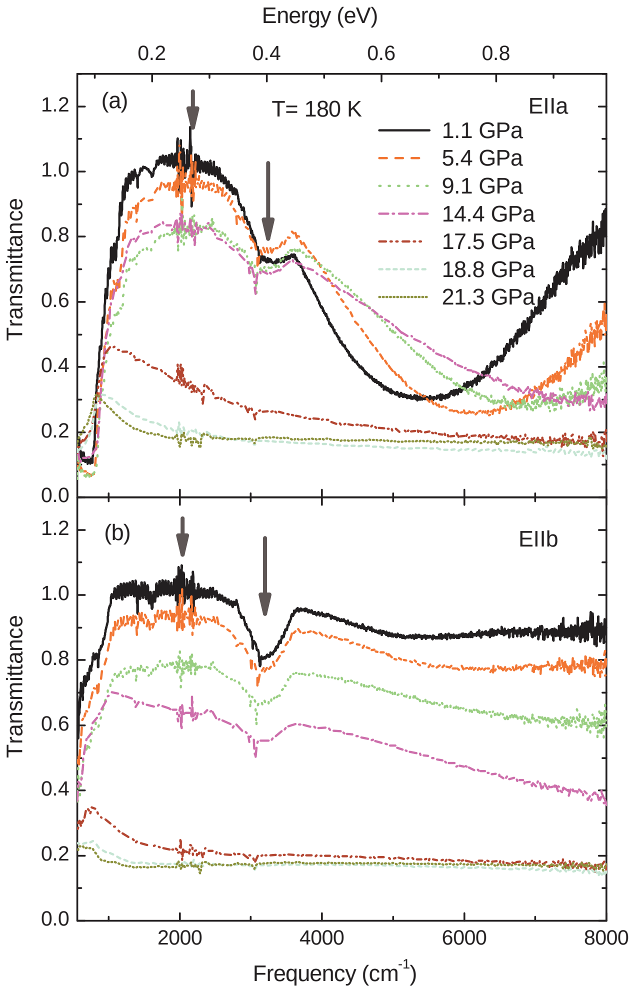

Figure 3: Transmittance spectra of TiOCl for various pressures for the polarization directions $E\|a$, $E\|b$ at around 180 K. Arrows refer to artifacts due to diamond absorption.

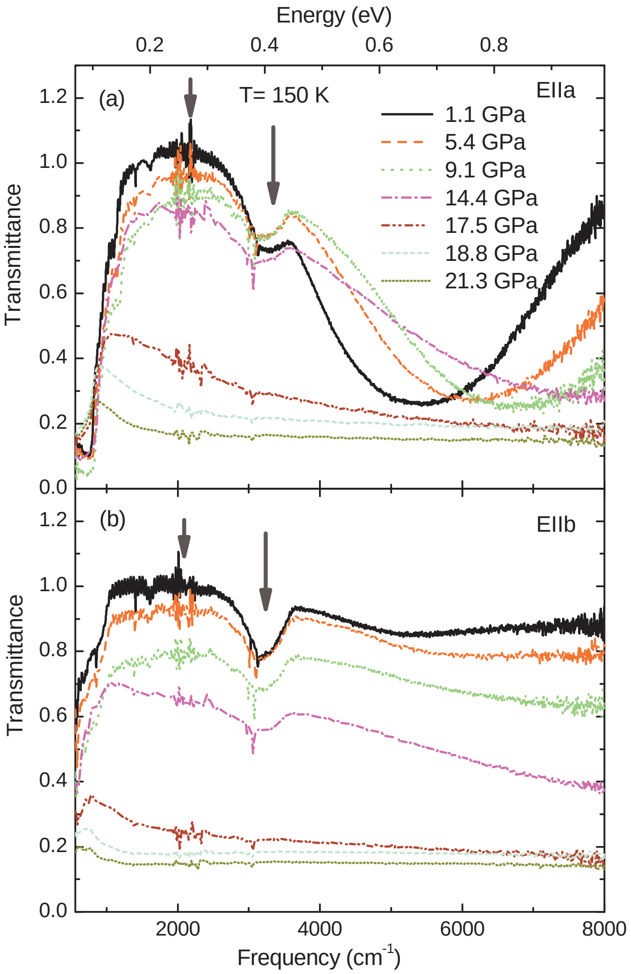

Figure 4: Transmittance spectra of TiOCl for various pressures for the polarization directions $E\|a$, $E\|b$ at around 150 K. Arrows refer to artifacts due to diamond absorption.

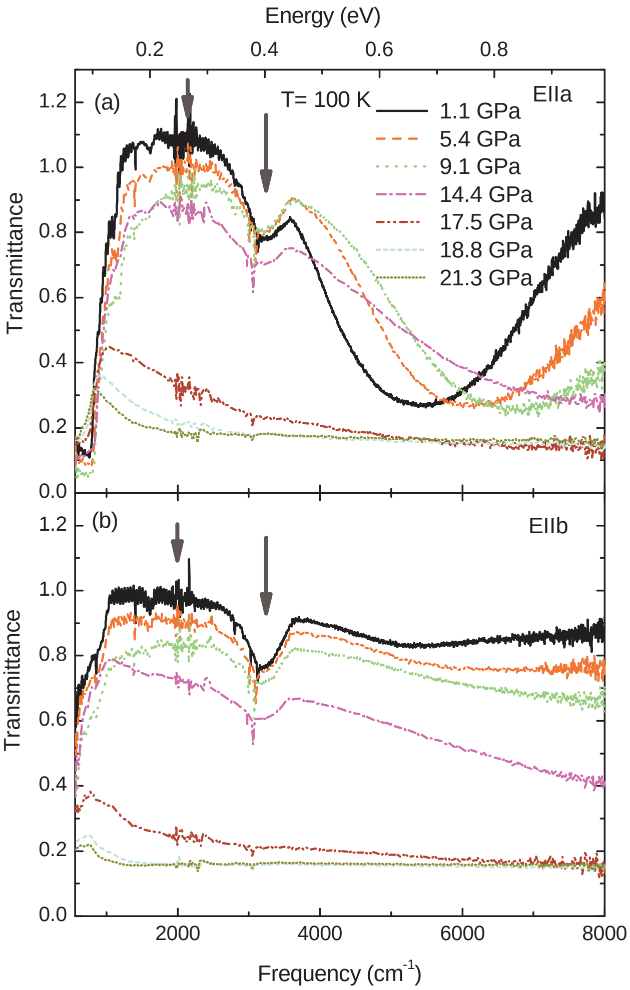

Figure 5: Transmittance spectra of TiOCl for various pressures for the polarization directions $E \| a$, $E \| b$ at around 100 K. Arrows refer to artifacts due to diamond absorption.

References

[1] M. Imada, A. Fujimori, and Y. Tokura, Rev. Mod. Phys. **70**, 1039 (1998).

[2] F. Gebhard, *Mott Metal-Insulator Transition: Models and Methods*, vol. 137 (Springer, 1997).

[3] J. H. de Boer and E. J. W. Verwey, Proceedings of the Physical Society **49**, 59 (1937).

[4] N. F. Mott and R. Peierls, Proceedings of the Physical Society **49**, 72 (1937).

[5] N. F. Mott, Proceedings of the Physical Society. Section A **62**, 416 (1949).

[6] N. F. Mott, Philosophical Magazine **6**, 287 (1961).

[7] F. H. L. Essler, H. Frahm, A. Klmper, and V. E. Korepin, *The One-Dimensional Hubbard Model* (Cambridge University Press, New York, 2005).

[8] J. Schlipf, M. Jarrell, P. G. J. van Dongen, N. Blümer, S. Kehrein, T. Pruschke, and D. Vollhardt, Phys. Rev. Lett. **82**, 4890 (1999).

[9] K. Yamada, *Electron Correlation in Metals* (Cambridge University Press, New York, 2004).

[10] A. Georges, G. Kotliar, W. Krauth, and M. J. Rozenberg, Rev. Mod. Phys. **68**, 13 (1996).

[11] J. Hubbard, Proc. Roy. Soc.(London) **A 281**, 401 (1964).

[12] W. F. Brinkman and T. M. Rice, Phys. Rev. B **2**, 4302 (1970).

[13] M. J. Rozenberg, G. Kotliar, H. Kajueter, G. A. Thomas, D. H. Rapkine, J. M. Honig, and P. Metcalf, Phys. Rev. Lett. **75**, 105 (1995).

[14] J. Merino and R. H. McKenzie, Phys. Rev. B **61**, 7996 (2000).

[15] J. Merino, M. Dumm, N. Drichko, M. Dressel, and R. H. McKenzie, Phys. Rev. Lett. **100**, 086404 (2008).

[16] R. Bulla, T. A. Costi, and D. Vollhardt, Phys. Rev. B **64**, 045103 (2001).

[17] D. Faltermeier, J. Barz, M. Dumm, M. Dressel, N. Drichko, B. Petrov, V. Semkin, R. Vlasova, C. c. Mezi, and P. Batail, Phys. Rev. B **76**, 165113 (2007).

[18] D. B. McWhan and J. P. Remeika, Phys. Rev. B **2**, 3734 (1970).

[19] D. B. McWhan, A. Menth, J. P. Remeika, W. F. Brinkman, and T. M. Rice, Phys. Rev. B **7**, 1920 (1973).

[20] M. Dressel and G. Grüner, *Optical Properties of Solids* (Cambridge University Press, New York, 2002).

[21] X. B. Zhang, T. Taliercio, S. Kolliakos, and P. Lefebvre, Journal of Physics: Condensed Matter **13**, 7053 (2001).

[22] J. P. Falck, A. Levy, M. A. Kastner, and R. J. Birgeneau, Phys. Rev. Lett. **69**, 1109 (1992).

[23] P. Calvani, M. Capizzi, S. Lupi, P. Maselli, A. Paolone, and P. Roy, Phys. Rev. B **53**, 2756 (1996).

[24] D. Schrupp, M. Sing, M. Tsunekawa, H. Fujiwara, S. Kasai, A. Sekiyama, S. Suga, T. Muro, V. A. M. Brabers, and R. Claessen, Europhys. Lett. **70**, 789 (2005).

[25] L. Landau, Phys. Z. Sowjetunion **3**, 644 (1933).

[26] D. Emin, Phys. Rev. B **48**, 13691 (1993).

[27] T. Holstein, Ann. Phys. **8**, 325 (1959).

[28] S. Fratini and S. Ciuchi, Phys. Rev. B **74**, 075101 (2006).

[29] I. G. Austin and N. F. Mott, Adv. Phys. **18**, 41 (1969).

[30] H. Fröhlich, Adv. Phys. **3**, 325 (1954).

[31] J. T. Devreese, in Digital Encyclopedia of Appl. Phys, edited by G. L. Tigger (Wiley, online, 2008). Article also available at arXiv:cond-mat/0004497v2 **14**, 383 (1996).

[32] C. Hartinger, F. Mayr, J. Deisenhofer, A. Loidl, and T. Kopp, Phys. Rev. B **69**, 100403 (2004).

[33] N. F. Mott and E. A. Davis, *Electronic Processes in Non-Crystalline Materials* (Clarendon Press, Oxforf, New York, 1971).

[34] S. Ciuchi, F. de Pasquale, S. Fratini, and D. Feinberg, Phys. Rev. B **56**, 4494 (1997).

[35] X.-X. Bi, P. C. Eklund, and J. M. Honig, Phys. Rev. B **48**, 3470 (1993).

[36] X.-X. Bi and P. C. Eklund, Phys. Rev. Lett. **70**, 2625 (1993).

[37] H. G. Reik, Solid State Commun. **1**, 102 (1963).

[38] M. Ziese and C. Srinitiwarawong, Phys. Rev. B **58**, 11519 (1998).

[39] K. Thirunavukkuarasu, F. Lichtenberg, and C. A. Kuntscher, J. Phys.: Condens. Matter **18**, 9173 (2006).

[40] M. Capone, S. Ciuchi, and C. Grimaldi, Europhys. Lett. **42**, 523 (1998).

[41] V. Ta Phuoc, C. Sellier, B. Corraze, E. Janod, and C. Marin, Eur. Phys. J. B **69**, 181 (2009).

[42] C. A. Kuntscher, D. van der Marel, M. Dressel, F. Lichtenberg, and J. Mannhart, Phys. Rev. B **67**, 035105 (2003).

[43] R. G. Bell, *Introductory Fourier Transform Spectroscopy* (Academic Press, New York, 1972).

[44] P. Griffiths and J. De Haseth, *Fourier Transform Infrared Spectrometry* (John Wiley and sons, 1986).

[45] A. Michelson and E. W. Morley, Am. J. Sci. **22**, 120 (1981).

[46] P. Hariharan, *Basics of Interferometry, Second Edition* (Elsevier, 2007).

[47] B. Stuart, *Infrared Spectroscopy: Fundamentals and Applications* (John Wiley and Sons, 2004).

[48] IFS 66v/S User Manual.

[49] HYPERION User Manual.

[50] M. E. Thomas, *Multiphonon Absorption in Diamond* (1994).

[51] A. Jayaraman, Rev. Mod. Phys. **55**, 65 (1983).

[52] C. Narayanan, H. Luo, J. Orloff, and A. L. Ruoff, Nature **393**, 46 (1998).

[53] `http://www.easylab.co.uk`.

[54] G. Huber, K. Syassen, and W. B. Holzapfel, Phys. Rev. B **15**, 5123 (1977).

[55] G. J. Piermarini and S. Block, Rev. Sci. Instrum. **46**, 973 (1975).

[56] R. A. Forman, G. J. Piermarini, J. D. Barnett, and S. Block, Science **176**, 284 (1972).

[57] J. D. Barnett, S. Block, and G. J. Piermarini, Rev. Sci. Instrum. **44**, 1 (1973).

[58] H. K. Mao, J. Xu, and P. M. Bell, J. Geophys. Res.,[Solid Earth] **91**, 4673 (1986).

[59] K. Thirunavukkuarasu, Phd. thesis, Augsburg University (2009).

[60] `http://www.cryovac.de`.

[61] D. R. Lide, *Physical constants of organic compounds in CRC Handbook of Chemistry and Physics* (CRC Press, Boca Raton, FL, 2005).

[62] M. Fox, *Optical Properties of Solids* (Oxford University Press, London, 2001).

[63] F. Wooten, *Optical properties of solids* (Academic Press, New York, 1972).

[64] F. Bommeli, Phd. thesis, ETH Zrich, Zrich, Switzerland (1997).

[65] K. Wille, *The Physics of Particle Accelerators an introduction* (Oxford University Press, 2000).

[66] `http://ankaweb.fzk.de`.

[67] Syassen, K. private communication.

[68] M. M. Woolfson, *An introduction to X-ray crystallography; Second Edition* (Cambridge University Press, United Kingdom, 1997).

[69] H. P. Klug and L. E. Alexander, *X-ray diffraction procedure; Second Edition* (John wiley and Sons, Inc, New York, 1954).

[70] C. A. Kuntscher, A. Pashkin, H. Hoffmann, S. Frank, M. Klemm, S. Horn, A. Schönleber, S. van Smaalen, M. Hanfland, S. Glawion, et al., Phys. Rev. B **78**, 035106 (2008).

[71] A. P. Hammersley, *FIT2D: An Introduction and Overview*, ESRF, BP 220, 38043 Grenoble, France (1997).

[72] V. Petricek, M. Dusek, and L. Palatinus, *JANA2006. A Crystallographic Computng System*, Institute of Physics, Praha, Czech Republic (2008).

[73] F. C. Voogt, Phd thesis, University of Groningen, The Netherlands (1998).

[74] R. W. G. Wyckoff, *Crystal Structures*, vol. 2nd ed. (Krieger, Malabar, FL, 1982).

[75] `http://wikis.lib.ncsu.edu/index.php/Spinel`.

[76] E. J. W. Verwey, P. W. Haayman, and F. C. Romeijn, Nature (London) **144**, 327 (1939).

[77] E. J. W. Verwey and P. W. Haayman, Physica **8**, 979 (1941).

[78] W. C. Hamilton, Phys. Rev. **110**, 1050 (1958).

[79] M. Iizumi, T. F. Koetzle, G. Shirane, S. Chikazumi, M. Matsui, and S. Todo, Acta Crystallogr., Sect. B: Struct. Sci. **38**, 2121 (1982).

[80] J. P. Wright, J. P. Attfield, and P. G. Radaelli, Phys. Rev. Lett. **87**, 266401 (2001).

[81] J. P. Wright, J. P. Attfield, and P. G. Radaelli, Phys. Rev. B **66**, 214422 (2002).

[82] M. S. Senn, J. P. Wright, and J. P. Attfield, Nature **481**, 173 (2012).

[83] H.-K. Mao, T. Takahashi, W. A. Bassett, G. L. Kinsland, and L. Merrill, J. Geophys. Res. **79**, 1165 (1974).

[84] P. Weiss and R. Forrer, Ann. Phys. **12**, 279 (1929).

[85] T. Okamura, Sci. Rep. Tohoku Imp. Univ.IV **21**, 231 (1932).

[86] E. J. W. Verwey, P. W. Haayman, and F. C. Romeijn, J. Chem. Phys. **15**, 181 (1947).

[87] G. Subias, J. Garcia, J. Blasco, M. Grazia Proietti, H. Renevier, and M. Concepcion Sanchez, Phys. Rev. Lett. **93**, 156408 (2004).

[88] L. Degiorgi, I. Blatter-Mörke, and P. Wachter, Phys. Rev. B **35**, 5421 (1987).

[89] L. V. Gasparov, D. B. Tanner, D. B. Romero, H. Berger, G. Margaritondo, and L. Forró, Phys. Rev. B **62**, 7939 (2000).

[90] R. D. Waldron, Phys. Rev. **99**, 1727 (1955).

[91] S. K. Park, T. Ishikawa, and Y. Tokura, Phys. Rev. B **58**, 3717 (1998).

[92] D. L. Camphausen, J. M. D. Coey, and B. K. Chakraverty, Phys. Rev. Lett. **29**, 657 (1972).

[93] G. K. Rozenberg, G. R. Hearne, M. P. Pasternak, P. A. Metcalf, and J. M. Honig, Phys. Rev. B **53**, 6482 (1996).

[94] H. Kobayashi, I. Isogai, T. Kamimura, N. Hamada, H. Onodera, S. Todo, and N. Môri, Phys. Rev. B **73**, 104110 (2006).

[95] S. V. Ovsyannikov, V. V. Shchennikov, S. Todo, and Y. Uwatoko, J. Phys.: Condens. Matter **20**, 172201 (2008).

[96] M. Pasternak, W. Xu, G. Rozenberg, R. Taylor, and R. Jeanloz, J. Magn. Magn. Mater. **265**, L107 (2003).

[97] S. K. Ramasesha, M. Mohan, A. K. Singh, J. M. Honig, and C. N. R. Rao, Phys. Rev. B **50**, 13789 (1994).

[98] G. A. Samara, Phys. Rev. Lett. **21**, 795 (1968).

[99] L. V. Gasparov, D. Arenas, K.-Y. Choi, G. Guntherodt, H. Berger, L. Forro, G. Margaritondo, V. V. Struzhkin, and R. Hemley, J. Appl. Phys. **97**, 10A922 (2005).

[100] Y. Kakudate, N. Mori, and Y. Kino, J. Magn. Magn. Mater. **12**, 22 (1979).

[101] S. Tamura, J. Phys. Soc. Jpn. **59**, 4462 (1990).

[102] S. Todo, N. Takeshita, T. Kanehara, T. Mori, and N. Mori, J. Appl. Phys. **89**, 7347 (2001).

[103] N. Môri, S. Todo, N. Takeshita, T. Mori, and Y. Akishige, Physica B: Condens. Matter **312**, 686 (2002).

[104] G. K. Rozenberg, M. P. Pasternak, W. M. Xu, Y. Amiel, M. Hanfland, M. Amboage, R. D. Taylor, and R. Jeanloz, Phys. Rev. Lett. **96**, 045705 (2006).

[105] J. Spalek, A. Kozlowski, Z. Tarnawski, Z. Kakol, Y. Fukami, F. Ono, R. Zach, L. J. Spalek, and J. M. Honig, Phys. Rev. B **78**, 100401 (2008).

[106] A. Schlegel, S. F. Alvarado, and P. Wachter, J. Phys. C: Solid State Phys. **12**, 1157 (1979).

[107] V. Brabers, Journal of Crystal Growth **8**, 26 (1971).

[108] J. Ebad-Allah, L. Baldassarre, M. Sing, R. Claessen, V. A. M. Brabers, and C. A. Kuntscher, J. Phys.: Condens. Matter **25**, 035602 (2013).

[109] `http://hyperphysics.phy-astr.gsu.edu/hbase/quantum/hosc.html`.

[110] C. A. Kuntscher, S. Frank, I. Loa, K. Syassen, T. Yamauchi, and Y. Ueda, Phys. Rev. B **71**, 220502 (2005).

[111] S. Frank, C. A. Kuntscher, I. Gregora, J. Petzelt, T. Yamauchi, and Y. Ueda, Phys. Rev. B **76**, 075128 (2007).

[112] E. Nazarenko, J. E. Lorenzo, Y. Joly, J. L. Hodeau, D. Mannix, and C. Marin, Phys. Rev. Lett. **97**, 056403 (2006).

[113] R. Hill, J. Craig, and G. Gibbs, Phys. Chem. Miner. **4**, 317 (1979).

[114] P. Piekarz, K. Parlinski, and A. M. Oles, Phys. Rev. B **76**, 165124 (2007).

[115] M. Kimura, H. Fujiwara, A. Sekiyama, J. Yamaguchi, K. Kishimoto, H. Sugiyama, G. Funabashi, S. Imada, S. Iguchi, Y. Tokura, et al., J. Phys. Soc. Jpn. **79**, 064710 (2010).

[116] J. Ebad-Allah, L. Baldassarre, M. Sing, R. Claessen, V. A. M. Brabers, and C. A. Kuntscher, J. Appl. Phys. **112**, 073524 (2012).

[117] A. Pimenov, S. Tachos, T. Rudolf, A. Loidl, D. Schrupp, M. Sing, R. Claessen, and V. A. M. Brabers, Phys. Rev. B **72**, 035131 (2005).

[118] H. Schäfer, F. Wartenpfuhl, and E. Weise, Z. Anorg. Allg. Chem. **295**, 268 (1958), ISSN 1521-3749.

[119] T. Sasaki, M. Mizumaki, K. Kato, Y. Watabe, Y. Nishihata, M. Takata, and J. Akimitsu, J. Phys. Soc. Jpn. **74**, 2185 (2005).

[120] S. Blanco-Canosa, F. Rivadulla, A. Pineiro, V. Pardo, D. Baldomir, D. I. Khomskii, M. M. Abd-Elmeguid, M. A. Lopez-Quintela, and J. Rivas, Phys. Rev. Lett. **102**, 056406 (2009).

[121] A. Seidel, C. A. Marianetti, F. C. Chou, G. Ceder, and P. A. Lee, Phys. Rev. B **67**, 020405 (2003).

[122] E. T. Abel, K. Matan, F. C. Chou, E. D. Isaacs, D. E. Moncton, H. Sinn, A. Alatas, and Y. S. Lee, Phys. Rev. B **76**, 214304 (2007).

[123] S. Glawion, J. Heidler, M. W. Haverkort, L. C. Duda, T. Schmitt, V. N. Strocov, C. Monney, K. J. Zhou, A. Ruff, M. Sing, et al., Phys. Rev. Lett. **107**, 107402 (2011).

[124] S. Glawion, M. R. Scholz, Y.-Z. Zhang, R. Valenti, T. Saha-Dasgupta, M. Klemm, J. Hemberger, S. Horn, M. Sing, and R. Claessen, Phys. Rev. B **80**, 155119 (2009).

[125] S. Glawion, Phd. thesis, Würzburg University (2010).

[126] V. I. Anisimov, F. Aryasetiawan, and A. I. Lichtenstein, J. Phys.: Condens. Matter **9**, 767 (1997).

[127] T. Saha-Dasgupta, A. Lichtenstein, M. Hoinkis, S. Glawion, M. Sing, R. Claessen, and R. Valent, New J. Phys. **9**, 380 (2007).

[128] R. Rückamp, J. Baier, M. Kriener, M. W. Haverkort, T. Lorenz, G. S. Uhrig, L. Jongen, A. Möller, G. Meyer, and M. Grüninger, Phys. Rev. Lett. **95**, 097203 (2005).

[129] R. Rückamp, E. Benckiser, M. W. Haverkort, H. Roth, T. Lorenz, A. Freimuth, L. Jongen, A. Möller, G. Meyer, P. Reutler, et al., New Journal of Physics **7**, 144 (2005).

[130] C. Kuntscher, M. Klemm, S. Horn, M. Sing, and R. Claessen, Eur. Phys. J. Special Topics **180**, 29 (2009).

[131] P. Anderson, Mater. Res. Bull. **8**, 153 (1973).

[132] R. J. Beynon and J. A. Wilson, J. Phys.: Condens. Matter **5**, 1983 (1993).

[133] V. Kataev, J. Baier, A. Möller, L. Jongen, G. Meyer, and A. Freimuth, Phys. Rev. B **68**, 140405 (2003).

[134] S. Saha, S. Golin, T. Imai, and F. Chou, J. Phys. Chem. Solids **68**, 2044 (2007).

[135] M. Shaz, S. van Smaalen, L. Palatinus, M. Hoinkis, M. Klemm, S. Horn, and R. Claessen, Phys. Rev. B **71**, 100405 (2005).

[136] J. Hemberger, M. Hoinkis, M. Klemm, M. Sing, R. Claessen, S. Horn, and A. Loidl, Phys. Rev. B **72**, 012420 (2005).

[137] A. Krimmel, J. Strempfer, B. Bohnenbuck, B. Keimer, M. Hoinkis, M. Klemm, S. Horn, A. Loidl, M. Sing, R. Claessen, et al., Phys. Rev. B **73**, 172413 (2006).

[138] G. Caimi, L. Degiorgi, P. Lemmens, and F. C. Chou, J. Phys.: Condens. Matter **16**, 5583 (2004).

[139] S. van Smaalen, L. Palatinus, and A. Schönleber, Phys. Rev. B **72**, 020105 (2005).

[140] C. A. Kuntscher, S. Frank, A. Pashkin, M. Hoiniks, M. Klemm, M. Sing, S. Horn, and R. Claessen, Phys. Rev. B **74**, 184402 (2006).

[141] C. A. Kuntscher, S. Frank, A. Pashkin, H. Hoffmann, A. Schönleber, S. van Smaalen, M. Hanfland, S. Glawion, M. Klemm, M. Sing, et al., Phys. Rev. B **76**, 241101 (2007).

[142] M. K. Forthaus, T. Taetz, A. Möller, and M. M. Abd-Elmeguid, Phys. Rev. B **77**, 165121 (2008).

[143] Y.-Z. Zhang, H. O. Jeschke, and R. Valenti, Phys. Rev. Lett. **101**, 136406 (2008).

[144] J. Ebad-Allah, A. Schönleber, S. van Smaalen, M. Hanfland, M. Klemm, S. Horn, S. Glawion, M. Sing, R. Claessen, and C. A. Kuntscher, Phys. Rev. B **82**, 134117 (2010).

[145] A. Prodi, J. S. Helton, Y. Feng, and Y. S. Lee, Phys. Rev. B **81**, 201103 (2010).

[146] C. Kato, Y. Kobayashi, and M. Sato, J. Phys. Soc. Jpn. **74**, 473 (2005).

[147] P. V. Rysselberghe, J. Phys. Chem. **36**, 1152 (1931).

[148] A. Schönleber, S. van Smaalen, and L. Palatinus, Phys. Rev. B **73**, 214410 (2006).

[149] A. Schönleber, G. Shcheka, and S. van Smaalen, Phys. Rev. B **77**, 094117 (2008).

Acknowledgements

Many people have helped me to finish this dissertation, and I owe my gratitude to all of them. First of all, my deepest acknowledgements go to my supervisor, Prof. Dr. Christine Kuntscher, whose scientific enthusiasm has been a precious constant during my work. In particular I want to thank her for giving me the opportunity to work in her group and for providing me as much help as I needed. My thankfulness for her not only because her help with physical questions, but also for her encouragements that always lifted good feeling inside me especially after my accident. Without her knowledge and support I would not complete this study.

My great thanks to our collaborators Prof. Dr. Sander van Smaalen and Dr. Andreas Schönleber (Bayreuth University) for their guidance and advice for analyzing the x-ray diffraction data of TiOCl, also to Prof. Dr. R. Claessen and Prof. Dr. V. A. M. Brabers for providing us with the TiOCl and magnetite samples which were studied within this dissertation. I am grateful to Dr. Leoneta Baldassarre for providing me with her experience and to Dr. Günter Obermeier for his assistance to carry out the DC measurements of magnetite.

My thankfulness to all of the current and former group members of Prof. Dr. Christine Kuntscher for their support. It is a pleasure also to acknowledge Mrs. Beate Spörhase for her technical support and Mrs. Jutta Hampel for her assistance with the official stuff.

Finally, I would like to use this opportunity to thank the Egyptian government and all the members of the Physics department at Tanta University for giving me this chance to study my Ph.D. in Germany.

Curriculum Vitae

Personal information

Date of birth	21 May 1974
Nationality	Egyptian
Gender	Female
Martial status	Married

Education

Sep 1980 - May 1992	All Egyptian Primary and Secondary Schools.
Sep 1992 - Jun 1996	Bachelor's degree in Physics, Faculty of Science, Physics Department, Tanta University, Tanta, Egypt.
Sept 1996 - Sept 1997	Pre-Master on Theoretical Physics, Faculty of Science, Physics Department, Tanta University, Tanta, Egypt.
Jan 2004	Master's degree in Physics, Faculty of Science, Physics Department, Tanta University, Tanta, Egypt; Title: *Analysis of Atomic Collision Processes.*
Sept 2004	Enrolled in a Ph.D. Program in theoretical atomic physics at Tanta University, Faculty of Science, Physics Department, Tanta,, Egypt.
April 2006 - Aug 2006	Studies of a German language course at Goethe institute, Cairo , Egypt.
April 2007	The Ph.D. programme at Tanta University was cancelled
Since May 2008	Start of Ph.D. in Physics, Experimental physics II, Augsburg University, Augsburg, Germany, Supervisor: Prof. Dr. Christine Kuntscher.
Jun 2012 - Jun 2013	The Ph.D. study in Physics, Experimental physics II, Augsburg University, Germany, interrupted because of illness vacation.

Work Experience

Jan 1997- Jan 2004	Instructor, Faculty of Science, Physics Department, Tanta University, Tanta, Egypt.
Since March 2004	Assistant Lecturer, Faculty of Science, Physics Department, Tanta University, Tanta, Egypt.

List of publications

- *Infrared studies of magnetite under high pressure.*
  J. Ebad-Allah, L. Baldassarre, M. Sing, R. Claessen, V.A.M. Brabers, and C.A. Kuntscher,
  High Pressure Research **29**, 500 (2009).
- *Filling of the Mott-Hubbard gap in the oxyhalides TiOCl and TiOBr induced by external pressure.*
  C. A. Kuntscher, J. Ebad-Allah, A. Pashkin, S. Frank, M. Klemm, S. Horn, A. Schoenleber, S. van Smaalen, M. Hanfland, S. Glawion, M. Sing, and R. Claessen ,
  High Pressure Research **29**, 509 (2009).
- *Two pressure-induced structural phase transitions in TiOCl.*
  J. Ebad-Allah, A. Schoenleber, S. van Smaalen, M. Hanfland, M. Klemm, S. Horn, S. Glawion, M. Sing, R. Claessen, and C.A. Kuntscher,
  Phys. Rev. B **82**, 134117 (2010).
- *Pressure dependence of the Verwey transition in magnetite: an infrared spectroscopic point of view.*
  J. Ebad-Allah, L. Baldassarre, R. Claessen, M. Sing, V.A.M. Brabers, and C.A. Kuntscher,
  J. Appl. Phys. **112**, 073524 (2012).
- *Polaron physics and crossover transition in magnetite probed by pressure-dependent infrared spectroscopy.*
  J. Ebad-Allah, L. Baldassarre, M. Sing, R. Claessen, V.A.M. Brabers, and C.A. Kuntscher,
  J. Phys.: Condens. Matter **25**, 035602 (2013).

- *Polaron physics and crossover transition in magnetite probed by pressure-dependent infrared spectroscopy.*
  A. M. Anton, W. Kossack, C. Gutsche, R. Figuli, P. Papadopoulos, J. Ebad-Allah, C. A. Kuntscher and F. Kremer,
  Macromolecules **46**, 4919-4923 (2013)..